

Euclid preparation. Expected constraints on initial conditions

Euclid Collaboration: F. Finelli^{★1,2}, Y. Akrami^{3,4}, A. Andrews^{1,2}, M. Ballardini^{5,6,1}, S. Casas⁷, D. Karagiannis^{5,8}, Z. Sakr^{9,10,11}, J. Valiviita^{12,13}, G. Alestas³, N. Bartolo^{14,15,16}, J. R. Bermejo-Cli ment^{17,18}, S. Nesseris³, D. Paoletti^{1,2}, D. Sapone¹⁹, I. Tutusaus¹⁰, A. Achúcarro^{20,21}, G. Cañas-Herrera^{22,20,23}, J. Jasche^{24,25}, G. Lavaux²⁶, N. Aghanim²⁷, B. Altieri²⁸, A. Amara²⁹, L. Amendola⁹, S. Andreon³⁰, N. Auricchio¹, C. Baccigalupi^{31,32,33,34}, D. Bagot³⁵, M. Baldi^{36,1,37}, S. Bardelli¹, P. Battaglia¹, A. Biviano^{32,31}, E. Branchini^{38,39,30}, M. Brescia^{40,41}, S. Camera^{42,43,44}, V. Capobianco⁴⁴, C. Carbone⁴⁵, J. Carretero^{46,47}, M. Castellano⁴⁸, G. Castignani¹, S. Cavuoti^{41,49}, K. C. Chambers⁵⁰, A. Cimatti⁵¹, C. Colodro-Conde¹⁷, G. Congedo⁵², C. J. Conselice⁵³, L. Conversi^{54,28}, Y. Copin⁵⁵, F. Courbin^{56,57}, H. M. Courtois⁵⁸, M. Cropper⁵⁹, A. Da Silva^{60,61}, H. Degaudenzi⁶², S. de la Torre⁶³, G. De Lucia³², A. M. Di Giorgio⁶⁴, H. Dole²⁷, M. Douspis²⁷, F. Dubath⁶², C. A. J. Duncan^{52,53}, X. Dupac²⁸, S. Dusini¹⁵, S. Escoffier⁶⁵, M. Farina⁶⁴, R. Farinelli¹, F. Faustini^{48,66}, S. Ferriol⁵⁵, P. Fosalba^{67,68}, M. Frailis³², E. Franceschi¹, M. Fumana⁴⁵, S. Galeotta³², K. George⁶⁹, B. Gillis⁵², C. Giocoli^{1,37}, J. Gracia-Carpio⁷⁰, A. Grazian¹⁶, F. Grupp^{70,69}, S. V. H. Haugan⁷¹, W. Holmes⁷², I. M. Hook⁷³, F. Hormuth⁷⁴, A. Hornstrup^{75,76}, K. Jahnke⁷⁷, M. Jhabvala⁷⁸, B. Joachimi⁷⁹, E. Keihänen⁸⁰, S. Kermiche⁶⁵, A. Kiessling⁷², B. Kubik⁵⁵, M. Kümmel⁶⁹, M. Kunz⁸¹, H. Kurki-Suonio^{12,13}, A. M. C. Le Brun⁸², S. Ligi⁴⁴, P. B. Lilje⁷¹, V. Lindholm^{12,13}, I. Lloro⁸³, G. Mainetti⁸⁴, D. Maino^{85,45,86}, E. Maiorano¹, O. Mansutti³², S. Marcin⁸⁷, O. Marggraf⁸⁸, M. Martinelli^{48,89}, N. Martinet⁶³, F. Marulli^{90,1,37}, R. J. Massey⁹¹, E. Medinaceli¹, S. Mei^{92,93}, Y. Mellier^{24,26}, M. Meneghetti^{1,37}, E. Merlin⁴⁸, G. Meylan⁹⁴, A. Mora⁹⁵, M. Moresco^{90,1}, L. Moscardini^{90,1,37}, C. Neissner^{96,47}, S.-M. Niemi²², C. Padilla⁹⁶, S. Paltani⁶², F. Pasian³², K. Pedersen⁹⁷, W. J. Percival^{98,99,100}, V. Pettorino²², S. Pires¹⁰¹, G. Polenta⁶⁶, M. Poncet³⁵, L. A. Popa¹⁰², L. Pozzetti¹, F. Raison⁷⁰, R. Rebolo^{17,103,18}, A. Renzi^{14,15}, J. Rhodes⁷², G. Riccio⁴¹, E. Romelli³², M. Roncarelli¹, C. Rosset⁹², R. Saglia^{69,70}, B. Sartoris^{69,32}, M. Schirmer⁷⁷, T. Schrabback¹⁰⁴, A. Secroun⁶⁵, E. Sefusatti^{32,31,33}, G. Seidel⁷⁷, M. Seiffert⁷², S. Serrano^{67,105,68}, P. Simon⁸⁸, C. Sirignano^{14,15}, G. Sirri³⁷, A. Spurio Mancini¹⁰⁶, L. Stanco¹⁵, J. Steinwagner⁷⁰, P. Tallada-Crespi^{46,47}, D. Tavagnacco³², A. N. Taylor⁵², I. Tereno^{60,107}, N. Tessore⁷⁹, S. Toft^{108,109}, R. Toledo-Moreo¹¹⁰, F. Torradeflot^{47,46}, L. Valenziano^{1,2}, T. Vassallo^{69,32}, G. Verdoes Kleijn¹¹¹, A. Veropalumbo^{30,39,38}, Y. Wang¹¹², J. Weller^{69,70}, A. Zacchei^{32,31}, G. Zamorani¹, F. M. Zerbi³⁰, E. Zucca¹, V. Allevato⁴¹, E. Bozzo⁶², C. Burigana^{113,2}, R. Cabanac¹⁰, M. Calabrese^{114,45}, A. Cappi^{1,115}, D. Di Ferdinando³⁷, J. A. Escartin Vigo⁷⁰, L. Gabarra¹¹⁶, J. Martín-Fleitas¹¹⁷, S. Matthew⁵², N. Mauri^{51,37}, R. B. Metcalf^{90,1}, A. A. Nucita^{118,119,120}, A. Pezzotta^{121,70}, M. Pöntinen¹², C. Porciani⁸⁸, I. Risso¹²², V. Scottez^{24,123}, M. Sereno^{1,37}, M. Tenti³⁷, M. Viel^{31,32,34,33,124}, M. Wiesmann⁷¹, I. T. Andika^{125,126}, M. Archidiacono^{85,86}, F. Atrio-Barandela¹²⁷, S. Avila⁴⁶, A. Balaguera-Antolinez^{17,128}, D. Bertacca^{14,16,15}, M. Bethermin¹²⁹, A. Blanchard¹⁰, L. Blot^{130,82}, H. Böhringer^{70,131,132}, S. Borgani^{133,31,32,33,124}, M. L. Brown⁵³, S. Bruton¹³⁴, A. Calabro⁴⁸, B. Camacho Quevedo^{31,34,32,67,68}, F. Caro⁴⁸, C. S. Carvalho¹⁰⁷, T. Castro^{32,33,31,124}, F. Cogato^{90,1}, S. Conseil⁵⁵, A. R. Cooray¹³⁵, S. Davini³⁹, F. De Paolis^{118,119,120}, G. Desprez¹¹¹, A. Díaz-Sánchez¹³⁶, J. J. Diaz¹⁷, S. Di Domizio^{38,39}, J. M. Diego¹³⁷, P. Dimauro^{138,48}, A. Enia^{36,1}, Y. Fang⁶⁹, A. G. Ferrari³⁷, A. Finoguenov¹², A. Fontana⁴⁸, A. Franco^{119,118,120}, K. Ganga⁹², J. García-Bellido³, T. Gasparetto³², V. Gautard¹³⁹, E. Gaztanaga^{68,67,140}, F. Giacomini³⁷, F. Gianotti¹, G. Gozaliasl^{141,12}, A. Gruppuso^{1,37}, M. Guidi^{36,1}, C. M. Gutierrez¹⁴², S. Hemmati¹⁴³, C. Hernández-Monteagudo^{18,17}, H. Hildebrandt¹⁴⁴, J. Hjorth⁹⁷, S. Joudaki⁴⁶, J. J. E. Kajava^{145,146}, Y. Kang⁶², V. Kansal^{147,148}, K. Kiiveri⁸⁰, C. C. Kirkpatrick⁸⁰, S. Kruk²⁸, M. Lattanzi⁶, V. Le Brun⁶³, J. Le Graet⁶⁵, L. Legrand^{149,150}, M. Lembo²⁶, F. Lepori¹⁵¹, G. Leroy^{152,91}, G. F. Lesci^{90,1}, J. Lesgourgues⁷, L. Leuzzi¹, T. I. Liaudat¹⁵³, J. Macias-Perez¹⁵⁴, G. Maggio³², M. Magliocchetti⁶⁴, F. Mannucci¹⁵⁵, R. Maoli^{156,48}, C. J. A. P. Martins^{157,158}, L. Maurin²⁷, M. Migliaccio^{159,160}, M. Miluzio^{28,161}, P. Monaco^{133,32,33,31}, C. Moretti^{34,124,32,31,33}, G. Morgante¹, S. Nadathur¹⁴⁰, K. Naidoo¹⁴⁰, A. Navarro-Alsina⁸⁸, L. Pagano^{5,6}, F. Passalacqua^{14,15}, K. Paterson⁷⁷, L. Patrizii³⁷, A. Pisani⁶⁵, D. Potter¹⁵¹, S. Quai^{90,1}, M. Radovich¹⁶, P. Reimberg²⁴, P.-F. Rocci²⁷, G. Rodighiero^{14,16}, S. Sacquogna^{118,119,120}, M. Sahlén¹⁶², D. B. Sanders⁵⁰, E. Sarpa^{34,124,33}, A. Schneider¹⁵¹, D. Sciotti^{48,89}, E. Sellentin^{163,23}, L. C. Smith¹⁶⁴, K. Tanidis¹¹⁶, C. Tao⁶⁵, G. Testera³⁹, R. Teyssier¹⁶⁵, S. Tosi^{38,39,30}, A. Troja^{14,15}, M. Tucci⁶², C. Valieri³⁷, A. Venhola¹⁶⁶, D. Vergani¹, F. Vernizzi¹⁶⁷, G. Verza¹⁶⁸, P. Vielzeuf⁶⁵, and N. A. Walton¹⁶⁴

(Affiliations can be found after the references)

Received Month Day 2025; accepted Month Day, 2025

ABSTRACT

Context. The *Euclid* mission of the European Space Agency will deliver galaxy and cosmic shear surveys, which will be used to constrain initial conditions and statistics of primordial fluctuations.

Aims. We present highlights for the *Euclid* scientific capability to test initial conditions beyond Λ CDM with the 3-dimensional galaxy clustering from the spectroscopic survey, the tomographic approach to 3×2 pt statistics (information) from photometric galaxy survey, and their combination. We then present how these *Euclid* results can be enhanced when combined with current and future measurements of the cosmic microwave background (CMB) anisotropies.

Methods. We provide Fisher forecasts from the combination of *Euclid* spectroscopic and photometric surveys for spatial curvature, running of the spectral index of the power spectrum of curvature perturbations, isocurvature perturbations, and primordial features. For the parameters of these models we also provide the combination of *Euclid* forecasts (pessimistic and optimistic) with three different CMB specifications, i.e. *Planck*, the Simons Observatory (SO), and CMB-S4. We provide Fisher forecasts for how the power spectrum and bispectrum from the *Euclid* spectroscopic survey will constrain the local, equilateral, and orthogonal shapes of primordial non-Gaussianity. We also review how Bayesian field-level inference of primordial non-Gaussianity can constrain local primordial non-Gaussianity.

Results. We find that the combination of the *Euclid* main probes will provide the uncertainty of $\sigma(\Omega_K) = 0.0044$ (0.003) at the 68% confidence level (CL) in the pessimistic (optimistic) settings assuming flat spatial sections as fiducial cosmology. We also find that the combination of the *Euclid* main probes can detect the running of the scalar spectral index for the fiducial value $\alpha_s = -0.01$ with approximately 2σ (4σ) uncertainty and provide the uncertainty of $\sigma(\alpha_s) = 0.004$ (0.0015) for the fiducial value $\alpha_s = -0.001$ at the 68% CL, always with pessimistic (optimistic) settings. We show how *Euclid* will have the capability to provide constraints on isocurvature perturbations with a blue spectral index that are one order of magnitude tighter than current bounds. The combined power spectrum and bispectrum Fisher forecast for the *Euclid* spectroscopic survey leads to $\sigma(f_{\text{NL}}^{\text{local}}) = 2.2$, $\sigma(f_{\text{NL}}^{\text{equil}}) = 108$, and $\sigma(f_{\text{NL}}^{\text{ortho}}) = 33$ by assuming $k_{\text{max}} = 0.15 h \text{Mpc}^{-1}$ and universality for the halo mass function. We show how the expected uncertainty on the local shape decreases by encompassing summary statistics and using Bayesian field-level inference. For the *Euclid* main probes, we find relative errors on the amplitude of primordial oscillations (with a fiducial value of 0.01), of 21% (18 %) for linear frequency and of 22% (18 %) for logarithmic frequency at 68.3% CL in the pessimistic (optimistic) case. These uncertainties can be further improved by adding the information from the bispectrum and the non-linear reconstruction.

Conclusions. We show how *Euclid*, with its unique combination of 3-dimensional galaxy clustering from the spectroscopic survey and 3×2 pt statistics from the photometric survey, will provide the tightest constraints on low redshift to date. By targeting a markedly different range in redshift and scale, *Euclid*'s expected uncertainties are complementary to those obtained by CMB primary anisotropy, returning the tightest combined constraints on the physics of the early Universe.

Key words. *Euclid* – large-scale structure – initial conditions – early Universe – inflation

1. Introduction

The initial conditions of primordial fluctuations are the most ancient fossil imprint of the early Universe, which can be retrieved from the statistical properties of the cosmological data provided by galaxy surveys. With the large fraction of the sky measured by the current and planned galaxy surveys and their large redshift coverage, not only will they greatly improve our understanding of dark energy and dark matter, but they will also provide the most precise measurement of the initial conditions of primordial fluctuations at low redshift (Amendola et al. 2018; Alvarez et al. 2014).

The current observational status is consistent with a spatially flat universe and nearly Gaussian, adiabatic perturbations whose spectrum is described by a simple power-law function (Planck Collaboration: Aghanim et al. 2020b; Planck Collaboration: Akrami et al. 2020a,b; Alam et al. 2021):

$$\mathcal{P}_{\mathcal{R}}(k) \equiv \frac{k^3}{2\pi^2} |\mathcal{R}(k)|^2 = A_s \left(\frac{k}{k_*} \right)^{n_s - 1}, \quad (1)$$

where A_s is the amplitude of the power spectrum of the scalar curvature perturbation \mathcal{R} at the pivot scale k_* (usually taken to be $k_* = 0.05 \text{Mpc}^{-1}$) and n_s is the scalar spectral index.

Current cosmological observations are consistent with the key predictions of cosmic inflation (Brout et al. 1978; Starobinsky 1980; Guth 1981; Sato 1981; Linde 1982; Albrecht & Steinhardt 1982; Hawking et al. 1982; Linde 1983), a phase of nearly exponential expansion in the primordial Universe, which diluted any pre-existing inhomogeneity – this has provided arguably the most elegant solution to the flatness problem and the other puzzles of the standard hot Big Bang cosmology. In the simplest models, a single real Klein–Gordon scalar field – the inflaton

– slowly rolling on a sufficiently flat potential, drives the inflationary stage, during which unavoidable quantum fluctuations in scalar (Mukhanov & Chibisov 1981; Hawking 1982; Guth & Pi 1982; Starobinsky 1982; Bardeen et al. 1983; Mukhanov 1985) and tensor (Starobinsky 1979) curvature perturbations are stretched to scales relevant for structure formation inheriting a nearly scale-invariant spectrum with statistics that are close to Gaussian. The initial conditions for the primordial perturbations, which evolve into the large-scale structure that we observe today, are therefore connected to the inflaton's Lagrangian, in particular to the inflaton's potential, under minimal assumptions for the simplest models.

The power of cosmological observations to constrain the initial conditions is currently dominated by measurements of the anisotropies of the cosmic microwave background (CMB), which mainly provide a snapshot of initial conditions at photon decoupling, i.e. at $z \sim 1100$, when cosmological fluctuations can be described in the linear regime. However, by the end of the current decade, thanks to the 3-dimensional (3D) information contained in the large-scale structure (LSS), the constraining power on the initial conditions retrieved from statistics of the data provided by the galaxy surveys DESI (DESI Collaboration: Aghamousa et al. 2016; Adame et al. 2025), *Euclid* (Euclid Collaboration: Mellier et al. 2025), LSST/Vera Rubin Observatory (LSST Science Collaboration et al. 2009), and SPHEREx (Doré et al. 2014) will increase significantly compared to current LSS measurements. Thanks to the sensitivity to the initial conditions at different redshifts and wavelengths, and to the access to the higher number of modes contained in the 3D volume, galaxy surveys will help us break the degeneracies between cosmological parameters that are encoded in the CMB constraints. This will lead to combined, tighter constraints on initial conditions that

* e-mail: fabio.finelli@inaf.it

are more robust than current bounds on the physics governing the low-redshift cosmological evolution.

Euclid (Laureijs et al. 2011; Euclid Collaboration: Mellier et al. 2025; Euclid Collaboration: Scaramella et al. 2022) is a medium-class mission of the European Space Agency, launched on July 1st, 2023, which will map the local Universe to improve our understanding of cosmic expansion history and of the growth of cosmic structures. The telescope will observe approximately 14 000 deg² of the sky through two instruments. The Visible Camera (Euclid Collaboration: Cropper et al. 2025) will collect optical images of more than one billion galaxies, whose photometric redshift will be determined with supporting ground-based observations. The Near-Infrared Spectrometer and Photometer (Euclid Collaboration: Jahnke et al. 2025), aims to determine emission-line redshifts of between 20 and 30 million galaxies in the range $0.9 < z < 1.8$ by using slitless spectroscopy. The combination of spectroscopy and photometry will allow us to measure galaxy clustering and weak gravitational lensing, aiming at percent accuracy in the corresponding power spectra.

In this paper we study the *Euclid* capabilities in testing initial conditions and statistics of primordial fluctuations through their main probes, i.e. 3D clustering from the galaxy spectroscopic sample and the tomographic approach to the joint galaxy clustering - weak gravitational lensing statistics from the photometric galaxy survey. We will also show how these *Euclid* forecasts can be enhanced when combined with current and future measurements of the cosmic microwave background (CMB) anisotropies.

This paper is organised as follows. In Sect. 2, we summarise the modeling of *Euclid* clustering from the spectroscopic survey and of the joint galaxy clustering – weak lensing analysis – from the photometric survey. We present in Sect. 3 the expected constraints from *Euclid*'s main probes on the spatial curvature of the Universe, i.e. on the curvature parameter Ω_K . *Euclid* forecasts for the constraints on the spectral index of the spectrum of curvature perturbations and its running are presented in Sect. 4. We discuss in Sect. 5 how *Euclid* can constrain the presence of additional isocurvature fluctuations. In Sect. 6 we discuss the expected constraints on primordial non-Gaussianity. We first present the Fisher forecasts of the joint power spectrum and bispectrum analysis of the *Euclid* spectroscopic survey for the local, equilateral, and orthogonal main shapes. In the same section we also summarise what can be achieved for the local shape of primordial non-Gaussianity by Bayesian field-level inference, always for the spectroscopic survey. Section 7 summarises the expected constraints from *Euclid* on primordial features, and finally, Sect. 8 presents our conclusions. In Appendix A, we review the methodology adopted to combine the *Euclid* forecasts with the information contained in current and future measurements of the CMB anisotropies.

In this paper, unless stated otherwise, all uncertainties (denoted by σ) are provided at the 68% confidence level (CL).

2. *Euclid*'s main probes

In this section, we summarise the modelling of the spectroscopic galaxy clustering, the 3×2 pt analysis from the photometric survey, and their combination, following Euclid Collaboration: Blanchard et al. (2020), henceforth, EC20¹. Although

¹ Differently from EC20, we use only the direct approach to 3D galaxy clustering used in EC20. We also corrected the inconsistency in the unit conversion from Mpc^{-1} to $h \text{Mpc}^{-1}$ in the 3D galaxy clustering that affected forecasts in EC20: thus, the uncertainty in h degrades with re-

the currently foreseen specifications of the *Euclid* Wide Survey (EWS) differ from those assumed in EC20, e.g. in terms of the survey area (Euclid Collaboration: Mellier et al. 2025), and the theoretical non-linear modelling within the *Euclid* collaboration has made progress since EC20 – see, e.g., Euclid Collaboration: Bose et al. (2024); Euclid Collaboration: Koyama et al. (2025) for physics beyond Λ CDM at low redshift – we use the EC20 methodology here for initial conditions to allow for comparison with similar forecasts in the context of dark energy/modified gravity (Euclid Collaboration: Casas et al. 2023; Euclid Collaboration: Frusciante et al. 2024), neutrinos (Euclid Collaboration: Archidiacono et al. 2025), and particle dark matter (Euclid Collaboration: Lesgourgues et al. 2025).

2.1. Spectroscopic galaxy clustering

We model the full, anisotropic, non-linear observed galaxy power spectrum as:

$$P_{\text{obs}}(k_{\text{ref}}, \mu_{\text{ref}}; z) = \frac{1}{q_{\perp}^2(z) q_{\parallel}(z)} \left\{ \frac{[b(z)\sigma_8(z) + f_g(z)\sigma_8(z)\mu^2]^2}{1 + k^2\mu^2 f_g^2(z)\sigma_p^2(z)} \right\} \times \frac{P_{\text{dw}}(k, \mu; z)}{\sigma_8^2(z)} F_z(k, \mu; z) + P_s(z), \quad (2)$$

where μ is the cosine of the angle of the wave mode with respect to the line of sight pointing in the \hat{r} direction, and k is the wavenumber of the perturbation. The subscript ‘‘ref’’ refers to the reference (or fiducial) cosmology.

The first term on the right-hand side of Eq. (2) is due to the Alcock–Paczynski (AP) effect (Alcock & Paczynski 1979), which takes into account deviations from the fiducial cosmology by the conversion of redshifts and angles in perpendicular and parallel distances,

$$q_{\perp}(z) = \frac{k_{\perp, \text{ref}}}{k_{\perp}} = \frac{D_A(z)}{D_{A, \text{ref}}(z)},$$

$$q_{\parallel}(z) = \frac{k_{\parallel, \text{ref}}}{k_{\parallel}} = \frac{H_{\text{ref}}(z)}{H(z)}, \quad (3)$$

where $D_A(z)$ and $H(z)$ are the angular diameter distance and the Hubble expansion rate, respectively.

The anisotropic distortion in the density field due to the line-of-sight effects of the peculiar velocity of the observed galaxy redshifts, known as redshift-space distortions (RSD), is modelled in the linear regime by the contribution in the numerator in the curly brackets of Eq. (2) (Kaiser 1987). Here, the linear galaxy bias b , connecting the dark matter (DM) power spectrum to the one of $\text{H}\alpha$ emitter galaxies targeted by NISP, and the growth rate f_g are considered scale-independent unless otherwise specified. The fingers-of-god (FoG) effect caused by galaxy peculiar velocity is modelled as a Lorentzian factor with the distance dispersion $\sigma_p(z)$ following Hamilton (1998).

The dewiggled power spectrum, $P_{\text{dw}}(k, \mu; z)$, models the smearing of the baryon acoustic oscillations (BAO) signal due to the effects of large-scale bulk flows (Wang et al. 2013) as:

$$P_{\text{dw}}(k, \mu; z) = P_{\text{m}}^L(k; z) e^{-g_{\mu} k^2} + P_{\text{nw}}(k; z) (1 - e^{-g_{\mu} k^2}), \quad (4)$$

where $P_{\text{nw}}(k; z)$ is the ‘no-wiggle’ linear power spectrum and $P_{\text{m}}^L(k; z)$ is the linear matter power spectrum. The former is obtained by removing the BAO from the latter (Boyle & Komatsu

spect to EC20 by a factor ~ 4 in Λ CDM, while those of other cosmological parameters are only mildly changed.

2018), while the linear matter power spectrum is derived by an Einstein-Boltzmann numerical code, e.g. CAMB (Lewis et al. 2000) or CLASS (Blas et al. 2011). The amplitude of the non-linear damping factor is given by (Eisenstein et al. 2007)

$$g_\mu(z, \mu) = \sigma_v^2(z) \left[1 - \mu^2 + \mu^2 \left[1 + f_g(z) \right]^2 \right], \quad (5)$$

where $\sigma_v(z)$ is the galaxy velocity dispersion modelled analogously to $\sigma_p(z)$ in Eq. (2) with four parameters, one for each redshift bin (see EC20 for more details).

The total galaxy power spectrum in Eq. (2) includes the errors on redshift through the factor

$$F_z(k, \mu; z) = e^{-k^2 \mu^2 \sigma_z^2(z)}, \quad (6)$$

where $\sigma_z(z) = c(1+z)\sigma_{z,0}/H(z)$ and $\sigma_{z,0} = 0.001$ is the error on the measured redshift.

The last term in Eq. (2), $P_s(z)$, is the shot noise caused by the Poissonian distribution of measured galaxies on the smallest scales due to the finite total number of observed galaxies. For each bin, we model it with one contribution given by the fiducial inverse number density, plus a second nuisance parameter accounting for the residual shot noise.

The final Fisher matrix for the galaxy clustering observable for one redshift bin z_i is

$$F_{\alpha\beta}(z_i) = \frac{1}{8\pi^2} \int_{-1}^1 d\mu \int_{k_{\min}}^{k_{\max}} V_{\text{eff}}(k, \mu; z) \frac{\partial \ln P_{\text{obs}}(k, \mu; z_i)}{\partial p_\alpha} \times \frac{\partial \ln P_{\text{obs}}(k, \mu; z_i)}{\partial p_\beta} k^2 dk, \quad (7)$$

where $k_{\min} = 0.002 h \text{ Mpc}^{-1}$. The derivatives in Eq. (7) are evaluated at the parameter values of the fiducial model and V_{eff} is the effective volume of the survey given by

$$V_{\text{eff}}(k, \mu; z) = V_s(z) \left[\frac{n(z) P_{\text{obs}}(k, \mu; z)}{1 + n(z) P_{\text{obs}}(k, \mu; z)} \right]^2, \quad (8)$$

with $V_s(z)$ the volume of the survey and $n(z)$ the galaxy number density in a redshift bin.

2.2. Photometric galaxy clustering and weak lensing

Beyond the spectroscopic survey, *Euclid* will also perform a photometric survey, which will enable us to consider at least three main cosmological probes. These are galaxy clustering for galaxies with photometric redshifts, weak lensing, and their cross-correlations, also called galaxy-galaxy lensing. The combination of these three probes is commonly denoted as a 3×2 pt analysis. As for the spectroscopic case in the previous section, we closely follow the forecasting method and the tools presented in EC20. We refer the interested reader to this reference for all the details, but still provide a self-consistent description of the *Euclid* photometric probes below.

We consider as the main photometric observables the angular harmonic power spectra, $C_{ij}^{XY}(\ell)$, between two probes X and Y in two tomographic bins i and j . Under the Limber approximation and by setting the ℓ -dependent prefactor in the flat-sky limit to unity, these spectra can be expressed as

$$C_{ij}^{XY}(\ell) = c \int_{z_{\min}}^{z_{\max}} dz \frac{W_i^X(z) W_j^Y(z)}{H(z) r^2(z)} P_m^{\text{NL}}(k_\ell, z), \quad (9)$$

with $P_m^{\text{NL}}(k, z)$ the non-linear matter power spectrum evaluated at $k_\ell = (\ell + 1/2)/r(z)$, where $r(z)$ is the co-moving distance.² We further set $z_{\min} = 0.001$ and $z_{\max} = 4$, which is enough to cover the entire redshift range of the survey. The kernels for the photometric galaxy clustering and the weak lensing probes are, respectively,

$$W_i^G(z) = b_i(z) \frac{n_i(z) H(z)}{\bar{n}_i c}, \quad (10)$$

$$W_i^L(z) = \frac{3}{2} \Omega_m \frac{H_0^2}{c^2} (1+z) r(z) \int_z^{z_{\max}} dz' \frac{n_i(z') r(z') - r(z)}{\bar{n}_i r(z')} + W_i^{\text{IA}}(z), \quad (11)$$

where $n_i(z)/\bar{n}_i$ stands for the normalised galaxy distribution in the i -th bin and $b_i(z)$ denotes the galaxy bias for the same tomographic bin (see Sect. 3 of EC20 for more details).

Finally, the $W_i^{\text{IA}}(z)$ term contains the contribution of the intrinsic alignment of galaxies to weak lensing. As in EC20, we consider the extended non-linear alignment (eNLA) model with the window function

$$W_i^{\text{IA}}(z) = -\frac{\mathcal{A}_{\text{IA}} C_{\text{IA}} \Omega_m \mathcal{F}_{\text{IA}}(z) n_i(z) H(z)}{D(z) \bar{n}_i(z) c}, \quad (12)$$

where

$$\mathcal{F}_{\text{IA}}(z) = (1+z)^{\eta_{\text{IA}}} \left[\frac{\langle L \rangle(z)}{L_\star(z)} \right]^{\beta_{\text{IA}}}. \quad (13)$$

In the equation above, $\langle L \rangle(z)$ and $L_\star(z)$ are the redshift-dependent mean and the characteristic luminosity of source galaxies as computed from the luminosity function. The growth factor is represented by $D(z)$. As in EC20, we keep C_{IA} fixed to 0.0134 and we allow to vary the other three parameters of the eNLA model $\{\mathcal{A}_{\text{IA}}, \eta_{\text{IA}}, \beta_{\text{IA}}\}$ around their fiducial values $= \{1.72, -0.41, 2.17\}$.

We consider a Gaussian-only covariance whose elements are given by

$$\text{Cov} \left[C_{ij,\ell}^{\text{AB}}, C_{mn,\ell'}^{\text{CD}} \right] = \frac{\delta_{\ell\ell'}^{\text{K}}}{(2\ell+1) f_{\text{sky}} \Delta\ell} \times \left\{ \left[C_{im,\ell}^{\text{AC}} + \mathcal{N}_{im,\ell}^{\text{AC}} \right] \left[C_{jn,\ell'}^{\text{BD}} + \mathcal{N}_{jn,\ell'}^{\text{BD}} \right] + \left[C_{in,\ell}^{\text{AD}} + \mathcal{N}_{in,\ell}^{\text{AD}} \right] \left[C_{jm,\ell'}^{\text{BC}} + \mathcal{N}_{jm,\ell'}^{\text{BC}} \right] \right\}, \quad (14)$$

where the upper- and lower-case Latin indices run over L and G and all tomographic bins, respectively, $\delta_{\ell\ell'}^{\text{K}}$ is the Kronecker delta coming from the lack of correlation between different multipoles (ℓ, ℓ') , f_{sky} is the survey's sky fraction, and $\Delta\ell$ denotes the width of the logarithmic equi-spaced multipole bins. We consider a white noise,

$$\mathcal{N}_{ij,\ell}^{\text{LL}} = \frac{\delta_{ij}^{\text{K}}}{\bar{n}_i} \sigma_\epsilon^2, \quad \mathcal{N}_{ij,\ell}^{\text{GG}} = \frac{\delta_{ij}^{\text{K}}}{\bar{n}_i}, \quad \mathcal{N}_{ij,\ell}^{\text{GL}} = 0, \quad (15)$$

where σ_ϵ is the variance of observed ellipticities.

For evaluating the Fisher matrix $F_{\alpha\beta}^{\text{ph}}$ for the observed angular power spectrum, we use

$$F_{\alpha\beta}^{\text{ph}} = \sum_{\ell=\ell_{\min}}^{\ell_{\max}} \sum_{ij, mn} \frac{\partial C_{ij,\ell}^{\text{AB}}}{\partial \theta_\alpha} \text{Cov}^{-1} \left[C_{ij,\ell}^{\text{AB}}, C_{mn,\ell}^{\text{CD}} \right] \frac{\partial C_{mn,\ell}^{\text{CD}}}{\partial \theta_\beta}. \quad (16)$$

² As in EC20, and justified in Taylor et al. (2018), we use this formalism also for non-flat spatial geometries avoiding the introduction of hyper-spherical Bessel functions and non-Limber approximation by assuming that the changes in the cosmological parameters, the power spectrum, and the reduced window function are enough to capture the effect of a small non-zero spatial curvature.

2.3. Probe combination

We compute spectroscopic galaxy clustering (GC_{sp}), photometric galaxy clustering (GC_{ph}), weak lensing (WL), and cross-correlation between two photometric probes (XC) in two configurations: a pessimistic setting and an optimistic one, as in EC20. We consider $f_{sky} \approx 0.36$ for both of *Euclid*'s main probes (Euclid Collaboration: Scaramella et al. 2022). For the pessimistic setting, we set $k_{max} = 0.25 h \text{ Mpc}^{-1}$ for GC_{sp} , $\ell_{max} = 750$ for GC_{ph} and XC, and $\ell_{max} = 1500$ for WL. In addition, we impose a redshift cut of $z < 0.9$ on GC_{ph} to neglect any possible cross-correlation between the spectroscopic and photometric data when we combine the 3D GC_{sp} with the 3×2 pt. For the optimistic setting, we expand GC_{sp} to $k_{max} = 0.30 h \text{ Mpc}^{-1}$, GC_{ph} and XC to $\ell_{max} = 3000$, and WL to $\ell_{max} = 5000$, without imposing any redshift cut on GC_{ph} . For more details, see EC20.

For the cold dark matter isocurvature models in Sect. 5 that may be more susceptible to the details of their non-linear modeling, we also compute even more conservative results using a pessimistic quasilinear setting. That is $k_{max} = 0.15 h \text{ Mpc}^{-1}$ for GC_{sp} , $\ell_{max} = 750$ for WL, and $\ell_{max} = 500$ for GC_{ph} and XC.

We will consider the results obtained with the pessimistic setting as *the baseline* results. Where appropriate, we will also report the results with the EC20 optimistic setting to pair this with the other papers in this series (Euclid Collaboration: Casas et al. 2023; Euclid Collaboration: Frusciante et al. 2024; Euclid Collaboration: Ballardini et al. 2024).

3. Expected constraints on Ω_K

In this section, we present the results of the Fisher analysis for the cosmological parameters of interest corresponding to a non-flat Λ CDM,

$$\Theta_{\text{final}} = \{\Omega_m, \Omega_b, h, n_s, \Omega_K, \sigma_8\}, \quad (17)$$

after marginalisation over spectroscopic and photometric nuisance parameters.

Spatial flatness is one of the key predictions of the simplest slow-roll models of inflation, which have a stage of accelerated expansion sufficiently long to dilute pre-existing inhomogeneities and spatial curvature to undetectable levels. However, a non-zero spatial curvature larger than the standard deviation of $\sim 2 \times 10^{-5}$ for Ω_K due to inhomogeneities (Waterhouse & Zibin 2008) would have profound implications in terms of departures from the simplest slow-roll models: a negative curvature would support open inflation (Bucher et al. 1995), whereas a positive curvature would exclude false-vacuum eternal inflation and the simplest slow-roll models (Kleban & Schillo 2012).

The *Planck* measurements of CMB temperature, polarisation, and lensing anisotropies have constrained the spatial curvature at percent level: $\Omega_K = -0.011^{+0.013}_{-0.012}$ (Planck Collaboration: Aghanim et al. 2020b). This differs from the constraint $\Omega_K = -0.044^{+0.018}_{-0.015}$ (Planck Collaboration: Aghanim et al. 2020b) obtained from the combination of temperature and polarisation data only, as the *Planck* CMB lensing breaks the degeneracy between the total energy density and Ω_m (Efstathiou & Bond 1999) and reduces the allowed room for negative values.

The geometric information contained in the LSS breaks this CMB degeneracy between Ω_K and Ω_m more effectively. The completed SDSS-IV extended BAO survey alone and in combination with *Planck* measurements of CMB temperature and polarisation anisotropies gives, respectively, $\Omega_K = 0.078^{+0.086}_{-0.099}$ and $\Omega_K = -0.0001 \pm 0.0018$ (Alam et al. 2021). The DESI

BAO DR2 has updated these results to $\Omega_K = 0.025 \pm 0.041$ and $\Omega_K = 0.0023 \pm 0.0011$, alone and in combination with the CMB, respectively (DESI Collaboration: Abdul-Karim et al. 2025). The DES Y3 3×2 pt alone and in combination with *Planck*, BAO, and supernovae gives, respectively, $\Omega_K > -0.16$ at the 95% CL and $\Omega_K = 0.001 \pm 0.002$ at the 68% CL (DES Collaboration: Abbott et al. 2023).

For a fiducial value of $\Omega_K = 0$, the forecasted *Euclid* uncertainties obtained with Halofit (Takahashi et al. 2012) are displayed in detail in Table 1. The forecast uncertainty from GC_{sp} is $\sigma(\Omega_K) = 0.015$ (0.013) for the pessimistic (optimistic) setting. The photometric survey can provide tighter constraints: $\sigma(\Omega_K) = 0.0072$ (0.0039) for the pessimistic (optimistic) setting. Combining GC_{sp} with the 3×2 photometric information, i.e. WL+ GC_{ph} +XC, we find $\sigma(\Omega_K) = 0.0044$ (0.003) for the pessimistic (optimistic) setting. In the left and right panels of Fig. 1, we compare the expected constraints from GC_{sp} , WL+ GC_{ph} +XC, and their combination for the pessimistic and optimistic settings, respectively. *Euclid* alone has, therefore, the capability to squeeze the error on Ω_K an order of magnitude below the current constraint from galaxy surveys (Alam et al. 2021).

In Table 1, we show the constraints achievable from the combination of *Euclid* with CMB measurements. Following Euclid Collaboration: Ilić et al. (2022) – see Appendix A for a summary of their methodology – we consider the constraints expected from the combination of *Euclid* with *Planck*, SO, and CMB-S4. In Fig. 2, we show how the expected constraints from *Euclid* can break the CMB temperature and polarisation degeneracy in the (Ω_m, Ω_K) plane in the case of SO. We forecast $\sigma(\Omega_K) = 0.0009$ (0.0006) for the uncertainty on Ω_K in the pessimistic (optimistic) case from the combination of *Euclid*, SO, and *Planck*. Table 1 shows that these constraints are improved compared to those obtained from the combination of *Euclid* and *Planck* only and can be superseded by the combination with CMB-S4 and *Planck*.

4. Expected constraints on the scalar spectral index and its running

In this section, we forecast *Euclid*'s capability to constrain the scalar power spectrum when the scalar spectral index is assumed to have a non-zero running $\alpha_s \equiv dn_s/d \ln k$ (Kosowsky & Turner 1995), i.e.

$$\mathcal{P}_{\mathcal{R}}(k) = A_s \left(\frac{k}{k_*} \right)^{n_s - 1 + \frac{1}{2} \alpha_s \ln(k/k_*)}. \quad (18)$$

This expression includes the next-to-leading term in the Taylor expansion of $\ln \mathcal{P}_{\mathcal{R}}(k)$ in $\ln(k/k_*)$ with respect to the simplest power-law form in Eq. (1). In Eq. (18), we omit higher-order terms, such as the running of the running $\beta_s = d^2 n_s / d(\ln k)^2$, for simplicity. Both $n_s \neq 1$ and $\alpha_s \neq 0$ (as well as $\beta_s \neq 0$) are generic predictions of cosmic inflation and their values help in distinguishing among different models of inflation. However, in the simplest models characterised by an inflaton slowly rolling on a nearly flat potential, the running α_s is next-to-leading order with respect to the deviation from scale invariance, i.e. $n_s - 1$, in the parameters that characterise the slow-roll dynamics.³ As

³ Within the slow-roll approximation, $n_s - 1 \approx -2\epsilon_1 - \epsilon_2$, with $\epsilon_1 = -\dot{H}/H^2$ and $\epsilon_2 = \dot{\epsilon}_1/(H\epsilon_1)$ as the first two functions of the Hubble flow function (HFF) hierarchy. Analogously, always in the slow-roll approximation, we can write these deviations in terms of the slow-roll parameters $\epsilon = M_{pl}^2 V_\phi^2 / (2V^2)$ and $\eta = M_{pl}^2 V_{\phi\phi} / V$ (where $M_{pl} = (8\pi G)^{-1/2}$

Table 1. Fisher-matrix marginalised uncertainties on the cosmological parameters when the spatial curvature is allowed to vary in the pessimistic and optimistic settings and using *Euclid* observations GC_{sp}, WL+GC_{ph}+XC, and their combination. We quote absolute uncertainties for Ω_K (for the chosen fiducial value of $\Omega_K = 0$) and relative uncertainties for the other parameters (compared to their corresponding non-zero fiducial values).

$\Omega_K = 0$						
	Ω_m	Ω_b	h	n_s	Ω_K	σ_8
Pessimistic setting						
GC _{sp} ($k_{\max} = 0.25 h \text{ Mpc}^{-1}$)	1.6%	2.9%	2.5%	2.0%	0.015	0.99%
WL+GC _{ph} +XC	0.82%	6.1%	5.4%	2.9%	0.0072	0.44%
GC _{sp} +WL+GC _{ph} +XC ($z < 0.9$)	0.62%	1.8%	1.09%	0.47%	0.0044	0.32%
GC _{sp} +WL+GC _{ph} +XC ($z < 0.9$)+ <i>Planck</i> -like	0.47%	0.84%	0.35%	0.27%	0.0010	0.23%
GC _{sp} +WL+GC _{ph} +XC ($z < 0.9$)+SO-like+ <i>Planck</i> low- ℓ	0.43%	0.68%	0.32%	0.22%	0.0009	0.20%
GC _{sp} +WL+GC _{ph} +XC ($z < 0.9$)+S4-like+ <i>Planck</i> low- ℓ	0.38%	0.58%	0.28%	0.19%	0.0007	0.16%
Optimistic setting						
GC _{sp} ($k_{\max} = 0.3 h \text{ Mpc}^{-1}$)	1.6%	2.4%	1.92%	1.8%	0.013	0.96%
WL+GC _{ph} +XC	0.30%	4.6%	2.0%	0.37%	0.0039	0.14%
GC _{sp} +WL+GC _{ph} +XC	0.27%	1.6%	0.72%	0.19%	0.003	0.13%
GC _{sp} +WL+GC _{ph} +XC+ <i>Planck</i> -like	0.24%	0.59%	0.21%	0.15%	0.0007	0.11%
GC _{sp} +WL+GC _{ph} +XC+SO-like+ <i>Planck</i> low- ℓ	0.23%	0.44%	0.20%	0.14%	0.0006	0.11%
GC _{sp} +WL+GC _{ph} +XC+S4-like+ <i>Planck</i> low- ℓ	0.22%	0.38%	0.18%	0.12%	0.0006	0.10%

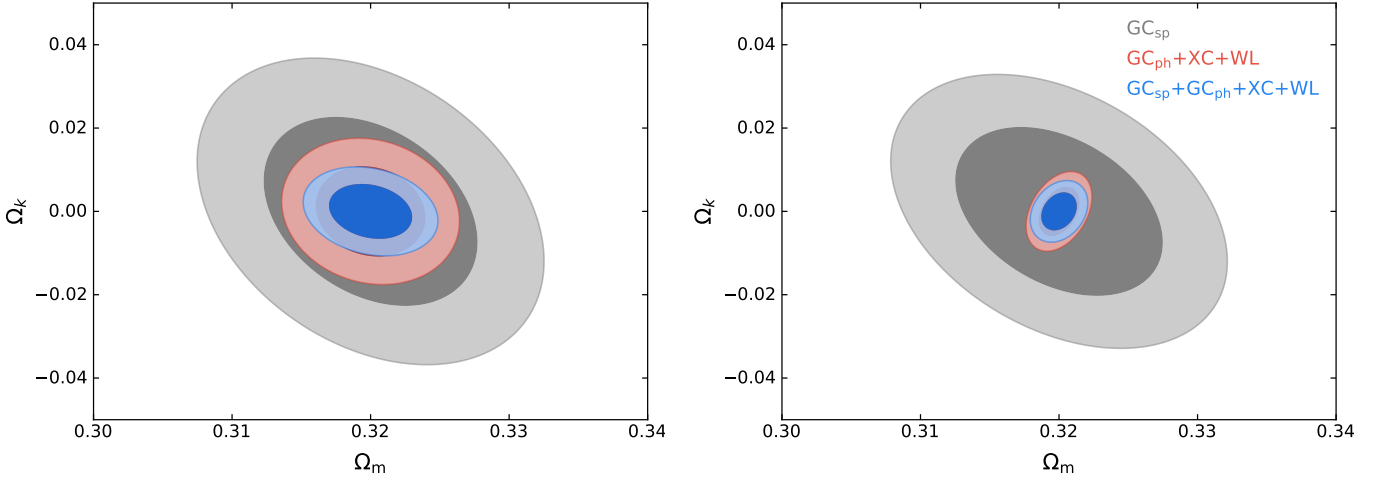


Fig. 1. *Euclid* Fisher-forecast marginalised two-dimensional contours for Ω_m and Ω_K . The left panel corresponds to the pessimistic setting for GC_{sp} (grey), WL+GC_{ph}+XC (red), and their combination (blue). The right panel shows the same constraints, but for the optimistic setting.

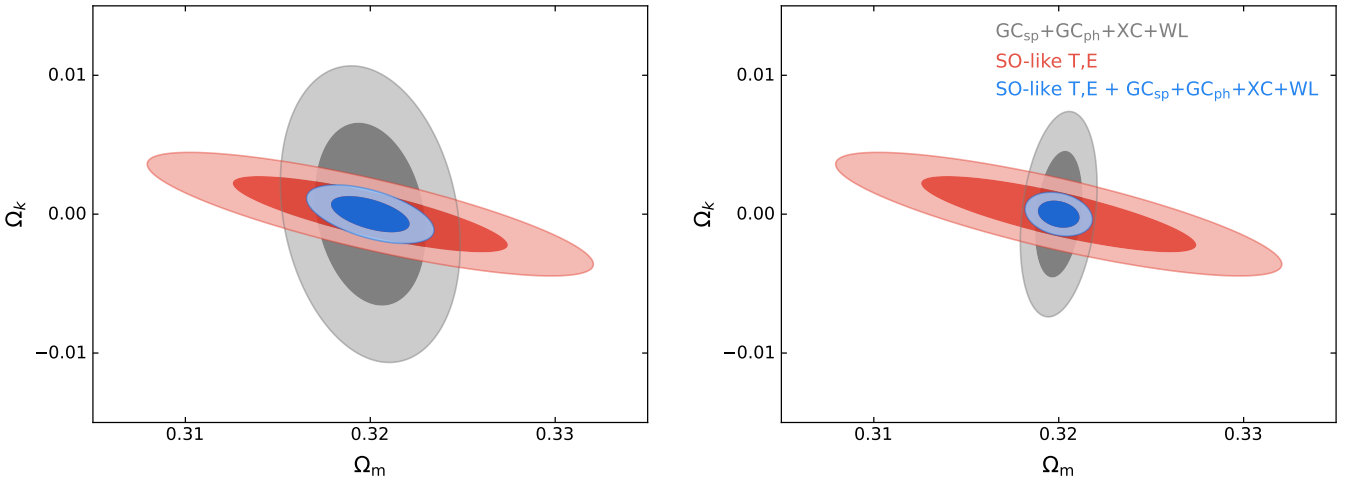


Fig. 2. Fisher-forecast marginalised two-dimensional contours for Ω_m and Ω_K from the combination of *Euclid* and CMB observations. The left panel corresponds to the pessimistic setting for *Euclid*'s GC_{sp}+WL+GC_{ph}+XC (grey), SO CMB temperature and polarisation (red), and their combination (blue). The right panel shows the same constraints, but for the optimistic setting.

a consequence, this scale dependence is suppressed compared to $n_s - 1$ and is expected to be $\lesssim 10^{-3}$ in the simplest single-field slow-roll models. On more general grounds, α_s is the next parameter to measure after the spectral index n_s of the power spectrum of scalar perturbations and its running, and is of utmost importance for inflation: a detection of $|\alpha_s| \gtrsim$ a few 10^{-3} would indicate new physics beyond the simplest models of inflation and a mild violation of slow roll even in single-field models.

Most of the cosmological observations are consistent with the key predictions of the simplest slow-roll inflationary models: deviation of the scalar spectral index from exact scale invariance $n_s - 1 \sim -0.035$ is measured at high statistical significance, while we usually have upper bounds on the absolute value of its running. The latest *Planck* CMB temperature and polarisation data provide a precise measurement of the spectral index, i.e. $n_s = 0.9635 \pm 0.0046$, and a tight constraint on its running, i.e. $\alpha_s = -0.0055 \pm 0.0067$ (Planck Collaboration: Aghanim et al. 2020b). Including a compilation of BAO measurements improves these results only marginally: $n_s = 0.9658 \pm 0.0041$ and $\alpha_s = -0.0049 \pm 0.0068$. We should, however, note that a non-zero running of $\alpha_s = -0.010 \pm 0.004$ may be the physical explanation alternative to unaccounted hidden systematics for the different spectral indices required to fit the Ly α and *Planck* data separately (Palanque-Desabrouille et al. 2020).

In order to model small scales relevant for galaxy surveys, we use a fitting formula designed to capture the enhancement in the power spectrum compared to the Λ CDM non-linear power spectrum as a function of the running of the scalar spectral index α_s . This fitting function has been calibrated using the NGenHalofit (Smith & Angulo 2019), which extends Halofit (Smith et al. 2003; Takahashi et al. 2012) to cosmologies that include a running spectral index,

$$\frac{P_m^{\text{NL}}(\alpha_s, k, z)}{P_m^{\text{NL}}(\alpha_s = 0, k, z)} = \left(\frac{k}{k_*}\right)^{\frac{1}{2}\alpha_s \ln(k/k_*)} \frac{1 + (1 + c_1 k) e^{c_2 k}}{2 + c_1 k}, \quad (19)$$

where c_1 and c_2 are quadratic polynomials in α_s and z . Fig. 3 shows the P_m^{NL} resulting from the prescription (19) compared to those obtained by NGenHalofit (Smith et al. 2003) or HMCode (Mead et al. 2015). We note that the differences at large scales are due to perturbation theory corrections to the smoothing of the BAO implemented in NGenHalofit. This non-linear modelling improves the theoretical treatment adopted in previous forecasts for α_s from galaxy surveys (Fedeli et al. 2010; Huang et al. 2012; Basse et al. 2015; Amendola et al. 2018; Ballardini et al. 2016; Muñoz et al. 2017; Bahr-Kalus et al. 2023), in particular at $k \gtrsim 0.2h/\text{Mpc}$.

Differently from the Ω_K case presented in the previous section, here we provide *Euclid* forecasts by choosing different non-zero fiducial values for the running of the spectral index consistent with current constraints. We present the results of the Fisher analysis for the cosmological parameters in the presence of a running spectral index,

$$\Theta_{\text{final}} = \{\Omega_m, \Omega_b, h, n_s, \alpha_s, \sigma_8\} \quad (20)$$

after marginalisation over spectroscopic and photometric nuisance parameters.

is the reduced Planck mass) related to the inflaton potential $V(\phi)$. The running of the spectral index is instead also related to the third HFF ϵ_3 , $\alpha_s \simeq -\epsilon_2 \epsilon_3 - 2\epsilon_1 \epsilon_3$, or equivalently to the third derivative of the potential through $\xi_V = M_{\text{pl}}^4 V_{\phi\phi\phi} V_\phi / V$, i.e. $\alpha_s \simeq -2\xi_V^2 + 16\epsilon_V \eta_V - 24\epsilon_V^2 - 2\xi_V^2$. See Auclair & Ringeval (2022); Ballardini et al. (2024) for third-order slow-roll expressions.

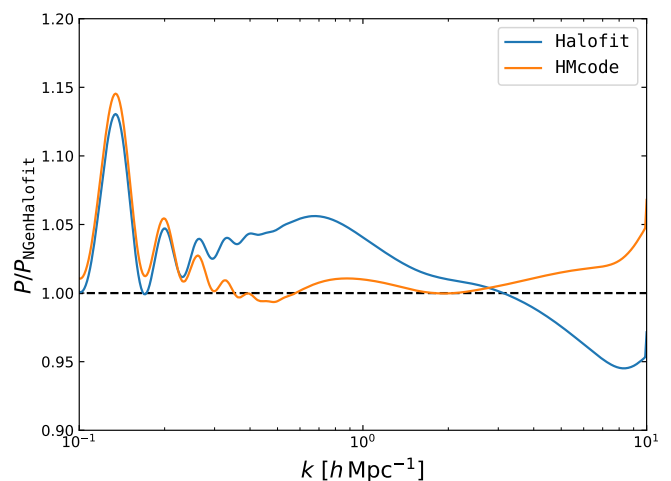


Fig. 3. Ratio of the non-linear matter power spectrum in Fourier space at redshift $z = 0$ with $\alpha_s = -0.01$ calculated using Halofit (blue line) and HMCode (orange line) to the non-linear matter power spectrum calculated using NGenHalofit.

Our results for the fiducial value $\alpha_s = -0.01$ are presented in Table 2. The relative uncertainties forecasted from GC_{sp} are 1.6% (1.5%) and 115% (91%) for n_s and α_s , respectively, with the pessimistic (optimistic) setting. The photometric survey provides tighter uncertainties compared to the spectroscopic survey only for α_s ; we obtain 2.0% (1.6%) and 57% (40%) for n_s and α_s , respectively, for the pessimistic (optimistic) setting (in qualitative agreement with the LSST forecasts presented in Ferté & Hong (2024), where it is possible to make a comparison). Combining GC_{sp} with the 3×2 photometric information, i.e. $\text{WL} + \text{GC}_{\text{ph}} + \text{XC}$, we find 0.78% (0.43%) and 53% (23%) for the pessimistic (optimistic) setting. Fig. 4 shows *Euclid*'s expected uncertainties in the (n_s, α_s) two-dimensional parameter space. These results imply that the uncertainty on the running expected from *Euclid* alone is comparable to or smaller than the current one based on *Planck* (Planck Collaboration: Akrami et al. 2020a). Therefore, *Euclid* alone will be sensitive to a value of the running of the scalar spectral index that is as large as $\alpha_s = -0.01$, but still consistent with the *Planck* constraints, at 2σ (4σ) for the pessimistic (optimistic) setting.

As in the case of spatial curvature, we also show in Table 2 the constraints that will be obtained by *Euclid* in combination with current and future CMB measurements. We find that *Euclid* with the pessimistic (optimistic) setting can reach a relative uncertainty of 23%, 14%, and 13% (13%, 11%, and 10%) in combination with *Planck*, SO, and CMB-S4, respectively. Fig. 5 shows, specifically, our forecasted marginalised two-dimensional contours for n_s and α_s from the combination of *Euclid* and SO measurements of the CMB temperature and polarisation.

In order to test the possible dependence of our Fisher results on the fiducial value, we repeat our analysis for $\alpha_s = -0.001$, a fiducial value that is smaller by one order of magnitude and closer to the typical values predicted by slow-roll inflation on the basis of the current measurements of n_s .⁴ The results are presented in Table 2 and show that the (absolute) uncertainty on the

⁴ In a similar way, different fiducial values have also been considered in *Euclid* forecasts for $f(R)$ cosmology (Euclid Collaboration: Casas et al. 2023) and for scale-independent modifications of gravity (Euclid Collaboration: Frusciante et al. 2024).

Table 2. Fisher-matrix marginalised uncertainties on the cosmological parameters relative to their corresponding fiducial values in the pessimistic and optimistic settings using *Euclid*'s observations GC_{sp}, WL+GC_{ph}+XC, and their combination when the running for the scalar spectral index is included.

$\alpha_s = -10^{-2}$						
	Ω_m	Ω_b	h	n_s	α_s	σ_8
Pessimistic setting						
GC _{sp} ($k_{\max} = 0.25 h \text{ Mpc}^{-1}$)	1.8%	3.1%	1.3%	1.6%	115%	1.0%
WL+GC _{ph} +XC	0.91%	6.1%	4.6%	2.0%	57%	0.45%
GC _{sp} +WL+GC _{ph} +XC($z < 0.9$)	0.81%	2.3%	0.62%	0.78%	53%	0.39%
GC _{sp} +WL+GC _{ph} +XC($z < 0.9$)+ <i>Planck</i> -like	0.35%	0.32%	0.24%	0.23%	23%	0.19%
GC _{sp} +WL+GC _{ph} +XC($z < 0.9$)+SO-like+ <i>Planck</i> low- ℓ	0.32%	0.095%	0.075%	0.21%	14%	0.18%
GC _{sp} +WL+GC _{ph} +XC($z < 0.9$)+CMB-S4+ <i>Planck</i> low- ℓ	0.30%	0.084%	0.067%	0.19%	13%	0.17%
Optimistic setting						
GC _{sp} ($k_{\max} = 0.3 h \text{ Mpc}^{-1}$)	1.7%	2.9%	1.1%	1.5%	91%	0.93%
WL+GC _{ph} +XC	0.30%	5.2%	4.1%	1.6%	40%	0.16%
GC _{sp} +WL+GC _{ph} +XC	0.28%	1.8%	0.47%	0.43%	23%	0.14%
GC _{sp} +WL+GC _{ph} +XC+ <i>Planck</i> -like	0.20%	0.28%	0.18%	0.17%	13%	0.11%
GC _{sp} +WL+GC _{ph} +XC+SO-like+ <i>Planck</i> low- ℓ	0.17%	0.084%	0.065%	0.16%	11%	0.090%
GC _{sp} +WL+GC _{ph} +XC+CMB-S4+ <i>Planck</i> low- ℓ	0.17%	0.076%	0.057%	0.15%	10%	0.089%
$\alpha_s = -10^{-3}$						
	Ω_m	Ω_b	h	n_s	α_s	σ_8
Pessimistic setting						
GC _{sp} ($k_{\max} = 0.25 h \text{ Mpc}^{-1}$)	1.0%	1.7%	1.3%	1.2%	1130%	0.75%
WL+GC _{ph} +XC	0.92%	6.0%	4.6%	2.0%	569%	0.43%
GC _{sp} +WL+GC _{ph} +XC($z < 0.9$)	0.62%	1.3%	0.58%	0.58%	418%	0.28%
GC _{sp} +WL+GC _{ph} +XC($z < 0.9$)+ <i>Planck</i> -like	0.32%	0.32%	0.24%	0.22%	215%	0.17%
GC _{sp} +WL+GC _{ph} +XC($z < 0.9$)+SO-like+ <i>Planck</i> low- ℓ	0.29%	0.094%	0.073%	0.20%	123%	0.16%
GC _{sp} +WL+GC _{ph} +XC($z < 0.9$)+CMB-S4+ <i>Planck</i> low- ℓ	0.27%	0.083%	0.065%	0.18%	118%	0.16%
Optimistic setting						
GC _{sp} ($k_{\max} = 0.3 h \text{ Mpc}^{-1}$)	1.0%	1.6%	1.1%	1.1%	858%	0.69%
WL+GC _{ph} +XC	0.27%	4.7%	3.2%	1.2%	241%	0.13%
GC _{sp} +WL+GC _{ph} +XC	0.25%	1.2%	0.046%	0.36%	154%	0.11%
GC _{sp} +WL+GC _{ph} +XC+ <i>Planck</i> -like	0.19%	0.29%	0.18%	0.17%	116%	0.096%
GC _{sp} +WL+GC _{ph} +XC+SO-like+ <i>Planck</i> low- ℓ	0.16%	0.083%	0.066%	0.15%	99%	0.082%
GC _{sp} +WL+GC _{ph} +XC+CMB-S4+ <i>Planck</i> low- ℓ	0.15%	0.075%	0.058%	0.14%	96%	0.080%

running is quite stable with respect to the change in the fiducial value by an order of magnitude. Consequently, it is difficult to detect a running as small as $\alpha_s = -0.001$ with *Euclid* or with any of the studied combinations of *Euclid* and CMB observations.

5. Expected constraints on isocurvature contribution

In the minimal scenario, primordial perturbations are assumed to be purely adiabatic, i.e. perturbations in the spatial curvature (see, e.g., Bardeen et al. 1983). In this case, the total energy density of the Universe—and thus its spatial curvature—can vary from point to point on super-Hubble scales, while the relative abundances of the different species (e.g., the photon-to-cold dark matter ratio) remain spatially uniform. The simplest single-field inflationary models naturally generate only this type of perturbation.

However, in more general multi-field inflationary models, there are more degrees of freedom, and orthogonal modes, i.e. isocurvature perturbations, can also be excited (Linde 1985; Efstathiou & Bond 1986; Sasaki & Stewart 1996; García-Bellido & Wands 1996; Peebles 1999). These isocurvature perturbations generated during inflation can survive after inflation as fluctuations in the composition of the Universe, where the ratios be-

tween species vary spatially, even though the total energy density remains spatially uniform on super-Hubble scales.

This means that the detection of isocurvature modes would be a smoking gun for models beyond the simplest single-field inflation. Moreover, if the trajectory or the kinetic manifold in field space is curved then the curvature and isocurvature perturbations can be correlated (Langlois 1999; Langlois & Riazuelo 2000; Gordon et al. 2000; di Marco et al. 2003; Amendola et al. 2002; Väliiviita & Muhonen 2003; Byrnes & Wands 2006).

5.1. Motivation and background

Here we focus on one isocurvature mode out of four theoretically possible ones (Bucher et al. 2000), the cold dark matter density isocurvature (CDI) perturbation⁵ for which

$$\mathcal{I}_{c\gamma} = \delta_c - \frac{3}{4}\delta_\gamma \quad (21)$$

is non-zero, i.e. varies spatially (unlike in the pure adiabatic case). Here, $\delta_\gamma = \delta\rho_\gamma/\bar{\rho}_\gamma$ is the density perturbation of photons

⁵ The CDI mode is observationally similar to the baryon isocurvature mode. Indeed, the CMB and matter power spectra depend on the total matter isocurvature $\mathcal{I}_{m\gamma} = \frac{\Omega_b}{\Omega_m}\mathcal{I}_{b\gamma} + \frac{\Omega_c}{\Omega_m}\mathcal{I}_{c\gamma}$, where $\mathcal{I}_{b\gamma} = \delta_b - \frac{3}{4}\delta_\gamma$. Thus, our results on the CDI can easily be converted to the constraints on the total matter isocurvature or baryon isocurvature.

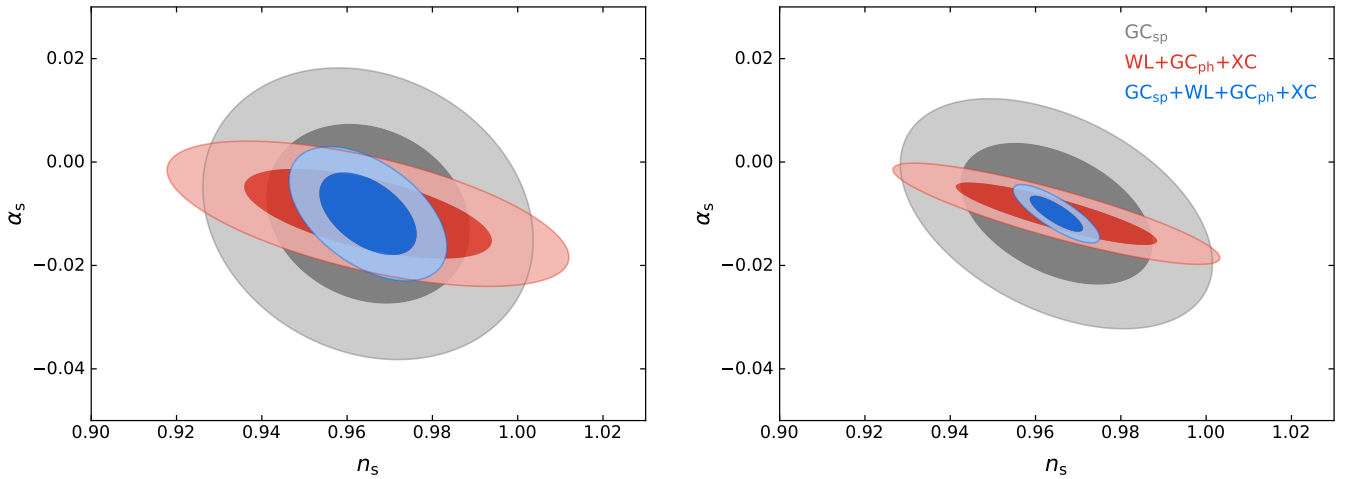


Fig. 4. *Euclid* Fisher-forecast marginalised two-dimensional contours for n_s and α_s . The left panel corresponds to the pessimistic setting for GC_{sp} (grey), $WL+GC_{ph}+XC$ (red), and their combination (blue). The right panel shows the same constraints, but for the optimistic setting.

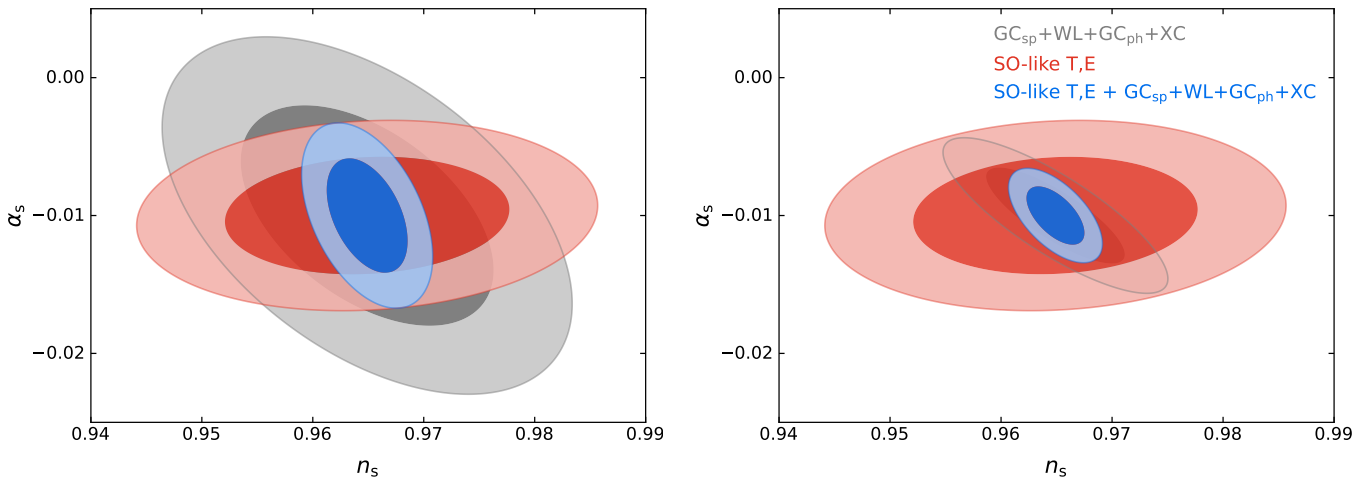


Fig. 5. Fisher-forecast marginalised two-dimensional contours for n_s and α_s from the combination of *Euclid* and CMB observations. The left panel corresponds to the pessimistic setting for *Euclid*'s $GC_{sp}+WL+GC_{ph}+XC$ (grey), SO CMB temperature and polarisation (red), and their combination (blue). The right panel shows the same constraints, but for the optimistic setting.

and δ_c is the density perturbation of cold dark matter. From now on, we ignore the subscripts in \mathcal{I}_{cy} .

CMB observations indicate that on scales corresponding to $0.001 \text{ Mpc}^{-1} \lesssim k \lesssim 0.05 \text{ Mpc}^{-1}$ the primordial perturbations are predominantly adiabatic and mildly red-tilted, with $n_s \approx 0.964$ (Planck Collaboration: Akrami et al. 2020a), which coincides with one of the predictions of single-field slow-roll inflation. However, there is no similar restriction for a CDI isocurvature contribution on which we have only upper bounds (Planck Collaboration: Akrami et al. 2020a). The isocurvature spectrum, e.g. from multi-field inflation, can be blue-tilted (more perturbation power at small scales than at large scales), i.e. $n_{iso} > 1$ (Polarski & Starobinsky 1994; Linde & Mukhanov 1997) and, on the other hand, the CMB observations are not very sensitive to even a dominant isocurvature contribution at $k \gtrsim 0.05 \text{ Mpc}^{-1}$. Here the LSS observations can significantly improve the constraints or lead to a detection.

A strong dark matter candidate, the axion (Weinberg 1978; Wilczek 1978; Axenides et al. 1983), can acquire even very blue-tilted ($n_{iso} \sim 2-4$) isocurvature perturbations (Kasuya &

Kawasaki 2009; Kobayashi & Takahashi 2016; Chung & Upadhye 2018; Chung & Chaitanya Tadepalli 2023), though at some small scale the spectrum should flatten. For reviews on the axion, see e.g. Kawasaki & Nakayama (2013); Marsh (2016). Super-heavy dark matter or WIMPzilla is another example of a model that could produce a blue-tilted isocurvature spectrum and for which the detection of the isocurvature mode could be a smoking gun (Chung et al. 2005; Kolb & Long 2017).

In these cases with a blue-tilted isocurvature spectrum, the adiabatic and isocurvature perturbations would be uncorrelated. Note that this possibility is very different from the standard curvaton case (Mollerach 1990; Enqvist & Sloth 2002; Moroi & Takahashi 2001; Lyth & Wands 2002; Bartolo & Liddle 2002; Lyth et al. 2003; Gordon & Lewis 2003; Langlois et al. 2008). Indeed, a generic feature of almost all curvaton models is that the adiabatic and isocurvature spectral indices are equal, since both perturbations arise from the same source in these models. As the existing data constrain the adiabatic spectral index near the value of 0.964, the curvaton models do not offer a large isocurvature

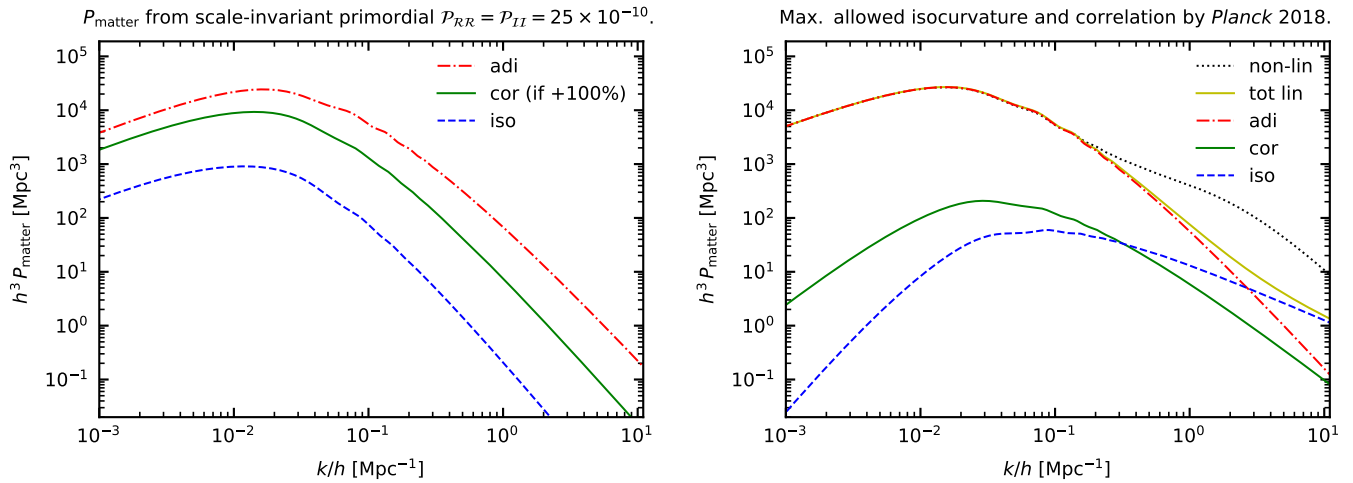


Fig. 6. Matter power spectra at redshift $z = 0$. The left panel shows the linear matter power spectrum today, if the primordial perturbations are scale-invariant pure adiabatic perturbations with amplitude $\mathcal{P}_{\mathcal{R}\mathcal{R}} = 25 \times 10^{-10}$ (red dotted-dashed), or if the primordial perturbations are scale-invariant pure cold dark matter isocurvature perturbations with amplitude $\mathcal{P}_{\mathcal{I}\mathcal{I}} = 25 \times 10^{-10}$ (blue dashed), and the resulting correlation component to the matter power spectrum if there are these two components and they are +100% correlated with each other (green solid). The right panel shows the fiducial model used in the case of “maximum 2σ allowed by *Planck*.” The linear total matter power spectrum (tot lin) is the sum of the adiabatic (adi) and blue-tilted isocurvature (iso) contributions, and their $\sim 10\%$ correlation (cor). This (tot lin) is then corrected by Halofit to approximate the non-linear spectrum (non-lin) of the fiducial model.

signal to the CMB or matter power spectra at high k , contrary to the blue-tilted axion or WIMPzilla models.

5.2. CDI models we consider and their observational aspects

We assume the standard, spatially flat, Λ CDM cosmology and that the primordial power spectra of the adiabatic perturbation, \mathcal{R} , and the CDI perturbation, \mathcal{I} , obey independent power-law forms

$$\mathcal{P}_{\mathcal{R}\mathcal{R}}(k) = \mathcal{P}_{\mathcal{R}\mathcal{R}}(k_*) \left(\frac{k}{k_*}\right)^{n_{\text{adi}}-1}, \quad \mathcal{P}_{\mathcal{I}\mathcal{I}}(k) = \mathcal{P}_{\mathcal{I}\mathcal{I}}(k_*) \left(\frac{k}{k_*}\right)^{n_{\text{iso}}-1}, \quad (22)$$

with their correlation power spectrum

$$\mathcal{P}_{\mathcal{R}\mathcal{I}}(k) = \mathcal{P}_{\mathcal{R}\mathcal{I}}(k_*) \left(\frac{k}{k_*}\right)^{n_{\text{cor}}-1}, \quad (23)$$

where $n_{\text{cor}} = (n_{\text{adi}} + n_{\text{iso}})/2$. Here we have five parameters: three amplitudes $\mathcal{P}_{\mathcal{R}\mathcal{R}}(k_*)$, $\mathcal{P}_{\mathcal{I}\mathcal{I}}(k_*)$, and $\mathcal{P}_{\mathcal{R}\mathcal{I}}(k_*)$ at the pivot scale $k_* = 0.05 \text{ Mpc}^{-1}$, and two independent constant spectral indices n_{adi} and n_{iso} . Each spectrum is a straight line (with a slope $n - 1$) in the $[\ln(k/k_*), \ln \mathcal{P}]$ space. However, in this parametrisation the adiabatic model would be recovered with any n_{iso} as long as the amplitudes $\mathcal{P}_{\mathcal{I}\mathcal{I}}(k_*)$ and $\mathcal{P}_{\mathcal{R}\mathcal{I}}(k_*)$ are zero. In the absence of detection of a non-zero isocurvature amplitude this parametrisation becomes problematic because the “adiabatic parameter space volume” would be arbitrarily large, i.e. the adiabatic model would not be a single point in the space of the extended parameters. Thus, we parametrise the perturbations mathematically equivalently by five amplitudes given at two scales⁶ $k_1 = 0.002 \text{ Mpc}^{-1}$ and $k_2 = 0.1 \text{ Mpc}^{-1}$:

$$\mathcal{P}_{\mathcal{R}\mathcal{R}1}, \quad \mathcal{P}_{\mathcal{R}\mathcal{R}2}, \quad \mathcal{P}_{\mathcal{I}\mathcal{I}1}, \quad \mathcal{P}_{\mathcal{I}\mathcal{I}2}, \quad \text{and} \quad \mathcal{P}_{\mathcal{R}\mathcal{I}1}. \quad (24)$$

⁶ Our choices for the fiducial models assume $h = 0.674$, so $k_1 \approx 0.003 \text{ h Mpc}^{-1}$ and $k_2 \approx 0.15 \text{ h Mpc}^{-1}$.

The first four of these are non-negative, whereas the correlation can be positive, negative, or zero. (In this parametrisation, the adiabatic model is simply recovered by setting all the extra isocurvature parameters $\mathcal{P}_{\mathcal{I}\mathcal{I}1}$, $\mathcal{P}_{\mathcal{I}\mathcal{I}2}$, and $\mathcal{P}_{\mathcal{R}\mathcal{I}1}$ to zero.) In addition, we can calculate derived parameters, such as the primordial isocurvature fraction $\beta_{\text{iso}}(k) = \mathcal{P}_{\mathcal{I}\mathcal{I}}(k) / [\mathcal{P}_{\mathcal{R}\mathcal{R}}(k) + \mathcal{P}_{\mathcal{I}\mathcal{I}}(k)]$, which can depend on k and is in the range $(0, 1)$, and the primordial correlation fraction $\cos \Delta = \mathcal{P}_{\mathcal{R}\mathcal{I}} / (\mathcal{P}_{\mathcal{R}\mathcal{R}} \mathcal{P}_{\mathcal{I}\mathcal{I}})^{1/2}$, which is constant in k and in the range $(-1, 1)$. For details, see [Planck Collaboration: Ade et al. \(2016\)](#) and [Planck Collaboration: Akrami et al. \(2020a\)](#).

The CDI mode is constrained by the *Planck* CMB angular power spectra $C_\ell^{TT,TE,EE}$ on large scales (corresponding to $k \sim k_1$) and medium scales (corresponding to $k \sim k_2$) to be less than a few percent of the dominant adiabatic mode. However, if the adiabatic and CDI modes had the same spectral index of primordial perturbations, i.e. $n_{\text{iso}} = n_{\text{adi}}$, the observational effects of the CDI mode would be damped compared to the adiabatic one at smaller scales, i.e., at larger multipoles or wavenumbers by $C_{\ell, \text{CDI}} / C_{\ell, \text{ADI}} \propto (\ell / \ell_{\text{eq}})^{-2} \sim (k / k_{\text{eq}})^{-2}$, where in the latter we refer to the scale that re-entered the Hubble radius at the radiation–matter equality. Hence, the constraints at the smallest scales ($k \sim k_2$) probed by *Planck* remain weaker, allowing for a spectral index as large as $n_{\text{iso}} \sim 2.9$. At $k = k_2 = 0.1 \text{ Mpc}^{-1}$ the *Planck* CMB temperature and polarisation data give a 95% CL upper bound on the ratio of the primordial isocurvature power to the curvature perturbation power $\mathcal{P}_{\mathcal{I}\mathcal{I}} / \mathcal{P}_{\mathcal{R}\mathcal{R}} \lesssim 1.4$, i.e., $\beta_{\text{iso}}(k_2) < 0.58$, which tightens to $\beta_{\text{iso}}(k_2) < 0.47$ when the *Planck* CMB lensing data are included. This is the region of parameter space for the CDI mode in which we expect *Euclid* to significantly improve the current CMB constraints.

However, one should keep in mind that the isocurvature contribution is also damped (compared to the primordial ratio $\mathcal{P}_{\mathcal{I}\mathcal{I}} / \mathcal{P}_{\mathcal{R}\mathcal{R}}$) in the LSS observables. The left panel of Fig. 6 shows the linear matter power spectra P_m (at redshift $z = 0$) resulting from scale-invariant adiabatic and isocurvature perturbations of the same primordial amplitude $\mathcal{P}_{\mathcal{R}\mathcal{R}}(k) = 25 \times 10^{-10}$ and

Table 3. Fisher-matrix 68.3% CL marginalised uncertainties in the pessimistic setting on the cosmological parameters, relative to their corresponding fiducial values, when the “maximum 2σ allowed by *Planck*”, “scale-invariant uncorrelated isocurvature contribution”, or “blue-tilted uncorrelated isocurvature contribution” is respectively included. In Case 2 and Case 3, the fiducial model has a zero isocurvature contribution, and consequently, instead of the percent-level error with respect to the fiducial value, we report the 68.3% (1σ) upper limit for $10^{10}\mathcal{P}_{II1}$. Case 2 and Case 3 have only one isocurvature parameter, $10^{10}\mathcal{P}_{II1}$. Thus, we indicate in square brackets the “derived” value of $10^{10}\mathcal{P}_{II2} = 10^{10}\mathcal{P}_{II1}$ in Case 2 and $10^{10}\mathcal{P}_{II2} = 1690.6 \times 10^{10}\mathcal{P}_{II1}$ in Case 3. In the last column, we report the corresponding isocurvature fraction at $k_2 = 0.1 \text{ Mpc}^{-1}$ calculated from the other values by $\beta_{\text{iso}2} = \mathcal{P}_{II2}/(\mathcal{P}_{II2} + \mathcal{P}_{\mathcal{R}\mathcal{R}2, \text{fiducial}})$. Here square brackets indicate that this only corresponds to the other values, not a 68.3% CL marginalised uncertainty for $\beta_{\text{iso}2}$, which would have a highly non-Gaussian posterior in these cases where \mathcal{P}_{II2} is of the same order of magnitude as $\mathcal{P}_{\mathcal{R}\mathcal{R}2}$.

Case 1: Maximum 2σ allowed by <i>Planck</i> isocurvature and correlation contribution at k_2								
	Ω_m	Ω_b	h	$10^{10}\mathcal{P}_{\mathcal{R}\mathcal{R}1}$	$10^{10}\mathcal{P}_{\mathcal{R}\mathcal{R}2}$	$10^{10}\mathcal{P}_{II1}$	$10^{10}\mathcal{P}_{II2}$	$10^{10}\mathcal{P}_{\mathcal{R}I1}$
Fiducial value	0.315	0.049	0.674	28.990	19.449	0.017	30.916	0.076
GC _{sp} ($k_{\text{max}} = 0.25 h \text{ Mpc}^{-1}$)	1.0%	2.4%	1.0%	2.1%	1.5%	39.0%	32.5%	35.8%
WL+GC _{ph} +XC	0.9%	7.7%	6.2%	3.3%	12.5%	338.9%	180.5%	162.1%
GC _{sp} +WL+GC _{ph} +XC	0.3%	2.0%	0.9%	1.1%	1.3%	31.4%	16.0%	26.4%
Case 2: Scale-invariant ($n_{\text{iso}} = 1.0$) uncorrelated isocurvature contribution; fiducial $\mathcal{P}_{II1} = 0$								
	Ω_m	Ω_b	h	$10^{10}\mathcal{P}_{\mathcal{R}\mathcal{R}1}$	$10^{10}\mathcal{P}_{\mathcal{R}\mathcal{R}2}$	$10^{10}\mathcal{P}_{II1}$	$[10^{10}\mathcal{P}_{II2}]$	$[\beta_{\text{iso}2}]$
Fiducial value	0.315	0.049	0.674	23.551	20.529	0	[0]	[0]
GC _{sp} ($k_{\text{max}} = 0.25 h \text{ Mpc}^{-1}$)	1.4%	2.2%	1.2%	5.7%	1.7%	19.0	[19.0]	[0.48]
WL+GC _{ph} +XC	0.9%	6.0%	4.5%	6.7%	9.3%	24.7	[24.7]	[0.55]
GC _{sp} +WL+GC _{ph} +XC	0.6%	1.5%	0.8%	2.5%	1.4%	9.4	[9.4]	[0.31]
Case 3: Blue-tilted ($n_{\text{iso}} = 2.9$) uncorrelated isocurvature contribution; fiducial $\mathcal{P}_{II1} = 0$								
GC _{sp} ($k_{\text{max}} = 0.25 h \text{ Mpc}^{-1}$)	1.5%	2.2%	1.2%	2.7%	2.2%	0.0200	[33.7]	[0.62]
WL+GC _{ph} +XC	0.8%	6.3%	4.8%	1.7%	7.9%	0.0011	[1.9]	[0.08]
GC _{sp} +WL+GC _{ph} +XC	0.6%	1.5%	0.8%	1.0%	1.1%	0.0005	[0.9]	[0.04]
Adiabatic Λ CDM								
GC _{sp} ($k_{\text{max}} = 0.25 h \text{ Mpc}^{-1}$)	1.4%	2.2%	1.2%	2.5%	1.3%			
WL+GC _{ph} +XC	0.8%	4.9%	2.7%	1.5%	3.7%			
GC _{sp} +WL+GC _{ph} +XC	0.6%	1.4%	0.8%	1.0%	1.0%			

$\mathcal{P}_{II}(k) = 25 \times 10^{-10}$. In addition, a (possible) 100% correlation ($\cos \Delta = 1$) is indicated. In this case, the observable CDI to adiabatic ratio in the matter power spectrum would be $P_m^{\text{iso}}/P_m^{\text{adi}} \approx 1/13$ at $k/h = 0.002 \text{ Mpc}^{-1}$ and $1/54$ at $k/h = 0.1 \text{ Mpc}^{-1}$, and only $1/244$ at $k/h = 1 \text{ Mpc}^{-1}$. The observable effects (among others the modification of the baryon acoustic peak structure) are maximised in the case of a 100% correlation, which would, in this example, give approximately $1/2$, $1/4$, and $1/8$ contribution, respectively, to the total at the above-mentioned scales. It should be underlined that apart from modifying the overall shape of the matter power spectrum, as is immediately visible in the right panel of Fig. 6, the CDI and correlation contributions slightly shift the positions (and alter the heights) of BAO peaks in the matter power with respect to the pure adiabatic case (see, e.g., Fig. 15 of Väiviita et al. 2012). All this is automatically taken into account by our Fisher forecast codes. If the actual Universe had some isocurvature but the pure adiabatic model were fitted to the data, then the interpreted values of the standard cosmological and dark energy parameters might be biased (Muya Kasanda et al. 2012), but as already Mangilli et al. (2010) forecasted (and our results confirm it) the error bars on the standard parameters would not be significantly affected by the extra degrees of freedom. The use of the combination of CMB and LSS observations will reduce the risk of biased results for the standard parameters and would simultaneously optimally constrain the isocurvature parameters.

If the spectral index of primordial isocurvature perturbations is $n_{\text{iso}} \approx n_{\text{adi}} + 0.5$, then the isocurvature to adiabatic ratio in

the observable matter power spectrum stays nearly constant over all wavenumbers. (This can easily be checked by reproducing, e.g. by CAMB, the left panel of Fig. 6, but with $n_{\text{iso}} = 1.5$ and plotting the isocurvature to adiabatic ratio.) Therefore, if the data were adiabatic and had the same constraining power at every k in the considered range, then the minimum “disturbance” would be achieved with this n_{iso} . The result is that if the overall isocurvature contribution were to be minimised over the whole data, the posterior probability density function would apparently favour $n_{\text{iso}} \sim 1.46$. (In the case of the CMB the similar relation is $n_{\text{iso}} \sim n_{\text{adi}} + 2$.) On the other hand, this means that *Euclid* has very little constraining power on those CDI models whose spectral index is $n_{\text{iso}} \lesssim 1.46$. Only for $n_{\text{iso}} > 1.5$ does *Euclid* have the potential to considerably improve the constraints over the existing CMB constraints.

We present *Euclid* forecasts for three different isocurvature cases:

Case 1: The observable effects are the largest for the CDI spectra that are primordially blue-tilted and/or positively correlated with the primordial adiabatic perturbations. Hence, we first derive *Euclid* forecasts for a positively correlated blue-tilted CDI model that lies in terms of the isocurvature contribution close to the maximum 95% CL allowed region, as well as has the maximum allowed correlation by *Planck*. This model has $\beta_{\text{iso}}(k_1) = 0.00059$, $\beta_{\text{iso}}(k_2) = 0.6$, and $\cos \Delta = 0.108$ giving $n_{\text{iso}} = 2.9$, $n_{\text{cor}} = 1.9$, and $\beta_{\text{iso}}(k_*) = 0.28$ or $\mathcal{P}_{II}(k_*)/\mathcal{P}_{\mathcal{R}\mathcal{R}}(k_*) = 0.39$. The

values of cosmological parameters⁷ used to produce this “maximum 2σ allowed by *Planck*” fiducial model are presented in Table 3. The contributions to the matter power spectrum in this model are presented in the right panel of Fig. 6. The total linear matter power, which is the sum of the CDI, correlation, and adiabatic components, differs visibly from the pure adiabatic one from $k/h \approx 0.1 \text{ Mpc}^{-1}$ onward, where $P_m^{\text{tot lin}}/P_m^{\text{adi}} \approx 1.033$. At $k/h = 0.3 \text{ Mpc}^{-1}$, the ratio is 1.089. The effects of this magnitude should be detectable by *Euclid*. We also show the total linear spectrum run through Halofit (setting `halofit_version = 4` in CAMB) to estimate the resulting total non-linear matter power spectrum. This is used in the WL+GC_{ph}+XC analysis and has been shown to be inaccurate in the case of extreme isocurvature spectral indices, $n_{\text{iso}} \geq 3$, studied in detail by Chung et al. (2023). However, our fiducial n_{iso} is more modest, and when doing the Fisher forecasts we are dealing with models in the vicinity of the fiducial model, and hence even if the non-linearities were modelled slightly inaccurately, these should not considerably affect the results. We also report results with an extra conservative quasilinear setting, leaving the full non-linear modelling of admixtures of nearly scale-invariant adiabatic contribution and a highly blue-tilted isocurvature contribution for future N-body simulations. It is important to note that on sub-Hubble scales there is no isocurvature left, which means that the simulations themselves could be the standard ones as long as adiabatic initial conditions with a linear spectrum similar to the yellow curve (“tot lin”) in the right panel of Fig. 6 were specified at a redshift 50–100 instead of the ones similar to the standard red curve (“adi”).

Case 2: In our second isocurvature case we go to the opposite extreme. Our fiducial model is now adiabatic Λ CDM and we forecast a model that has only one isocurvature parameter, a scale-invariant amplitude \mathcal{P}_{II} , i.e. we have $n_{\text{iso}} = 1$ and no correlation between the CDI and the adiabatic components. As explained above, due to the damping of the primordial CDI component, *Euclid* is expected to be relatively insensitive to this type of CDI contribution. In addition, here we can safely use the standard adiabatic non-linear modelling and have high confidence in the results even in the optimistic case that picks contributions from high k (because the isocurvature contribution decreases rapidly towards high k).

Case 3: In our third isocurvature case we keep the adiabatic Λ CDM fiducial model and forecast the expected constraint for an isocurvature fraction with a fixed spectral index $n_{\text{iso}} = 2.9$. Unlike in Case 1, we consider zero correlation. This case most directly answers the question of how much *Euclid* can improve over the *Planck* isocurvature constraints, if the true underlying Universe has adiabatic primordial perturbations. This case is most sensitive to the non-linear scales and, therefore, to non-linear modelling, as the fiducial model is the standard adiabatic model, but then we add to this a blue-tilted component whose contribution grows rapidly towards small scales. For GC_{sp} we impose three different k cuts and see that, as expected, the con-

straints improve as a function of k cut. For WL+GC_{ph}+XC the situation is more complicated as some contribution from very high k enters to the constraints no matter how aggressive an ℓ cut one imposes because $P_m(k)$ is not rapidly decreasing as in the pure adiabatic case or in the $n_{\text{iso}} = 1$ case (see Fig. 7). Thus, we deem, in particular, forecasts with the optimistic setting for WL+GC_{ph}+XC with $n_{\text{iso}} = 2.9$ in Fig. 8 less reliable than the other results.

5.3. Euclid forecasts for the CDI mode

We report the fiducial parameter values and our forecasts with the pessimistic setting for the above three isocurvature cases in Table 3. For comparison, we show the standard adiabatic results which indicate that allowing for an isocurvature contribution does not significantly affect the 1σ uncertainty of the background density parameters Ω_m , Ω_b , nor the current expansion rate h with GC_{sp}. However, when using WL+GC_{ph}+XC, the parameters Ω_b and, in particular, h are somewhat degenerate with the isocurvature parameters, and hence their uncertainty increases with respect to the adiabatic case. The same is true for the amplitude of adiabatic perturbations ($\mathcal{P}_{\mathcal{RR}1}$ and $\mathcal{P}_{\mathcal{RR}2}$). A smaller primordial adiabatic amplitude can fit the data since part of the perturbation power comes from the isocurvature perturbations.

The results of Table 3 for \mathcal{P}_{II2} with the pessimistic setting are displayed in Fig. 8. For comparison, this figure shows the results for more conservative quasilinear settings and for the optimistic setting. Apart from Case 3 ($n_{\text{iso}} = 2.9$), the dependence on k_{max} or ℓ_{max} is moderate. This fact was expected for Case 2 since the isocurvature contribution with $n_{\text{iso}} = 1.0$ rapidly decreases towards high k and hence adding information at higher k only mildly improves the constraints. For Case 1, the fiducial model has a large blue-tilted isocurvature contribution and including higher k slightly helps to improve the constraints on the isocurvature contribution. Case 3 ($n_{\text{iso}} = 2.9$) is very different: as the data do not have any isocurvature but the isocurvature contribution in the theoretical model rapidly increases toward high k , we get only an upper bound for the isocurvature amplitude. Adding data up to higher k improves this upper bound significantly. Moreover, in Case 1 and Case 2, GC_{sp} gives tighter constraints compared to WL+GC_{ph}+XC, but for Case 3 GC_{sp} leads to more than one order of magnitude weaker constraints compared to WL+GC_{ph}+XC, which picks up the isocurvature contribution from high k .

For Case 1, our main result is that if the actual Universe had a CDI contribution that is of the order of the maximum 2σ allowed by *Planck* CMB data, then *Euclid* GC_{sp} would be able to detect a non-zero \mathcal{P}_{II2} at the 3σ level (1σ is 32.5% of the fiducial value according to Table 3). Combining all the *Euclid* data studied in this paper, GC_{sp}+WL+GC_{ph}+XC, and using the pessimistic setting, would lead to a 6.3σ detection of a non-zero isocurvature amplitude at $k_2 = 0.1 \text{ Mpc}^{-1}$ (1σ is 16.0% of the fiducial value according to Table 3). This 6.3σ detection is only mildly weakened (improved) to 5.6σ (6.8σ) if quasilinear (optimistic) settings are adopted. This great detection potential of *Euclid* is illustrated in Fig. 9, which also shows that for this model the constraints mainly come from GC_{sp} while the role of WL+GC_{ph}+XC is to confine the isocurvature spectral index close to the fiducial value without giving tight constraints on the overall amplitude, even (0,0) being inside the 68% CL region in the (\mathcal{P}_{II1} , \mathcal{P}_{II2}) plane with WL+GC_{ph}+XC.

Case 2 confirms our expectations that a primordial isocurvature amplitude of the same order as the adiabatic amplitude around k_2 is required in order for *Euclid* to be sensitive to it.

⁷ The values have been taken directly from the *Planck* 2018 MultiNest chains, except that all the power spectra amplitudes have been scaled up by a constant in order to obtain $\sigma_8 \approx 0.8111$. (When allowing for CDI, the CMB analysis typically gives $\sigma_8 \sim 0.75$, since the required amplitude for the CMB angular power spectra can be reached by a slightly smaller amplitude of $\mathcal{P}_{\mathcal{RR}}$ than in the pure adiabatic case due to the CDI power providing the rest at large scales. Then, at small scales, i.e. at high k , the matter perturbations originating from the isocurvature component are so much damped that the result is a relatively small σ_8 .) We do this scaling to be able to check the consistency against the other *Euclid* forecasts.

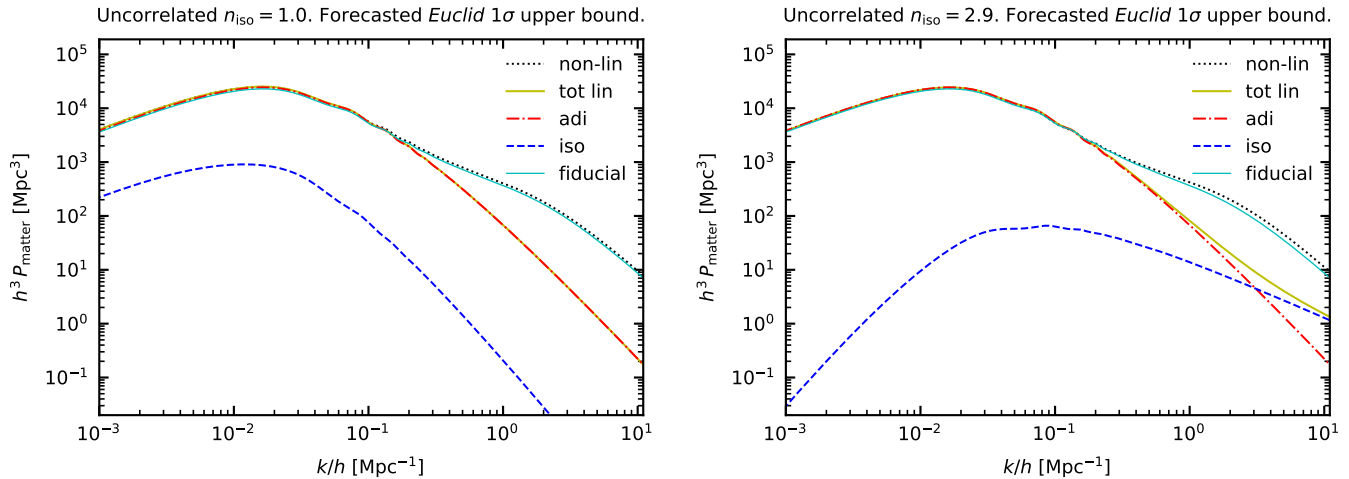


Fig. 7. Matter power spectra at redshift $z = 0$ for Case 2 (left panel) and Case 3 (right panel). The left panel shows the different contributions for our forecasted pessimistic GC_{sp} 1σ upper bound on our Case 2 uncorrelated isocurvature model with $n_{iso} = 1.0$ when the underlying true model (fiducial, cyan colour) is purely adiabatic. The upper bound on the isocurvature contribution is so small that the linear pure adiabatic (adi) and total linear (tot lin) matter power spectra are indistinguishable by eye in this figure. The right panel shows the same quantities for the forecasted GC_{sp} 1σ pessimistic upper bound on our Case 3 one-isocurvature-parameter uncorrelated isocurvature model with $n_{iso} = 2.9$ when the underlying true model (fiducial) is purely adiabatic. Note how, for Case 3, the isocurvature contribution visibly modifies the spectrum for $k/h \gtrsim 0.1 \text{ Mpc}^{-1}$.

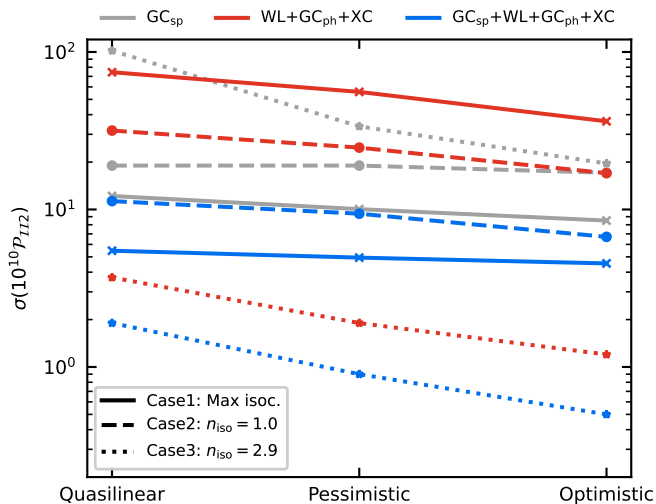


Fig. 8. Fisher-matrix marginalised uncertainty for 10^{10} times the primordial isocurvature perturbation amplitude \mathcal{P}_{II} at $k_2 = 0.1 \text{ Mpc}^{-1}$ for Case 1 “maximum 2σ allowed by *Planck*” (solid lines), Case 2 “scale-invariant uncorrelated $n_{iso} = 1.0$ ” (dashed lines), and Case 3 “blue-tilted uncorrelated $n_{iso} = 2.9$ ” (dotted lines). Our baseline results of Table 3 are for the pessimistic setting. To test the effect of the choice of k_{max} and ℓ_{max} on the results we repeat the analysis with an even more conservative quasilinear setting ($k_{max} = 0.15 h \text{ Mpc}^{-1}$ for GC_{sp} , $\ell_{max} = 750$ for WL, and $\ell_{max} = 500$ for GC_{ph} and XC) and with the optimistic setting ($k_{max} = 0.30 h \text{ Mpc}^{-1}$ for GC_{sp} , $\ell_{max} = 5000$ for WL, and $\ell_{max} = 3000$ for GC_{ph} and XC).

(Recall that the equal primordial amplitude means about 2% CDI contribution to the observable matter power spectrum at k_2 .) The left panel of Fig. 7 shows various contributions to the matter power spectrum in a model with the forecasted maximum (1σ , GC_{sp}) scale-invariant ($n_{iso} = 1.0$) CDI contribution. Naturally, in this case, *Euclid* does not improve the constraints over *Planck*.

In Case 3, our 2σ upper bound $\mathcal{P}_{II}(k_*)/\mathcal{P}_{RR}(k_*) < 0.86$ for the strongly blue-tilted uncorrelated CDI ($n_{iso} = 2.9$, pessimistic

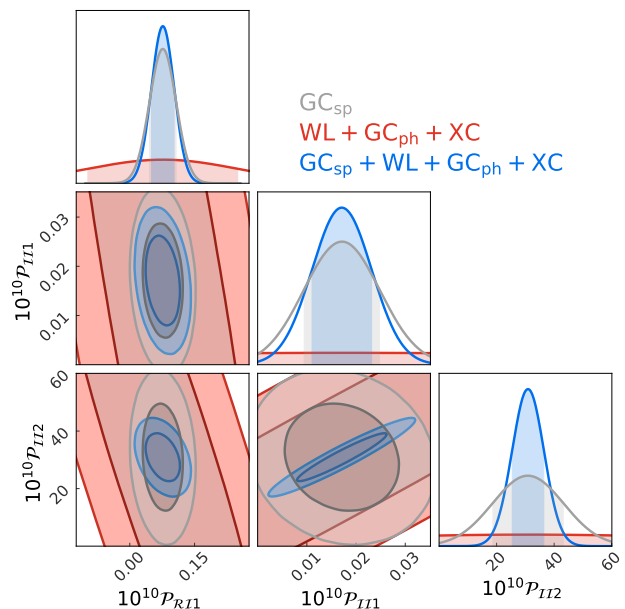


Fig. 9. *Euclid* marginalised posterior probability density functions for Case 1 “maximum 2σ allowed by *Planck*” isocurvature model using the pessimistic *Euclid* setting.

GC_{sp} , $k_{max} = 0.25 h \text{ Mpc}^{-1}$) fully matches the recent findings of Chung et al. (2023) who used galaxy correlation and bispectrum with a more rigorous non-linear model, but did not specify k_{max} . The forecasted *Euclid* GC_{sp} upper bound at $k_2 = 0.1 \text{ Mpc}^{-1}$ is 20% tighter than the *Planck* 2018 95% CL upper bound for the uncorrelated CDI with non-scale-invariant spectrum, “axion II” of Planck Collaboration: Akrami et al. (2020a).

We conclude that, in the case of a fiducial model with adiabatic initial conditions, *Euclid* GC_{sp} alone will constrain the blue-tilted CDI at medium and high k at the same level as *Planck* CMB observations. Adding WL+ GC_{ph} +XC can improve the containing power of *Euclid* by an order of magnitude (see the

second last column in Table 3 and the dotted lines in Fig. 8), should the modelling of non-linearities used here provide a suitable approximation of the photometric and weak lensing observables in the presence of blue-tilted CDI. This high gain from WL+GC_{ph}+XC merits a detailed future N-body study of blue-tilted CDI models.

6. Expected constraints on primordial non-Gaussianity

One of the most common predictions of inflation is the presence of a small amount of non-Gaussianity in the distribution of the seed perturbations, generated during the early stages of the Universe. In the simplest models, these primordial fluctuations are nearly perfectly Gaussian, while more complex scenarios predict a deviation from Gaussian distribution (see, e.g., Achúcarro et al. 2022, for a review). Measuring the amount of this primordial non-Gaussianity (PNG), parametrised in terms of a dimensionless amplitude parameter f_{NL} , has emerged as one of the most powerful probes of the early Universe (Bartolo et al. 2004; Meerburg et al. 2019).

Currently, the tightest constraints on f_{NL} come from the CMB anisotropies (Planck Collaboration: Akrami et al. 2020b), where the constraints on the so-called local-type PNG are $f_{\text{NL}}^{\text{loc}} = -0.9 \pm 5.1$ at the 68% CL. Most of the information on PNG within the CMB has been extracted. Next-generation LSS surveys, due to their inherently 3-dimensional structure and large cosmic volumes, are catching up fast (Leistedt et al. 2014; Castorina et al. 2019; Mueller et al. 2022; D’Amico et al. 2022; Cabass et al. 2022; Rezaie et al. 2024; Cagliari et al. 2024) and could soon supersede the CMB measurements (e.g. Karagiannis et al. 2018, 2020).

In this section, we present forecasted uncertainties on the amplitude parameter of three PNG shapes by utilising the spectroscopic galaxy clustering *Euclid* sample (GC_{sp}). Our main results follow from the Fisher-matrix methodology described in EC20. Additionally, we summarise, for comparison, the findings on the amplitude of local PNG presented in *Euclid Collaboration: Andrews et al. (2024)*, which are based on an advanced field-level inference technique. The constraints on f_{NL} presented in this section follow the CMB convention as in *Planck Collaboration: Akrami et al. (2020b)*.

6.1. Fisher analysis

6.1.1. Matter bispectrum

In most inflationary scenarios, the generated amount of PNG leads to a non-zero bispectrum⁸ of the primordial curvature fluctuation field. The resulting bispectrum is characterised by an amplitude parameter f_{NL} , which defines the magnitude of the PNG signal, and by the shape, which describes the functional dependence on the various Fourier space triangles. Both of them depend strongly on the inflationary model at hand. Thus, constraining the amplitude of the primordial bispectrum can rule out different classes of inflationary models and shed light on the early phases of the Universe.

Violating different conditions of the standard inflation generates a non-zero primordial bispectrum, whose signal peaks at

⁸ The presence of PNG leads to all high-order correlation functions of the primordial perturbations being non-zero. However, in most inflationary models, the three-point function and its Fourier transformation, the bispectrum, are the largest.

distinct triangle configurations. In this section, we consider the most studied PNG shapes:

- *local* (Salopek & Bond 1990; Gangui et al. 1994; Verde et al. 2000; Komatsu & Spergel 2001), peaking at squeezed triangles ($k_3 \ll k_2 \simeq k_1$);
- *equilateral* (Creminelli et al. 2006), peaking at equilateral configurations ($k_3 \simeq k_2 \simeq k_1$);
- *orthogonal* (Senatore et al. 2010), peaking at both equilateral and folded triangles ($k_1 \simeq k_2 \simeq k_3/2$). Here we consider both approximations of the exact shape derived in Senatore et al. (2010): *orthogonal-CMB*, more used in CMB analysis because of its 2-dimensional projection accuracy, and *orthogonal-LSS*, which is important for LSS studies.

The corresponding bispectra of the Bardeen gauge-invariant primordial gravitational potential Φ are defined respectively as

$$B_{\Phi}^{\text{loc}}(k_1, k_2, k_3) = 2f_{\text{NL}}^{\text{loc}} \left[P_{\Phi}(k_1)P_{\Phi}(k_2) + 2 \text{ perms} \right], \quad (25)$$

$$B_{\Phi}^{\text{equil}}(k_1, k_2, k_3) = 6f_{\text{NL}}^{\text{equil}} \left(- \left[P_{\Phi}(k_1)P_{\Phi}(k_2) + 2 \text{ perms} \right] - 2 \left[P_{\Phi}(k_1)P_{\Phi}(k_2)P_{\Phi}(k_3) \right]^{2/3} + \left[P_{\Phi}^{1/3}(k_1)P_{\Phi}^{2/3}(k_2)P_{\Phi}(k_3) + 5 \text{ perms} \right] \right), \quad (26)$$

$$B_{\Phi}^{\text{ortho-CMB}}(k_1, k_2, k_3) = 6f_{\text{NL}}^{\text{ortho-CMB}} \left(- 3 \left[P_{\Phi}(k_1)P_{\Phi}(k_2) + 2 \text{ perms} \right] + 3 \left[P_{\Phi}^{1/3}(k_1)P_{\Phi}^{2/3}(k_2)P_{\Phi}(k_3) + 5 \text{ perms} \right] - 8 \left[P_{\Phi}(k_1)P_{\Phi}(k_2)P_{\Phi}(k_3) \right]^{2/3} \right), \quad (27)$$

$$B_{\Phi}^{\text{ortho-LSS}}(k_1, k_2, k_3) = 6f_{\text{NL}}^{\text{ortho-LSS}} \left[P_{\Phi}(k_1)P_{\Phi}(k_2)P_{\Phi}(k_3) \right]^{2/3} \left((1+p) \frac{\Delta}{k_1 k_2 k_3} - p \frac{\Gamma^3}{k_1^2 k_2^2 k_3^2} \right), \quad (28)$$

where

$$p = \frac{27}{-21 + \frac{743}{7(20\pi^2 - 193)}}, \quad \Delta = (k_T - 2k_1)(k_T - 2k_2)(k_T - 2k_3)$$

$$\Gamma = \frac{2}{3}(k_1 k_2 + k_2 k_3 + k_3 k_1) - \frac{1}{3}(k_1^2 + k_2^2 + k_3^2), \quad (29)$$

and $k_T = k_1 + k_2 + k_3$. The power spectrum $P_{\Phi}(k)$ is directly related to the power spectrum of the primordial curvature perturbations generated during inflation. The primordial potential perturbations Φ are associated with the linear dark matter field via the Poisson equation $\delta_{\text{m}}^{\text{L}}(\mathbf{k}, z) = M(k, z)\Phi(\mathbf{k})$, where $M(k, z) = 2c^2 D(z) T(k) k^2 / (3\Omega_{\text{m}} H_0^2)$, with $D(z)$ the linear growth factor and $T(k)$ the matter transfer function normalised to unity at large scales $k \rightarrow 0$. Thus, $P_{\Phi}(k) = P_{\text{m}}(k, z) / M^2(k, z)$. The leading order PNG contribution to the matter density bispectrum is

$$B_I(k_1, k_2, k_3; z) = M(k_1, z)M(k_2, z)M(k_3, z)B_{\Phi}(k_1, k_2, k_3). \quad (30)$$

Due to the non-linear nature of gravity the bispectrum has additional terms at leading order besides the primordial contribution shown above – for LSS it is an intrinsically non-zero quantity, independently of the initial conditions.

6.1.2. Galaxy power spectrum and bispectrum

In a biased tracer of the dark matter field, like the GC_{sp} *Euclid* sample considered here, there are two main sources of PNG signal: the primordial part of the galaxy bispectrum (Eq. 30) and the scale-dependent bias signature (Dalal et al. 2008; Slosar et al. 2008; Matarrese & Verde 2008; Verde & Matarrese 2009; Afshordi & Tolley 2008; Desjacques & Seljak 2010) induced at linear order in the galaxy power spectrum and bispectrum. Therefore, we use both summary statistics in order to extract the PNG information within the GC_{sp} sample. In redshift space, the tree-level model for the observed galaxy power spectrum and bispectrum, in the presence of PNG, is given by

$$P_{\text{obs}}(\mathbf{k}^{\text{ref}}; z) = \frac{1}{q_{\perp}^2(z) q_{\parallel}(z)} \left[D^{\text{P}}(\mathbf{k}; z) Z_1(\mathbf{k})^2 P_{\text{m}}^{\text{L}}(k; z) + P_{\text{s}}(z) \right], \quad (31)$$

$$B_{\text{obs}}(\mathbf{k}_1^{\text{ref}}, \mathbf{k}_2^{\text{ref}}, \mathbf{k}_3^{\text{ref}}; z) = \frac{1}{q_{\perp}^4(z) q_{\parallel}^2(z)} \left[D^{\text{B}}(\mathbf{k}_1, \mathbf{k}_2, \mathbf{k}_3; z) \left[Z_1(\mathbf{k}_1) Z_1(\mathbf{k}_2) Z_1(\mathbf{k}_3) B_I(k_1, k_2, k_3; z) + (2Z_1(\mathbf{k}_1) Z_1(\mathbf{k}_2) Z_2(\mathbf{k}_1, \mathbf{k}_2) P_{\text{m}}^{\text{L}}(k_1; z) P_{\text{m}}^{\text{L}}(k_2; z) + 2 \text{perm}) \right] + 2P_{\varepsilon\varepsilon\delta}(z) (Z_1(\mathbf{k}_1) P_{\text{m}}^{\text{L}}(k_1; z) + 2 \text{perm}) + B_{\varepsilon}(z) \right], \quad (32)$$

where the redshift dependence of the kernels has been depreciated for simplicity. The redshift kernels up to second order for a general type of PNG are

$$\begin{aligned} Z_1(\mathbf{k}_i, z) &= b_1(z) + f_{\text{g}}(z) \mu_i^2 + f_{\text{NL}} b_{\Psi}(z) \frac{k_i^{\alpha}}{M(k_i, z)}, \quad (33) \\ Z_2(\mathbf{k}_i, \mathbf{k}_j, z) &= b_1(z) F_2(\mathbf{k}_i, \mathbf{k}_j) + f_{\text{g}}(z) \mu_{ij}^2 G_2(\mathbf{k}_i, \mathbf{k}_j) + \frac{b_2(z)}{2} \\ &+ \frac{b_{s^2}(z)}{2} S_2(\mathbf{k}_i, \mathbf{k}_j) + \frac{f_{\text{g}}(z) \mu_{ij} k_{ij}}{2} \left[\frac{\mu_i}{k_i} Z_1(\mathbf{k}_j, z) + \frac{\mu_j}{k_j} Z_1(\mathbf{k}_i, z) \right] \\ &+ f_{\text{NL}} b_{\Psi}(z) \frac{1}{2} \left[\frac{k_i^{\alpha}}{k_j^2 M(k_i)} + \frac{k_j^{\alpha}}{k_i^2 M(k_j)} \right] \mathbf{k}_i \cdot \mathbf{k}_j \\ &+ f_{\text{NL}} b_{\Psi\delta}(z) \frac{1}{2} \left[\frac{k_i^{\alpha}}{M(k_i)} + \frac{k_j^{\alpha}}{M(k_j)} \right], \quad (34) \end{aligned}$$

where $\mu_i = \hat{\mathbf{k}}_i \cdot \hat{\mathbf{z}}$ with $\hat{\mathbf{z}}$ the line-of-sight vector, $\mu_{ij} = (\mu_i k_i + \mu_j k_j) / k_{ij}$, and $k_{ij}^2 = (\mathbf{k}_i + \mathbf{k}_j)^2$. The kernels $F_2(\mathbf{k}_i, \mathbf{k}_j)$ and $G_2(\mathbf{k}_i, \mathbf{k}_j)$ are the second-order symmetric standard perturbation theory kernels (Bernardeau et al. 2002), while $S_2(\mathbf{k}_1, \mathbf{k}_2) = (\mathbf{k}_1 \cdot \mathbf{k}_2)^2 - 1/3$ is the tidal kernel (McDonald & Roy 2009). In addition to the triangle shape, defined by the three sides k_1, k_2, k_3 , the redshift space bispectrum has a dependence on the orientation of the triangle with respect to the line-of-sight direction. Two angles characterise this orientation, which are chosen to be the polar angle θ of \mathbf{k}_1 [$\cos(\theta) = \mu_1$] and the azimuthal angle ϕ around \mathbf{k}_1 , which is involved in the definition of μ_2 (Scoccimarro et al. 1999).

The factors $D^{\text{P}}(\mathbf{k}, z)$ and $D^{\text{B}}(\mathbf{k}_1, \mathbf{k}_2, \mathbf{k}_3, z)$ incorporate the redshift errors and FoG effect (see Sect. 2.1) for the power spectrum and bispectrum, respectively, while they are given by $D^{\text{P}}(\mathbf{k}, z) = \exp\{-k \mu [f_{\text{g}}^2(z) \sigma_{\text{p}}^2(z) + \sigma_{\text{r}}^2(z)]\}$ and $D^{\text{B}}(\mathbf{k}_1, \mathbf{k}_2, \mathbf{k}_3, z) = \exp\{-(k_1^2 \mu_1^2 + k_2^2 \mu_2^2 + k_3^2 \mu_3^2) [f_{\text{g}}^2(z) \sigma_{\text{p}}^2(z) + \sigma_{\text{r}}^2(z)]/2\}$. The fiducial values of the stochastic terms in Eqs. (31) and (32) are taken to

be those predicted by Poisson statistics (Desjacques et al. 2018), i.e. $P_{\text{s}} = 1/\bar{n}_{\text{g}}$, $P_{\varepsilon\varepsilon\delta} = b_1/(2\bar{n}_{\text{g}})$, and $B_{\varepsilon} = 1/\bar{n}_{\text{g}}^2$.

The fiducial values of the linear and quadratic galaxy bias coefficients, needed in Eqs. (33) and (34), are derived by using the peak-background split argument applied on the best-fit halo mass function of Tinker et al. (2010), together with the halo occupation distribution (HOD) model of Yankelevich & Porciani (2019). Moreover, the second-order tidal field bias term, following the convention of (Baldauf et al. 2012), is given by $b_{s^2}(z) = -4[b_1(z) - 1]/7$. In the presence of PNG, the peak-background split argument is used to derive the non-Gaussian halo bias coefficients for the shapes considered here (Schmidt & Kamionkowski 2010; Giannantonio & Porciani 2010; Scoccimarro et al. 2012; Desjacques et al. 2011a; Schmidt et al. 2013; Desjacques et al. 2011b; Schmidt et al. 2013; Desjacques et al. 2018):

$$b_{\Psi}(M, z) = A \left[b_{\Phi} + 4 \left(\frac{d \ln \sigma_{R, -\alpha}^2}{d \ln \sigma_R^2} - 1 \right) \right] \frac{\sigma_{R, -\alpha}^2}{\sigma_R^2} \quad (35)$$

and

$$\begin{aligned} b_{\Psi\delta}(M, z) &= A \left[\delta_c \left(b_2 - \frac{8}{21} (b_1 - 1) \right) \right. \\ &\left. + (b_1 - 1) \left(2 \frac{d \ln \sigma_{R, -\alpha}^2}{d \ln \sigma_R^2} - 3 \right) \right] \frac{\sigma_{R, -\alpha}^2}{\sigma_R^2} + b_{\Psi}, \quad (36) \end{aligned}$$

where $\delta_c = 1.686$, $\sigma_{R, n}^2 = (2\pi)^{-3} \int d^3 \mathbf{k} k^n W_R(k)^2 P_{\text{m}}^{\text{L}}(k; z)$, with W_R being the top-hat filter. For local PNG, $\alpha = 0$ and $A = 1$, the above expressions reduce to $b_{\Psi} \equiv b_{\Phi}$ and $b_{\Psi\delta} \rightarrow b_{\Phi\delta} = \delta_c [b_2 - 8/21 (b_1 - 1)] - b_1 + 1 + b_{\Phi}$ (Desjacques et al. 2018; Barreira 2022b; Cabass et al. 2022). Moreover, for equilateral and orthogonal-CMB PNG they are $\alpha = 2, A = 3$, and $\alpha = 1, A = -3$, respectively (Schmidt & Kamionkowski 2010; Giannantonio et al. 2012). The distinct squeezed-limit behaviour of the orthogonal-LSS template, compared to orthogonal-CMB, has important implications for the scale dependence of PNG bias terms. Like the equilateral case, this template does not lead to a scale-dependent bias correction (i.e. $\alpha = 2$) (Schmidt & Kamionkowski 2010). These results are used together with the HOD model to derive the fiducial values for the PNG galaxy bias coefficients at redshift z_i .

The exact expression for b_{Φ} is still unresolved and under investigation within the community (see, e.g., Barreira 2022a, for a discussion). The conventional derivation relies on the universality relation of the halo mass function, i.e. b_{Φ} depends only on the halo mass and redshift. Recent work has shown that it depends on the halo formation history (Barreira et al. 2020; Barreira 2022b; Lazeyras et al. 2023; Fondi et al. 2024), i.e. on properties beyond total mass. Here, we adopt the modified universality relation $b_{\Phi} = 2\delta_c(b_1 - p)$ with a fixed $p = 0.55$ (Barreira 2020, 2022a; Cabass et al. 2022).

Note that in the case of equilateral and orthogonal-LSS PNG templates ($\alpha = 2$), the last term in Eq. (35) and the last two terms in Eq. (36) become scale-independent on large scales (i.e. $b_{\Psi} \propto 1$). This indicates that these terms do not have constraining power on equilateral and orthogonal-LSS PNG (see, e.g., Schmidt & Kamionkowski 2010; Scoccimarro et al. 2012; Schmid & Hui 2013; Assassi et al. 2015, for a discussion). Hence, we exclude these terms from the linear and quadratic redshift kernels. This means that the sole contribution in the equilateral and orthogonal-LSS PNG forecasts is the primordial bispectrum (i.e. B_I in Eq. 32).

Table 4. Forecasted 1σ uncertainties on the three PNG shapes from the GC_{sp} sample of *Euclid* from the power spectrum, bispectrum, and their joint signal. Inside the parenthesis we present the forecasts assuming the PNG bias coefficients to be free in the presence of priors (see Sect. 6.1.3 for a discussion). All the results consider *Planck* priors for the cosmological parameters.

	P	B	P+B
Pessimistic quasilinear setting $\text{GC}_{\text{sp}} (k_{\text{max}} = 0.15 h \text{ Mpc}^{-1})$			
$f_{\text{NL}}^{\text{loc}}$	2.8 (-)	3.3 (12.7)	2.2 (12.5)
$f_{\text{NL}}^{\text{equil}}$	-	126 (126)	108 (108)
$f_{\text{NL}}^{\text{ortho-CMB}}$	214 (-)	38 (40)	33 (34)
$f_{\text{NL}}^{\text{ortho-LSS}}$	-	37 (37)	33 (33)
Pessimistic setting $\text{GC}_{\text{sp}} (k_{\text{max}} = 0.25 h \text{ Mpc}^{-1})$			
$f_{\text{NL}}^{\text{loc}}$	2.7 (-)	2.1 (9.1)	1.7 (8.7)
$f_{\text{NL}}^{\text{equil}}$	-	74 (74)	63 (63)
$f_{\text{NL}}^{\text{ortho-CMB}}$	177 (-)	30 (31)	24 (25)
$f_{\text{NL}}^{\text{ortho-LSS}}$	-	23 (23)	21 (21)
Optimistic setting $\text{GC}_{\text{sp}} (k_{\text{max}} = 0.3 h \text{ Mpc}^{-1})$			
$f_{\text{NL}}^{\text{loc}}$	2.7 (-)	1.9 (8.5)	1.6 (8.1)
$f_{\text{NL}}^{\text{equil}}$	-	64 (64)	53 (53)
$f_{\text{NL}}^{\text{ortho-CMB}}$	130 (-)	27 (29)	22 (24)
$f_{\text{NL}}^{\text{ortho-LSS}}$	-	20 (20)	19 (19)

6.1.3. Fisher forecasts

The Fisher matrix for the bispectrum in one redshift bin z_i is

$$F_{\alpha\beta}^B(z_i) = \frac{1}{4\pi} \sum_T \int_{-1}^1 d\mu_1 \int_0^{2\pi} d\phi \frac{\partial B_{\text{obs}}(\mathbf{k}_1, \mathbf{k}_2, \mathbf{k}_3, z_i)}{\partial p_\alpha} [\text{Cov}^G]^{-1} \times \frac{\partial B_{\text{obs}}(\mathbf{k}_1, \mathbf{k}_2, \mathbf{k}_3, z_i)}{\partial p_\beta}, \quad (37)$$

where \sum_T indicates the sum over all triangles formed by the Fourier modes k_1 , k_2 and k_3 . Here we only consider the Gaussian part of the bispectrum covariance matrix. In the thin shell limit ($k \gg \Delta k$), it is given by

$$\text{Cov}_{ij}^G = \frac{(2\pi)^6}{V_s V_{123}} s_{123} \delta_{ij} P_{\text{obs}}(\mathbf{k}_1) P_{\text{obs}}(\mathbf{k}_2) P_{\text{obs}}(\mathbf{k}_3), \quad (38)$$

where $s_{123} = 6, 2, 1$ for equilateral, isosceles, and scalene triangles, respectively. In this limit, the volume of the fundamental triangle bins is $V_{123} = 8\pi^2 k_1 k_2 k_3 \Delta k^3$ (Sefusatti et al. 2006), where the bin size Δk is taken to be the fundamental frequency of the survey, i.e. $\Delta k = k_f = 2\pi/V_s^{1/3}$. The expression for V_{123} requires some corrections for the extreme cases of flattened ($k_1 = k_2 + k_3$) and open ($k_1 \neq k_2 + k_3$) triangles, which are presented in Biagetti et al. (2022) and considered here as well.

The Gaussian covariance is assumed to be accurate enough up to linear and mildly non-linear scales, for high-density samples (Howlett & Percival 2017; Barreira & Schmidt 2017; Li

et al. 2019; Blot et al. 2019; Chan & Blot 2017). However, higher-order corrections to the bispectrum variance still have an effect even at the mildly non-linear scales at low redshifts. Hence, we consider these corrections in the bispectrum Fisher analysis by following the prescription of Chan & Blot (2017).

The stochastic contributions, the amplitude of the FoG effect, and the bias coefficients are treated as nuisance parameters and are marginalised over in the analysis. We use the Fisher analysis to generate power spectrum and bispectrum forecasts on the parameters of interest for ΛCDM with non-Gaussian initial conditions,

$$\Theta_{\text{final}} = \{\Omega_m, \Omega_b, h, n_s, \sigma_8, f_{\text{NL}}\}. \quad (39)$$

The forecasted 1σ uncertainties on the PNG amplitude of the three types considered here, coming from the GC_{sp} sample, are presented in Table 4. The forecasts from the galaxy power spectrum, bispectrum, and their combined signal are shown, where the latter is derived by summing the Fisher matrices of the first two without considering their cross-covariance, since it would have a minimal impact on our results (Chan & Blot 2017; Yankelevich & Porciani 2019). These findings highlight the potential of the *Euclid* mission to tightly constrain the primordial Universe.

The forecasts are presented for different small-scale cutoffs (i.e. k_{max}), with an increasing value, venturing further into the non-linear regime. In the case of local PNG, the power spectrum dominates over the bispectrum as the main source of signal for the small k_{max} value, while the reverse is observed as we allow smaller scales to enter the analysis. For the equilateral and orthogonal PNG types, bispectrum drives the forecasts for all the settings considered. This indicates the importance of the bispectrum in the analysis of the GC_{sp} sample in order to achieve tight constraints on the PNG amplitude.

In addition to the main forecasts presented in Table 4, for which the PNG bias coefficients (i.e. b_Ψ and $b_\Psi\delta$) are considered known, we present the results when these parameters are marginalised over (values inside the parenthesis). Following recent developments in the literature in effectively constraining the PNG bias coefficients (Fondi et al. 2024), we use Gaussian priors for b_Ψ and $b_\Psi\delta$ centred around their fiducial values (see the previous section for a discussion) with a 40% relative standard deviation (following Euclid Collaboration: Andrews et al. 2024). Note that in this case the power spectrum only provides constraints on the $f_{\text{NL}} b_\Psi$ product. The impact of marginalising over the PNG bias parameters, given the chosen priors, is significant for forecasts on local PNG, whereas it remains minimal for the other two types.

6.2. Bayesian analysis (BORG)

In this section, we highlight the results of Euclid Collaboration: Andrews et al. (2024) regarding the inference of local primordial non-Gaussianity using the Bayesian origin reconstruction from galaxies (BORG) algorithm (Jasche & Wandelt 2013; Jasche et al. 2015; Lavaux & Jasche 2016; Jasche & Lavaux 2019; Lavaux et al. 2019).

The BORG algorithm is a Bayesian hierarchical field-level inference framework for analysing cosmic structure in cosmological surveys (Jasche & Wandelt 2013; Jasche et al. 2015; Lavaux & Jasche 2016; Jasche & Lavaux 2019; Lavaux et al. 2019). It employs physical forward modeling of 3-dimensional galaxy fields to link the observed data to the 3-dimensional primordial matter fluctuation field. The algorithm proposes a set of initial

conditions ϵ , simulates the gravitational evolution of the matter field, and populates the evolved density field through a galaxy bias model (Assassi et al. 2015; Desjacques et al. 2018; Barreira 2020). This process generates model predictions compared to observed galaxy redshift data and includes the primordial perturbation with $f_{\text{NL}}^{\text{loc}}$ and scale-dependent biases under the assumption of the universal mass approximation (Barreira 2022c; Lucie-Smith et al. 2023; Fondi et al. 2024; Gutiérrez Adame et al. 2024). The target posterior distribution explored, which is generated by the data model, is formally expressed as

$$\mathcal{P}_{\text{post}}(\epsilon, f_{\text{NL}}, \{b_i^g\} | N_g^o) \propto \mathcal{P}_f(f_{\text{NL}}) \mathcal{P}_\epsilon(\epsilon) \mathcal{P}_b\{b_i^g\} \mathcal{P}_{\text{like}}(N_g^o | \epsilon, f_{\text{NL}}, \{b_i^g\}), \quad (40)$$

where N_g^o is the observed galaxy count data, $\mathcal{P}_\epsilon(\epsilon)$ is the Gaussian white-noise prior with zero mean and unit standard variance, $\mathcal{P}_{\text{like}}(N_g^o | \epsilon, f_{\text{NL}}, \{b_i^g\})$ is a likelihood distribution, and $\{b_i\}$ are the bias parameters (Euclid Collaboration: Andrews et al. 2024). Using Hamiltonian Monte Carlo and slice sampling, BORG explores the joint posterior of data, and thus infers the primordial initial conditions, the f_{NL} parameter, and marginalises over nuisance parameters (Jasche & Wandelt 2013; Andrews et al. 2023). This approach consistently accounts for observational and survey systematic effects and the incorporation of multiple PNG probes into the analysis (Jasche & Wandelt 2013; Andrews et al. 2023).

For mock data generation based on *Euclid* forecast specifications, the forward model is applied to a white-noise field and incorporates structure formation effects, redshift selection functions, sky masks, and other realistic observational aspects. The Markov chain starts at a random point for the initial conditions and converges with the target posterior distribution during the burn-in phase. Then, BORG, operating at resolutions down to $62.5 h^{-1} \text{Mpc}$, infers the initial conditions and $f_{\text{NL}}^{\text{loc}}$ that align closely with the expected confidence intervals of fiducial mock data. We analyse multiple mock data sets, each addressing various factors, such as different resolutions, different ground truth $f_{\text{NL}}^{\text{loc}}$ values, and sampling of additional bias parameters. The overall scope of runs contributes to a comprehensive understanding of inference processes.

We give an overview of the results in Table 5. The study demonstrates successful sampling of $f_{\text{NL}}^{\text{loc}}$ using *Euclid* data, achieving 1σ constraints across all runs. Notably, at a $62.5 h^{-1} \text{Mpc}$ resolution, we attain a constraining power of $\sigma(f_{\text{NL}}^{\text{ocal}}) = 2.3$, showcasing the method's ability to be competitive with other methods. These findings include handling *Euclid*-like specifications in the analysis framework, high-precision f_{NL} inference at multiple resolutions, and the impact of different parameter settings on the constraints. These results demonstrate the opportunity to use field-level inference as a complementary and independent approach to constrain the parameter space of plausible models for the early Universe.

In Fig. 10, we provide the main results of this section, a forecast of the achievable constraints for the *Euclid*-like mock with the method. Moreover, complementary to the main BORG results, we show the forecasted constraints from the Fisher matrix approach, presented in the previous section. These results correspond to the summed power spectrum and bispectrum signal after fixing the cosmology and marginalising over the nuisance parameters, as well as keeping a fixed $k_{\text{max}} = 0.1 h \text{Mpc}^{-1}$ over all redshifts, in order to match the specifications of the main BORG results. The 1σ forecasted errors on $f_{\text{NL}}^{\text{loc}}$ generated by the two methods are in good agreement.

Table 5. A table displaying $f_{\text{NL}}^{\text{loc}}$ inferences for each run in the BORG analysis, highlighting how changes in the data model affect constraints on $f_{\text{NL}}^{\text{loc}}$ for the given mock data. The last column provides a brief description of the analysis, with examples including resolution study or a change in the bias parameters. All $f_{\text{NL}}^{\text{loc}}$ estimates fall within 1σ of fiducial values, indicating consistent and reliable inference. Runs #1–#6 assume the universal mass function while Run #7 samples scale-dependent bias parameters. k_{max} values are in $h \text{Mpc}^{-1}$.

Run #	$f_{\text{NL}}^{\text{fid}}$	$\langle f_{\text{NL}} \rangle$	$\sigma_{f_{\text{NL}}}$	k_{max}^*	Description
1	0	-2.8	6.0	0.025	Low resolution
2	0	2.6	4.0	0.05	Mid resolution
3	0	-1.3	2.3	0.1	High resolution
4	5	6.0	2.5	0.1	Non-zero fiducial $f_{\text{NL}}^{\text{loc}}$
5	0	1.7	2.6	0.05	Fixed bias
6	0	0.9	6.3	0.05	$p = 1$
7	0	0.4	5.0	0.05	Sampling of $b_\phi, b_{\phi,\delta}$

* in units of $h \text{Mpc}^{-1}$

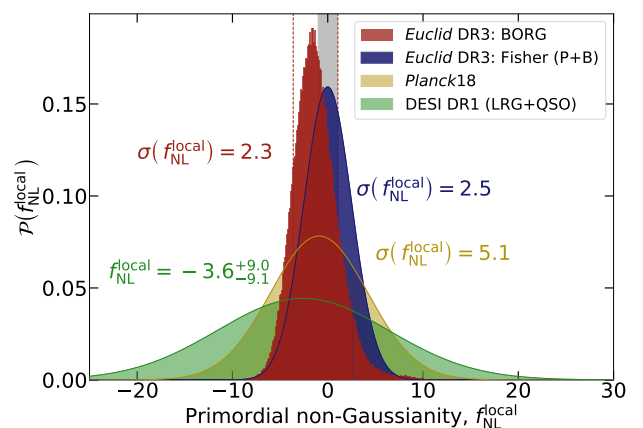


Fig. 10. Forecasted constraints on $f_{\text{NL}}^{\text{loc}}$ in *Euclid*-like data for the Fisher matrix formalism (Sect. 6.1) and the BORG method (Sect. 6.2). These results correspond to a fixed $k_{\text{max}} = 0.1 h \text{Mpc}^{-1}$ (i.e. Run # 3 of the BORG method). For comparison, we also include the current state-of-the-art constraints on $f_{\text{NL}}^{\text{loc}}$ from *Planck* (Planck Collaboration: Akrami et al. 2020b).

7. Beyond slow roll: searches for primordial features

In this section, we summarise the findings of the analysis and forecasts performed in Euclid Collaboration: Ballardini et al. (2024). The search for primordial features in the primordial power spectrum and bispectrum will benefit greatly from future LSS measurements expected from *Euclid* (Wang et al. 1999; Zhan et al. 2006; Huang et al. 2012; Chen et al. 2016a,b; Ballardini et al. 2016; Xu et al. 2016; Ansari Fard & Baghran 2018; Palma et al. 2018; Ballardini et al. 2018; Ballardini 2019; Beutler et al. 2019; Ballardini et al. 2020; Debono et al. 2020; Li et al. 2022; Ballardini & Finelli 2022; Ballardini et al. 2023; Mergulhão et al. 2023; Euclid Collaboration: Ballardini et al. 2024).

In general, and depending on their origin, features in the primordial power spectrum of density perturbations are the sign of conditions and dynamics at the very early Universe connected to new physical scales (see Achúcarro et al. 2022, for details and references). Modifications to the slow-roll dynamics such as an abrupt change in the background functions ϵ_1 (Starobinsky 1992; Adams et al. 2001) and c_s (Achúcarro et al. 2011; Chen 2011) at a particular moment during inflation, the periodicity in the background functions (Chen et al. 2008; Flauger et al. 2010;

Flauger & Pajer 2011; Chen 2010), and deviations from the standard Bunch-Davies vacuum of perturbations, (as well as combination of them) all result in oscillatory primordial features.

Following the Fisher-matrix-based methodology described in EC20 and here, we calculate the forecasted uncertainties from *Euclid*'s primary probes, i.e. spectroscopic galaxy clustering and the combination of photometric galaxy clustering and photometric weak lensing, for parametrised primordial features in the primordial power spectrum of density perturbations. We study two models characterised by a correction to the primordial power spectrum and to the matter power spectrum, $1 + \mathcal{A}_X \sin(\omega_X \Xi_X + 2\pi\phi_X)$, where \mathcal{A}_X is the amplitude of the primordial feature, ω_X is the dimensionless frequency, and ϕ_X is the normalised phase. In these models, we have a superimposed undamped oscillatory signal with $\Xi_{\text{lin}} \equiv k/k_*$ for linearly spaced oscillations (LIN) and with $\Xi_{\text{log}} \equiv \ln(k/k_*)$ for logarithmic ones (LOG).

In addition to the *Euclid*'s primary probes, we consider further information available from *Euclid* measurements including a numerical reconstruction of non-linear spectroscopic galaxy clustering (Beutler et al. 2019; Li et al. 2022, PS rec), the galaxy clustering bispectrum (Karagiannis et al. 2018),⁹ and the expected additional information (without including the cross-correlation) from CMB experiments (Euclid Collaboration: Ilić et al. 2022) such as *Planck* (Planck Collaboration: Aghanim et al. 2020b), SO (Ade et al. 2019), and CMB-S4 (CMB-S4 Collaboration: Abazajian et al. 2019).

We use perturbation theory (PT) predictions to model the galaxy clustering non-linear matter power spectrum (Blas et al. 2016; Vasudevan et al. 2019; Beutler et al. 2019; Chen et al. 2020; Ballardini & Barbieri 2024) plus a modified version of HMCODE (Mead et al. 2016) for the photometric probes. In order to assess the accuracy of the PT predictions at leading order and next-to-leading order, we generate a set of N-body simulations based on the COMoving Lagrangian Approximation (COLA) method (Tassev et al. 2013, 2015; Winther et al. 2017; Wright et al. 2017) with primordial oscillations injected to their initial conditions. We also use simulations produced in Ballardini et al. (2020) with the N-body code GADGET-3, a modified version of the publicly available code GADGET-2 (Springel et al. 2001; Springel 2005), to validate the COLA-based simulations and we use the N-body code ramSES (Teyssier 2002) to generate snapshots of dark matter to reconstruct the density fields as done in Li et al. (2022).

While the uncertainties on the primordial feature amplitude depend strongly on the value of the dimensionless frequency ω_X considering single *Euclid* probes, the combination of the spectroscopic and photometric probes (as well as the further addition of non-primary probes) allows us to reach robust uncertainties on the entire range of frequencies ($10^{0.2}$, $10^{2.1}$) we consider here. Our uncertainties, combining all the sources of information expected from *Euclid* in combination with future CMB experiments, e.g. SO complemented with *Planck* at low ℓ , correspond to $\mathcal{A}_{\text{lin}} = 0.0100 \pm 0.0008$ and $\mathcal{A}_{\text{log}} = 0.0100 \pm 0.0008$ for GC_{sp} (PS rec + BS)+WL+GC_{ph}+XC+SO-like for both the pessimistic and optimistic settings. In Table 6, we summarise the marginalised uncertainties of the primordial feature parameters, in percentage relative to the corresponding fiducial val-

⁹ We note that primordial features generated in single-field models are expected to show correlated signals between the primordial bispectrum and the primordial power spectrum (Chen et al. 2007, 2008; Gong et al. 2014; Mooij et al. 2015) and can be studied through a combined analysis (Fergusson et al. 2015; Meerburg et al. 2016; Planck Collaboration: Akrami et al. 2020a; Karagiannis et al. 2018).

Table 6. Fisher-matrix-based forecasted marginalised uncertainties for the feature model parameters, relative to their corresponding fiducial values ($\mathcal{A}_X = 0.01$, $\omega_X = 10$, $\phi_X = 0$), for the LIN and LOG models in the pessimistic and optimistic settings, using *Euclid*'s primary probes (GC_{sp}+WL+GC_{ph}+XC) alone and in combination with non-linear reconstruction of GC_{sp}, galaxy clustering bispectrum, and SO-like CMB.

	<i>Euclid</i>	GC _{sp} (rec) + WL + GC _{ph} + XC + BS + SO-like + <i>Planck</i> low- ℓ
Pessimistic setting		
A_{lin}	21%	8.5%
ω_{lin}	2.9%	0.83%
ϕ_{lin}	0.083	0.030
A_{log}	22%	7.3%
ω_{log}	2.4%	0.81%
ϕ_{log}	0.044	0.019
Optimistic setting		
A_{lin}	18%	8.1%
ω_{lin}	1.2%	0.84%
ϕ_{lin}	0.047	0.028
A_{log}	18%	6.6%
ω_{log}	1.1%	0.60%
ϕ_{log}	0.035	0.016

ues, for the full combination of *Euclid*'s primary probes, i.e. GC_{sp}+WL+GC_{ph}+XC, and in combination with the reconstruction of non-linear spectroscopic galaxy clustering, galaxy clustering bispectrum, and CMB information; see Fig. 11.

8. Conclusions

In this paper, we have presented highlights for the *Euclid* capability to test the cosmic initial conditions. In most of the cases, we have exploited the uniqueness of *Euclid*, i.e. the combination of the 3-dimensional galaxy clustering from the spectroscopic survey and the 3×2 pt from the photometric survey. This combination guarantees the removal of many degeneracies among the cosmological parameters that affect each probe separately and ensures constraints that are tighter than those from any other galaxy surveys in operation.

We have presented Fisher forecasts following EC20 for the spatial curvature, the running of the spectral index of the power spectrum of curvature perturbations, isocurvature perturbations, features in the primordial power spectrum from the main probes, and forecasts for primordial non-Gaussianity from the spectroscopic survey.

We have found that the combination of the *Euclid*'s main probes will provide the uncertainty of $\sigma(\Omega_K) = 0.0044$ (0.003) in the pessimistic (optimistic) setting assuming flat spatial sections as fiducial cosmology. These expected constraints can powerfully break the parameter degeneracy in what is achievable through the measurements of CMB temperature and polarisation anisotropies and return tighter limits such as $\sigma(\Omega_K) = 0.0009$ (0.0006) for the *Euclid*'s pessimistic (optimistic) setting in combination with the Simons Observatory.

For the fiducial value $\alpha_s = -0.01$, we have found that the combination of the *Euclid*'s main probes can reach the uncertainties $\sigma(n_s) \sim 0.008$ (0.0044) for the scalar spectral index and $\sigma(\alpha_s) \sim 0.005$ (0.002) for its running in the pessimistic (optimistic) setting. We have also found the uncertainty of

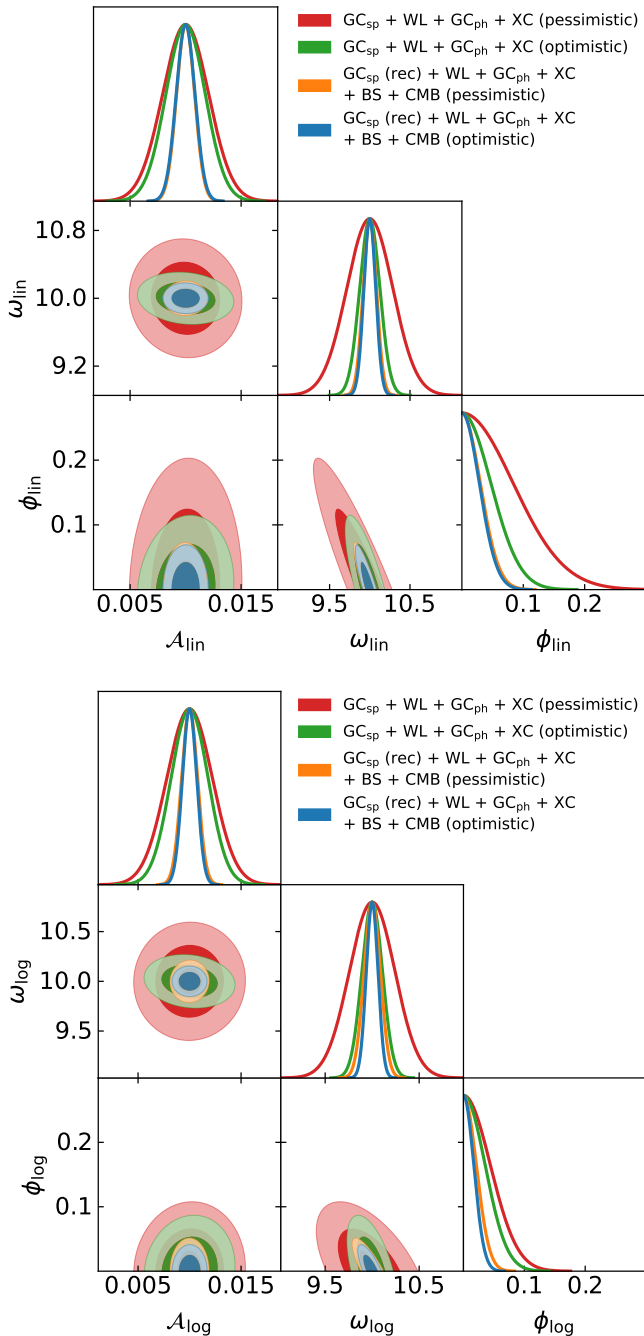


Fig. 11. Fisher-forecast marginalised two-dimensional contours and one-dimensional probability distribution functions from *Euclid* on the primordial feature parameters for the LIN model with $\omega_{\text{lin}} = 10$ (top panel) and the LOG model with $\omega_{\text{log}} = 10$ (bottom panel); in both cases we have $\mathcal{A}_X = 0.01$ and $\phi_X = 0$. We show $\text{GC}_{\text{sp}} + \text{WL} + \text{GC}_{\text{ph}} + \text{XC}$ with the pessimistic (optimistic) setting in red (green) and $\text{GC}_{\text{sp}}(\text{rec}) + \text{WL} + \text{GC}_{\text{ph}} + \text{XC}$ in combination with *Euclid* GC_{sp} bispectrum and SO-like CMB measurements with the pessimistic (optimistic) setting in orange (blue).

$\sigma(\alpha_s) = 0.004$ (0.0015) for a smaller fiducial value $\alpha_s = -0.001$, with $\sigma(n_s) \sim 0.006$ (0.0036), always in the pessimistic (optimistic) setting. These uncertainties are comparable with current constraints from *Planck* (Planck Collaboration: Akrami et al. 2020a). In addition, we have shown how *Euclid*, in combination with future CMB experiments, will probe $\alpha_s \lesssim \mathcal{O}(10^{-3})$,

therefore nearing the running expected in the currently preferred simplest slow-roll inflationary models.

By leveraging the smaller scales that *Euclid* has access to compared to the CMB measurements, we have explored what can be achieved for testing the adiabaticity of the initial conditions. Even though *Euclid* cannot achieve the CMB sensitivity to nearly scale-invariant CDM isocurvature perturbations, it has the capability to provide constraints on isocurvature perturbations with a blue spectral index that are at least one order of magnitude better than the current ones based on *Planck*. In order to achieve these tight limits, the use of the 3×2 pt is essential, and therefore, more work is needed to model non-linear scales in the presence of isocurvature perturbations at k beyond the EFT treatment suitable for GC_{sp} adopted in Chung et al. (2023).

We have also forecasted the constraints on primordial non-Gaussianity from the spectroscopic survey. The combined power spectrum and bispectrum Fisher forecast leads to $\sigma(f_{\text{NL}}^{\text{local}}) = 2.2$, $\sigma(f_{\text{NL}}^{\text{equil}}) = 108$, and $\sigma(f_{\text{NL}}^{\text{ortho}}) = 33$ by assuming $k_{\text{max}} = 0.15 h \text{Mpc}^{-1}$ and universality for the halo mass function. We have shown how the expected uncertainty on the local shape can be improved up to 20% by encompassing summary statistics and using Bayesian field-level inference, following Andrews et al. (2023).

We have analysed *Euclid*'s sensitivity to features in the primordial power spectrum. For *Euclid*'s main probes, we have found the relative errors 21% (22%) in the pessimistic setting and 18% (18%) in the optimistic setting for the amplitude of the linear (logarithmic) superimposed oscillations, with a fiducial value of 0.01. These uncertainties can be further improved by adding the information from the bispectrum and the non-linear reconstruction.

There are at least two important aspects that we have not studied in this paper.

The first aspect is the inclusion of *Euclid*-CMB cross-correlation (Euclid Collaboration: Ilić et al. 2022) for the physics of the early Universe. There are certain parameters, such as primordial local non-Gaussianity, which can be constrained by the CMB cross-correlation – see, e.g., Bermejo-Climent et al. (2021).

The second aspect is the interplay between *Euclid*'s capability and the CMB B -mode polarisation in addition to the temperature and E -mode polarisation. The CMB B -mode polarisation is the imprint of inflationary gravitational waves, whose amplitude is proportional to the energy scale at which inflation occurred, and is one of the main targets of next-generation CMB experiments dedicated to polarisation measurement (Ade et al. 2019; CMB-S4 Collaboration: Abazajian et al. 2019; LiteBIRD Collaboration et al. 2023). The search for the B -mode polarization will lead either to a detection or to an upper bound on r , *Euclid*'s constraints on n_s and α_s will be highly complementary to the CMB measurements in constraining inflation.

To conclude, *Euclid*'s measurements will have profound implications for the physics of inflation. The precision in the determination of n_s will pin down not only the slope of the inflationary potential, but also the uncertainties in the reheating stage after inflation, which affect the theoretical predictions of any inflationary model. The expected sensitivity of $\sigma(\alpha_s) \sim \mathcal{O}(10^{-3})$ will take us unprecedentedly closer to a generic prediction of inflation, such as the small but non-zero running of the scalar tilt, down to the expected values predicted by the simplest slow-roll inflationary models. As discussed in the paper, *Euclid*'s GC_{sp} has the capability of measuring $\sigma(f_{\text{NL}}^{\text{local}})$ below the *Planck*'s constraint when assuming universality for the halo mass function.

Expected *Euclid*'s galaxy clustering measurements of the local, as well as the other types of, primordial non-Gaussianity will be able to shed light on inflation interactions and on the presence of massive fields during inflation, making the idea of testing inflation as a cosmological collider (Arkani-Hamed & Maldacena 2015) operational.

Acknowledgements. FF acknowledges partial financial support from the contract ASI/INAF for the *Euclid* mission n.2018-23-HH.0, INFN InDark initiative and from the COSMOS network (www.cosmosnet.it) through the ASI (Italian Space Agency) grants 2016-24-H.0 and 2016-24-H.1-2018, as well as 2020-9-HH.0 (participation in LiteBIRD phase A). YA acknowledges support by the Spanish Research Agency (Agencia Estatal de Investigación)'s grant RYC2020-030193-I/AEI/10.13039/501100011033, by the European Social Fund (Fondo Social Europeo) through the Ramón y Cajal program within the State Plan for Scientific and Technical Research and Innovation (Plan Estatal de Investigación Científica y Técnica y de Innovación) 2017-2020, by the Spanish Research Agency through the grant IFT Centro de Excelencia Severo Ochoa No CEX2020-001007-S funded by MCIN/AEI/10.13039/501100011033, and by the Spanish National Research Council (CSIC) through the Talent Attraction grant 20225AT025. DK acknowledge support by the MUR PRIN2022 Project "BROWSEPOL: Beyond standard Model With cosmic microwave background Polarization"-2022EJNZ53 financed by the European Union - Next Generation EU. MB acknowledges financial support from the INFN InDark initiative and from the COSMOS network (www.cosmosnet.it) through the ASI (Italian Space Agency) Grants 2016-24-H.0, 2016-24-H.1-2018, 2020-9-HH.0 (participation in LiteBIRD phase A). ZS acknowledge ITP institute funding from DFG project 456622116 and IRAP lab support. DS acknowledges financial support from the Fondecyt Regular project number 1200171. GCH acknowledges support through the ESA research fellowship programme. JJ acknowledges support by the Swedish Research Council (VR) under the project 2020-05143 – 'Deciphering the Dynamics of Cosmic Structure'. GL acknowledges support by the ANR BIG4 project, grant ANR-16-CE23-0002 of the French Agence Nationale de la Recherche. AA, JJ, and GL acknowledge the support of the Simons Collaboration on "Learning the Universe". DP acknowledges financial support by agreement n. 2020-9-HH.0 ASI-UniRM2. JV was supported by Ruth och Nils-Erik Stenbäcks Stiftelse.

The *Euclid* Consortium acknowledges the European Space Agency and a number of agencies and institutes that have supported the development of *Euclid*, in particular the Agenzia Spaziale Italiana, the Austrian Forschungsförderungsgesellschaft funded through BMK, the Belgian Science Policy, the Canadian *Euclid* Consortium, the Deutsches Zentrum für Luft- und Raumfahrt, the DTU Space and the Niels Bohr Institute in Denmark, the French Centre National d'Etudes Spatiales, the Fundação para a Ciência e a Tecnologia, the Hungarian Academy of Sciences, the Ministerio de Ciencia, Innovación y Universidades, the National Aeronautics and Space Administration, the National Astronomical Observatory of Japan, the Nederlandse Onderzoeksschool Voor Astronomie, the Norwegian Space Agency, the Research Council of Finland, the Romanian Space Agency, the State Secretariat for Education, Research, and Innovation (SERI) at the Swiss Space Office (SSO), and the United Kingdom Space Agency. A complete and detailed list is available on the *Euclid* web site (www.euclid-ec.org).

References

Achúcarro, A., Biagetti, M., Braglia, M., et al. 2022, [arXiv:2203.08128](https://arxiv.org/abs/2203.08128)
 Achúcarro, A., Gong, J.-O., Hardeman, S., Palma, G. A., & Patil, S. P. 2011, *JCAP*, 01, 030
 Adame, A. G., Aguilar, J., Ahlen, S., et al. 2025, *JCAP*, 02, 021
 Adams, J., Cresswell, B., & Easther, R. 2001, *Phys. Rev. D*, 64, 123514
 Ade, P., Aguirre, J., Ahmed, Z., et al. 2019, *JCAP*, 02, 056
 Afshordi, N. & Tolley, A. J. 2008, *Phys. Rev. D*, 78, 123507
 Alam, S., Aubert, M., Avila, S., et al. 2021, *Phys. Rev. D*, 103, 083533
 Albrecht, A. & Steinhardt, P. J. 1982, *Phys. Rev. Lett.*, 48, 1220
 Alcock, C. & Paczynski, B. 1979, *Nature*, 281, 358
 Alvarez, M., Baldauf, T., Bond, J. R., et al. 2014, [arXiv:1412.4671](https://arxiv.org/abs/1412.4671)
 Amendola, L., Appleby, S., Avgoustidis, A., et al. 2018, *Living Reviews in Relativity*, 21, 2
 Amendola, L., Gordon, C., Wands, D., & Sasaki, M. 2002, *Phys. Rev. Lett.*, 88, 211302
 Andrews, A., Jasche, J., Lavaux, G., & Schmidt, F. 2023, *MNRAS*, 520, 5746
 Ansari Fard, M. & Baghran, S. 2018, *JCAP*, 01, 051
 Arkani-Hamed, N. & Maldacena, J. 2015, [arXiv:1503.08043](https://arxiv.org/abs/1503.08043)
 Assassi, V., Baumann, D., & Schmidt, F. 2015, *JCAP*, 12, 043
 Auclair, P. & Ringeval, C. 2022, *Phys. Rev. D*, 106, 063512
 Axenides, M., Brandenberger, R., & Turner, M. 1983, *Physics Letters B*, 126, 178

Bahr-Kalus, B., Parkinson, D., & Easther, R. 2023, *Mon. Not. Roy. Astron. Soc.*, 520, 520
 Baldauf, T., Seljak, U., Desjacques, V., & McDonald, P. 2012, *Phys. Rev. D*, 86, 083540
 Ballardini, M. 2019, *Physics of the Dark Universe*, 23, 100245
 Ballardini, M. & Barbieri, N. 2024, [arXiv:2411.02261](https://arxiv.org/abs/2411.02261)
 Ballardini, M., Davoli, A., & Samuele Sirletti, S. 2024, [arXiv:2408.05210](https://arxiv.org/abs/2408.05210)
 Ballardini, M. & Finelli, F. 2022, *JCAP*, 10, 083
 Ballardini, M., Finelli, F., Fedeli, C., & Moscardini, L. 2016, *JCAP*, 10, 041
 Bardeen, J. M., Steinhardt, P. J., & Moscardini, L. 2018, *JCAP*, 04, 044
 Ballardini, M., Finelli, F., Marulli, F., Moscardini, L., & Veropalumbo, A. 2023, *Phys. Rev. D*, 107, 043532
 Ballardini, M., Murgia, R., Baldi, M., Finelli, F., & Viel, M. 2020, *JCAP*, 04, 030
 Bardeen, J. M., Steinhardt, P. J., & Turner, M. S. 1983, *Phys. Rev. D*, 28, 679
 Barreira, A. 2020, *JCAP*, 12, 031
 Barreira, A. 2022a, *JCAP*, 11, 013
 Barreira, A. 2022b, *JCAP*, 01, 033
 Barreira, A. 2022c, *JCAP*, 04, 057
 Barreira, A., Cabass, G., Schmidt, F., Pillepich, A., & Nelson, D. 2020, *JCAP*, 12, 013
 Barreira, A. & Schmidt, F. 2017, *JCAP*, 11, 051
 Bartolo, N., Komatsu, E., Matarrese, S., & Riotto, A. 2004, *Phys. Rep.*, 402, 103
 Bartolo, N. & Liddle, A. R. 2002, *Phys. Rev. D*, 65, 121301
 Basse, T., Hamann, J., Hannestad, S., & Wong, Y. Y. Y. 2015, *JCAP*, 06, 042
 Bermejo-Clement, J. R., Ballardini, M., Finelli, F., et al. 2021, *Phys. Rev. D*, 103, 103502
 Bernardeau, F., Colombi, S., Gaztañaga, E., & Scoccimarro, R. 2002, *Phys. Rep.*, 367, 1
 Beutler, F., Biagetti, M., Green, D., Slosar, A., & Wallisch, B. 2019, *Physical Review Research*, 1, 033209
 Biagetti, M., Castiblanco, L., Noreña, J., & Sefusatti, E. 2022, *JCAP*, 09, 009
 Blas, D., Garny, M., Ivanov, M. M., & Sibiryakov, S. 2016, *JCAP*, 07, 028
 Blas, D., Lesgourgues, J., & Tram, T. 2011, *JCAP*, 07, 034
 Blot, L., Crocce, M., Sefusatti, E., et al. 2019, *MNRAS*, 485, 2806
 Boyle, A. & Komatsu, E. 2018, *JCAP*, 03, 035
 Brout, R., Englert, F., & Gunzig, E. 1978, *Ann. Phys.*, 115
 Bucher, M., Goldhaber, A. S., & Turok, N. 1995, *Phys. Rev. D*, 52, 3314
 Bucher, M., Moodley, K., & Turok, N. 2000, *Phys. Rev. D*, 62, 083508
 Byrnes, C. T. & Wands, D. 2006, *Phys. Rev. D*, 74, 043529
 Cabass, G., Ivanov, M. M., Philcox, O. H. E., Simonović, M., & Zaldarriaga, M. 2022, *Phys. Rev. Lett.*, 129, 021301
 Cagliari, M. S., Castorina, E., Bonici, M., & Bianchi, D. 2024, *JCAP*, 08, 036
 Castorina, E., Hand, N., Seljak, U., et al. 2019, *JCAP*, 09, 010
 Chan, K. C. & Blot, L. 2017, *Phys. Rev. D*, 96, 023528
 Chen, S.-F., Vlah, Z., & White, M. 2020, *JCAP*, 11, 035
 Chen, X. 2010, *JCAP*, 12, 003
 Chen, X. 2011, [arXiv:1104.1323](https://arxiv.org/abs/1104.1323)
 Chen, X., Dvorkin, C., Huang, Z., Namjoo, M. H., & Verde, L. 2016a, *JCAP*, 11, 014
 Chen, X., Easther, R., & Lim, E. A. 2007, *JCAP*, 06, 023
 Chen, X., Easther, R., & Lim, E. A. 2008, *JCAP*, 04, 010
 Chen, X., Meerburg, P. D., & Münchmeyer, M. 2016b, *JCAP*, 09, 023
 Chung, D. J., Kolb, E. W., Riotto, A., & Senatore, L. 2005, *Phys. Rev. D*, 72, 023511
 Chung, D. J. H. & Chaitanya Tadepalli, S. 2023, [arXiv:2309.17010](https://arxiv.org/abs/2309.17010)
 Chung, D. J. H., Münchmeyer, M., & Tadepalli, S. C. 2023, *Phys. Rev. D*, 108, 103542
 Chung, D. J. H. & Upadhye, A. 2018, *Phys. Rev. D*, 98, 023525
 CMB-S4 Collaboration: Abazajian, K., Addison, G., Adshead, P., et al. 2019, [arXiv:1907.04473](https://arxiv.org/abs/1907.04473)
 Creminelli, P., Nicolis, A., Senatore, L., Tegmark, M., & Zaldarriaga, M. 2006, *JCAP*, 5, 004
 Dalal, N., Doré, O., Huterer, D., & Shirokov, A. 2008, *Phys. Rev. D*, 77, 123514
 D'Amico, G., Lewandowski, M., Senatore, L., & Zhang, P. 2022, [arXiv:2201.11518](https://arxiv.org/abs/2201.11518)
 Debono, I., Hazra, D. K., Shafieloo, A., Smoot, G. F., & Starobinsky, A. A. 2020, *MNRAS*, 496, 3448
 DES Collaboration: Abbott, T. M. C., Aguena, M., Alarcon, A., et al. 2023, *Phys. Rev. D*, 107, 083504
 DESI Collaboration: Abdul-Karim, M., Aguilar, J., Ahlen, S., et al. 2025, [arXiv:2503.14738](https://arxiv.org/abs/2503.14738)
 DESI Collaboration: Aghamousa, A., Aguilar, J., Ahlen, S., et al. 2016, [arXiv:1611.00036](https://arxiv.org/abs/1611.00036)
 Desjacques, V., Jeong, D., & Schmidt, F. 2011a, *Phys. Rev. D*, 84, 061301
 Desjacques, V., Jeong, D., & Schmidt, F. 2011b, *Phys. Rev. D*, 84, 063512
 Desjacques, V., Jeong, D., & Schmidt, F. 2018, *Phys. Rep.*, 733, 1
 Desjacques, V. & Seljak, U. 2010, *Advances in Astronomy*, 2010, 908640
 di Marco, F., Finelli, F., & Brandenberger, R. 2003, *Phys. Rev. D*, 67, 063512
 Doré, O., Bock, J., Ashby, M., et al. 2014, [arXiv:1412.4872](https://arxiv.org/abs/1412.4872)
 Efsthathiou, G. & Bond, J. R. 1986, *MNRAS*, 218, 103

- Efstathiou, G. & Bond, J. R. 1999, *MNRAS*, 304, 75
- Eisenstein, D. J., Seo, H.-J., & White, M. 2007, *ApJ*, 664, 660
- Enqvist, K. & Sloth, M. S. 2002, *Nuclear Physics B*, 626, 395
- Euclid Collaboration: Andrews, A., Jasche, J., Lavaux, G., et al. 2024, [arXiv:2412.11945](https://arxiv.org/abs/2412.11945)
- Euclid Collaboration: Archidiacono, M., Lesgourgues, J., Casas, S., et al. 2025, *A&A*, 693, 693
- Euclid Collaboration: Ballardini, M., Akrami, Y., Finelli, F., et al. 2024, *A&A*, 683, A220
- Euclid Collaboration: Blanchard, A., Camera, S., Carbone, C., et al. 2020, *A&A*, 642, A191
- Euclid Collaboration: Bose, B., Carrilho, P., Marinucci, M., et al. 2024, *A&A*, 689, A275
- Euclid Collaboration: Casas, S., Cardone, V. F., Sapone, D., et al. 2023, [arXiv:2306.11053](https://arxiv.org/abs/2306.11053)
- Euclid Collaboration: Cropper, M. S., Al-Bahlawan, A., Amiaux, J., et al. 2025, *A&A*, 697, A2
- Euclid Collaboration: Frusciante, N., Pace, F., Cardone, V. F., et al. 2024, *A&A*, 690, A133
- Euclid Collaboration: Ilić, S., Aghanim, N., Baccigalupi, C., et al. 2022, *A&A*, 657, A91
- Euclid Collaboration: Jahnke, K., Gillard, W., Schirmer, M., et al. 2025, *A&A*, 697, A3
- Euclid Collaboration: Koyama, K., Pamuk, S., Casas, S., et al. 2025, *A&A*, 698, A233
- Euclid Collaboration: Lesgourgues, J., Schwagereit, J., Bucko, J., et al. 2025, *A&A*, 693, A249
- Euclid Collaboration: Mellier, Y., Abdurrouf, Acevedo Barroso, J. A., et al. 2025, *A&A*, 697, A1
- Euclid Collaboration: Scaramella, R., Amiaux, J., Mellier, Y., et al. 2022, *A&A*, 662, A112
- Fedeli, C., Finelli, F., & Moscardini, L. 2010, *MNRAS*, 407, 1842
- Fergusson, J. R., Gruetjen, H. F., Shellard, E. P. S., & Wallisch, B. 2015, *Phys. Rev. D*, 91, 123506
- Ferté, A. & Hong, K. 2024, *Phys. Rev. D*, 109, 109
- Flauger, R., McAllister, L., Pajer, E., Westphal, A., & Xu, G. 2010, *JCAP*, 06, 009
- Flauger, R. & Pajer, E. 2011, *JCAP*, 01, 017
- Fondi, E., Verde, L., Villaescusa-Navarro, F., et al. 2024, *JCAP*, 02, 048
- Gangui, A., Lucchin, F., Matarrese, S., & Mollerach, S. 1994, *ApJ*, 430, 447
- García-Bellido, J. & Wands, D. 1996, *Phys. Rev. D*, 53, 5437
- Giannantonio, T. & Porciani, C. 2010, *Phys. Rev. D*, 81, 063530
- Giannantonio, T., Porciani, C., Carron, J., Amara, A., & Pillepich, A. 2012, *MNRAS*, 422, 2854
- Gong, J.-O., Schalm, K., & Shiu, G. 2014, *Phys. Rev. D*, 89, 063540
- Gordon, C. & Lewis, A. 2003, *Phys. Rev. D*, 67, 123513
- Gordon, C., Wands, D., Bassett, B. A., & Maartens, R. 2000, *Phys. Rev. D*, 63, 023506
- Guth, A. H. 1981, *Phys. Rev. D*, 23, 347
- Guth, A. H. & Pi, S. Y. 1982, *Phys. Rev. Lett.*, 49, 1110
- Gutiérrez Adame, A., Avila, S., Gonzalez-Perez, V., et al. 2024, *A&A*, 689, A69
- Hamilton, A. J. S. 1998, in *Astrophysics and Space Science Library*, Vol. 231, The Evolving Universe, ed. D. Hamilton, 185
- Hawking, S. W. 1982, *Phys. Lett. B*, 115, 295
- Hawking, S. W., Moss, I. G., & Stewart, J. M. 1982, *Phys. Rev. D*, 26, 2681
- Howlett, C. & Percival, W. J. 2017, *MNRAS*, 472, 4935
- Huang, Z., Verde, L., & Vernizzi, F. 2012, *JCAP*, 04, 04
- Jasche, J. & Lavaux, G. 2019, *A&A*, 625, A64
- Jasche, J., Leclercq, F., & Wandelt, B. D. 2015, *JCAP*, 01, 036
- Jasche, J. & Wandelt, B. D. 2013, *MNRAS*, 432, 894
- Kaiser, N. 1987, *MNRAS*, 227, 1
- Karagiannis, D., Lazanu, A., Liguori, M., et al. 2018, *MNRAS*, 478, 1341
- Karagiannis, D., Slosar, A., & Liguori, M. 2020, *JCAP*, 11, 052
- Kasuya, S. & Kawasaki, M. 2009, *Phys. Rev. D*, 80, 023516
- Kawasaki, M. & Nakayama, K. 2013, *Annual Review of Nuclear and Particle Science*, 63, 69
- Kleban, M. & Schillo, M. 2012, *JCAP*, 06, 029
- Knox, L. 1995, *Phys. Rev. D*, 52, 4307
- Kobayashi, T. & Takahashi, F. 2016, *JCAP*, 08, 056
- Kolb, E. W. & Long, A. J. 2017, *Phys. Rev. D*, 96, 103540
- Komatsu, E. & Spergel, D. N. 2001, *Phys. Rev. D*, 63, 063002
- Kosowsky, A. & Turner, M. S. 1995, *Phys. Rev. D*, 52, R1739
- Langlois, D. 1999, *Phys. Rev. D*, 59, 123512
- Langlois, D. & Riazuelo, A. 2000, *Phys. Rev. D*, 62, 043504
- Langlois, D., Vernizzi, F., & Wands, D. 2008, *JCAP*, 12, 004
- Laureijs, R., Amiaux, J., Arduini, S., et al. 2011, *ESA/SRE(2011)12*, [arXiv:1110.3193](https://arxiv.org/abs/1110.3193)
- Lavaux, G. & Jasche, J. 2016, *MNRAS*, 455, 3169
- Lavaux, G., Jasche, J., & Leclercq, F. 2019, [arXiv:1909.06396](https://arxiv.org/abs/1909.06396)
- Lazeyras, T., Barreira, A., Schmidt, F., & Desjacques, V. 2023, *JCAP*, 01, 023
- Leistedt, B., Peiris, H. V., & Roth, N. 2014, *Phys. Rev. Lett.*, 113, 221301
- Lewis, A., Challinor, A., & Lasenby, A. 2000, *ApJ*, 538, 473
- Li, Y., Singh, S., Yu, B., Feng, Y., & Seljak, U. 2019, *JCAP*, 01, 016
- Li, Y., Zhu, H.-M., & Li, B. 2022, *MNRAS*, 514, 4363
- Linde, A. & Mukhanov, V. 1997, *Phys. Rev. D*, 56, R535
- Linde, A. D. 1982, *Physics Letters B*, 108, 389
- Linde, A. D. 1983, *Physics Letters B*, 129, 177
- Linde, A. D. 1985, *Physics Letters B*, 158, 375
- LiteBIRD Collaboration, Allys, E., Arnold, K., et al. 2023, *Progress of Theoretical and Experimental Physics*, 2023, 042F01
- LSST Science Collaboration, Abell, P. A., Allison, J., et al. 2009, [arXiv:0912.0201](https://arxiv.org/abs/0912.0201)
- Lucie-Smith, L., Barreira, A., & Schmidt, F. 2023, *MNRAS*, 524, 1746
- Lyth, D. H., Ungarelli, C., & Wands, D. 2003, *Phys. Rev. D*, 67, 023503
- Lyth, D. H. & Wands, D. 2002, *Physics Letters B*, 524, 5
- Mangilli, A., Verde, L., & Beltran, M. 2010, *JCAP*, 10, 009
- Marsh, D. J. E. 2016, *Phys. Rep.*, 643, 1
- Matarrese, S. & Verde, L. 2008, *ApJ*, 677, L77
- McDonald, P. & Roy, A. 2009, *JCAP*, 08, 020
- Mead, A. J., Heymans, C., Lombriser, L., et al. 2016, *MNRAS*, 459, 1468
- Mead, A. J., Peacock, J. A., Heymans, C., Joudaki, S., & Heavens, A. F. 2015, *MNRAS*, 454, 1958
- Meerburg, P. D., Green, D., Flauger, R., et al. 2019, *BAAS*, 51, 107
- Meerburg, P. D., Münchmeyer, M., & Wandelt, B. 2016, *Phys. Rev. D*, 93, 043536
- Mergulhão, T., Beutler, F., & Peacock, J. A. 2023, *JCAP*, 08, 012
- Mollerach, S. 1990, *Phys. Rev. D*, 42, 313
- Mooij, S., Palma, G. A., Panotopoulos, G., & Soto, A. 2015, *JCAP*, 10, 062
- Moroi, T. & Takahashi, T. 2001, *Physics Letters B*, 522, 215
- Muñoz, J. B., Kovetz, E. D., Raccanelli, A., Kamionkowski, M., & Silk, J. 2017, *JCAP*, 05, 05
- Mueller, E.-M., Rezaie, M., Percival, W. J., et al. 2022, *MNRAS*, 514, 3396
- Mukhanov, V. F. 1985, *Soviet Journal of Experimental and Theoretical Physics Letters*, 41, 493
- Mukhanov, V. F. & Chibisov, G. V. 1981, *Soviet Journal of Experimental and Theoretical Physics Letters*, 33, 532
- Muya Kasanda, S., Zunckel, C., Moodley, K., Bassett, B. A., & Okouma, P. 2012, *JCAP*, 07, 021
- Okamoto, T. & Hu, W. 2003, *Phys. Rev. D*, 67, 083002
- Palanque-Delabrouille, N., Yèche, C., Schöneberg, N., et al. 2020, *JCAP*, 04, 038
- Palma, G. A., Sapone, D., & Sypsas, S. 2018, *JCAP*, 06, 004
- Peebles, P. J. E. 1999, *ApJ*, 510, 523
- Planck Collaboration: Ade, P. A. R., Aghanim, N., Arnaud, M., et al. 2016, *A&A*, 594, A20
- Planck Collaboration: Aghanim, N., Akrami, Y., Arroja, F., et al. 2020a, *A&A*, 641, A1
- Planck Collaboration: Aghanim, N., Akrami, Y., Ashdown, M., et al. 2020b, *A&A*, 641, A6
- Planck Collaboration: Akrami, Y., Arroja, F., Ashdown, M., et al. 2020a, *A&A*, 641, A10
- Planck Collaboration: Akrami, Y., Arroja, F., Ashdown, M., et al. 2020b, *A&A*, 641, A9
- Polarski, D. & Starobinsky, A. A. 1994, *Phys. Rev. D*, 50, 6123
- Rezaie, M., Ross, A. J., Seo, H.-J., et al. 2024, *MNRAS*, 532, 1902
- Salopek, D. S. & Bond, J. R. 1990, *Phys. Rev. D*, 42, 3936
- Sasaki, M. & Stewart, E. D. 1996, *Progress of Theoretical Physics*, 95, 71
- Sato, K. 1981, *MNRAS*, 195, 467
- Schmid, F. & Hui, L. 2013, *Physical Review Letters*, 110, 011301
- Schmidt, F., Jeong, D., & Desjacques, V. 2013, *Phys. Rev. D*, 88, 023515
- Schmidt, F. & Kamionkowski, M. 2010, *Phys. Rev. D*, 82, 103002
- Scoccimarro, R., Couchman, H. M. P., & Frieman, J. A. 1999, *ApJ*, 517, 531
- Scoccimarro, R., Hui, L., Manera, M., & Chan, K. C. 2012, *Phys. Rev. D*, 85, 083002
- Sefusatti, E., Crocce, M., Pueblas, S., & Scoccimarro, R. 2006, *Phys. Rev. D*, 74, 023522
- Senatore, L., Smith, K. M., & Zaldarriaga, M. 2010, *JCAP*, 1, 028
- Slosar, A., Hirata, C., Seljak, U., Ho, S., & Padmanabhan, N. 2008, *JCAP*, 08, 031
- Smith, R. E. & Angulo, R. E. 2019, *MNRAS*, 486, 1448
- Smith, R. E., Peacock, J. A., Jenkins, A., et al. 2003, *MNRAS*, 341, 1311
- Springel, V. 2005, *MNRAS*, 364, 1105
- Springel, V., White, S. D. M., Tormen, G., & Kauffmann, G. 2001, *MNRAS*, 328, 726
- Starobinsky, A. A. 1979, *JETP Lett.*, 30, 30
- Starobinsky, A. A. 1980, *Physics Letters B*, 91, 99
- Starobinsky, A. A. 1982, *Physics Letters B*, 117, 175
- Starobinsky, A. A. 1992, *Soviet Journal of Experimental and Theoretical Physics Letters*, 55, 489

- Takahashi, R., Sato, M., Nishimichi, T., Taruya, A., & Oguri, M. 2012, *ApJ*, **761**, 152
- Tassev, S., Eisenstein, D. J., Wandelt, B. D., & Zaldarriaga, M. 2015, [arXiv:1502.07751](https://arxiv.org/abs/1502.07751)
- Tassev, S., Zaldarriaga, M., & Eisenstein, D. J. 2013, *JCAP*, **06**, 036
- Taylor, P. L., Kitching, T. D., McEwen, J. D., & Tram, T. 2018, *Phys. Rev. D*, **98**, 98
- Teyssier, R. 2002, *A&A*, **385**, 337
- Tinker, J. L., Robertson, B. E., Kravtsov, A. V., et al. 2010, *ApJ*, **724**, 878
- Väliiviita, J. & Muhonen, V. 2003, *Phys. Rev. Lett.*, **91**, 131302
- Väliiviita, J., Savelainen, M., Talvitie, M., Kurki-Suonio, H., & Rusak, S. 2012, *ApJ*, **753**, 151
- Vasudevan, A., Ivanov, M. M., Sibiryakov, S., & Lesgourgues, J. 2019, *JCAP*, **09**, 037
- Verde, L. & Matarrese, S. 2009, *ApJ*, **706**, L91
- Verde, L., Wang, L., Heavens, A. F., & Kamionkowski, M. 2000, *MNRAS*, **313**, 141
- Wang, Y., Chuang, C.-H., & Hirata, C. M. 2013, *MNRAS*, **430**, 2446
- Wang, Y., Spergel, D. N., & Strauss, M. A. 1999, *ApJ*, **510**, 20
- Waterhouse, T. P. & Zibin, J. P. 2008, [arXiv:0804.1771](https://arxiv.org/abs/0804.1771)
- Weinberg, S. 1978, *Phys. Rev. Lett.*, **40**, 223
- Wilczek, F. 1978, *Phys. Rev. Lett.*, **40**, 279
- Winther, H. A., Koyama, K., Manera, M., Wright, B. S., & Zhao, G.-B. 2017, *JCAP*, **08**, 006
- Wright, B. S., Winther, H. A., & Koyama, K. 2017, *JCAP*, **10**, 054
- Xu, Y., Hamann, J., & Chen, X. 2016, *Phys. Rev. D*, **94**, 123518
- Yankelevich, V. & Porciani, C. 2019, *MNRAS*, **483**, 2078
- Zhan, H., Knox, L., Tyson, J. A., & Margoniner, V. 2006, *ApJ*, **640**, 8
- ²³ Leiden Observatory, Leiden University, Einsteinweg 55, 2333 CC Leiden, The Netherlands
- ²⁴ Institut d'Astrophysique de Paris, 98bis Boulevard Arago, 75014, Paris, France
- ²⁵ Oskar Klein Centre for Cosmoparticle Physics, Department of Physics, Stockholm University, Stockholm, SE-106 91, Sweden
- ²⁶ Institut d'Astrophysique de Paris, UMR 7095, CNRS, and Sorbonne Université, 98 bis boulevard Arago, 75014 Paris, France
- ²⁷ Université Paris-Saclay, CNRS, Institut d'astrophysique spatiale, 91405, Orsay, France
- ²⁸ ESAC/ESA, Camino Bajo del Castillo, s/n., Urb. Villafranca del Castillo, 28692 Villanueva de la Cañada, Madrid, Spain
- ²⁹ School of Mathematics and Physics, University of Surrey, Guildford, Surrey, GU2 7XH, UK
- ³⁰ INAF-Osservatorio Astronomico di Brera, Via Brera 28, 20122 Milano, Italy
- ³¹ IFPU, Institute for Fundamental Physics of the Universe, via Beirut 2, 34151 Trieste, Italy
- ³² INAF-Osservatorio Astronomico di Trieste, Via G. B. Tiepolo 11, 34143 Trieste, Italy
- ³³ INFN, Sezione di Trieste, Via Valerio 2, 34127 Trieste TS, Italy
- ³⁴ SISSA, International School for Advanced Studies, Via Bonomea 265, 34136 Trieste TS, Italy
- ³⁵ Centre National d'Etudes Spatiales – Centre spatial de Toulouse, 18 avenue Edouard Belin, 31401 Toulouse Cedex 9, France
- ³⁶ Dipartimento di Fisica e Astronomia, Università di Bologna, Via Gobetti 93/2, 40129 Bologna, Italy
- ³⁷ INFN-Sezione di Bologna, Viale Berti Pichat 6/2, 40127 Bologna, Italy
- ³⁸ Dipartimento di Fisica, Università di Genova, Via Dodecaneso 33, 16146, Genova, Italy
- ³⁹ INFN-Sezione di Genova, Via Dodecaneso 33, 16146, Genova, Italy
- ⁴⁰ Department of Physics "E. Pancini", University Federico II, Via Cinthia 6, 80126, Napoli, Italy
- ⁴¹ INAF-Osservatorio Astronomico di Capodimonte, Via Moiariello 16, 80131 Napoli, Italy
- ⁴² Dipartimento di Fisica, Università degli Studi di Torino, Via P. Giuria 1, 10125 Torino, Italy
- ⁴³ INFN-Sezione di Torino, Via P. Giuria 1, 10125 Torino, Italy
- ⁴⁴ INAF-Osservatorio Astrofisico di Torino, Via Osservatorio 20, 10025 Pino Torinese (TO), Italy
- ⁴⁵ INAF-IASF Milano, Via Alfonso Corti 12, 20133 Milano, Italy
- ⁴⁶ Centro de Investigaciones Energéticas, Medioambientales y Tecnológicas (CIEMAT), Avenida Complutense 40, 28040 Madrid, Spain
- ⁴⁷ Port d'Informació Científica, Campus UAB, C. Albareda s/n, 08193 Bellaterra (Barcelona), Spain
- ⁴⁸ INAF-Osservatorio Astronomico di Roma, Via Frascati 33, 00078 Monteporzio Catone, Italy
- ⁴⁹ INFN section of Naples, Via Cinthia 6, 80126, Napoli, Italy
- ⁵⁰ Institute for Astronomy, University of Hawaii, 2680 Woodlawn Drive, Honolulu, HI 96822, USA
- ⁵¹ Dipartimento di Fisica e Astronomia "Augusto Righi" - Alma Mater Studiorum Università di Bologna, Viale Berti Pichat 6/2, 40127 Bologna, Italy
- ⁵² Institute for Astronomy, University of Edinburgh, Royal Observatory, Blackford Hill, Edinburgh EH9 3HJ, UK
- ⁵³ Jodrell Bank Centre for Astrophysics, Department of Physics and Astronomy, University of Manchester, Oxford Road, Manchester M13 9PL, UK
- ⁵⁴ European Space Agency/ESRIN, Largo Galileo Galilei 1, 00044 Frascati, Roma, Italy
- ⁵⁵ Université Claude Bernard Lyon 1, CNRS/IN2P3, IP2I Lyon, UMR 5822, Villeurbanne, F-69100, France
- ⁵⁶ Institut de Ciències del Cosmos (ICCUB), Universitat de Barcelona (IEEC-UB), Martí i Franquès 1, 08028 Barcelona, Spain
- ⁵⁷ Institució Catalana de Recerca i Estudis Avançats (ICREA), Passeig de Lluís Companys 23, 08010 Barcelona, Spain
- ¹ INAF-Osservatorio di Astrofisica e Scienza dello Spazio di Bologna, Via Piero Gobetti 93/3, 40129 Bologna, Italy
- ² INFN-Bologna, Via Irnerio 46, 40126 Bologna, Italy
- ³ Instituto de Física Teórica UAM-CSIC, Campus de Cantoblanco, 28049 Madrid, Spain
- ⁴ CERCA/ISO, Department of Physics, Case Western Reserve University, 10900 Euclid Avenue, Cleveland, OH 44106, USA
- ⁵ Dipartimento di Fisica e Scienze della Terra, Università degli Studi di Ferrara, Via Giuseppe Saragat 1, 44122 Ferrara, Italy
- ⁶ Istituto Nazionale di Fisica Nucleare, Sezione di Ferrara, Via Giuseppe Saragat 1, 44122 Ferrara, Italy
- ⁷ Institute for Theoretical Particle Physics and Cosmology (TTK), RWTH Aachen University, 52056 Aachen, Germany
- ⁸ Department of Physics and Astronomy, University of the Western Cape, Bellville, Cape Town, 7535, South Africa
- ⁹ Institut für Theoretische Physik, University of Heidelberg, Philosophenweg 16, 69120 Heidelberg, Germany
- ¹⁰ Institut de Recherche en Astrophysique et Planétologie (IRAP), Université de Toulouse, CNRS, UPS, CNES, 14 Av. Edouard Belin, 31400 Toulouse, France
- ¹¹ Université St Joseph; Faculty of Sciences, Beirut, Lebanon
- ¹² Department of Physics, P.O. Box 64, 00014 University of Helsinki, Finland
- ¹³ Helsinki Institute of Physics, Gustaf Hällströmin katu 2, University of Helsinki, Helsinki, Finland
- ¹⁴ Dipartimento di Fisica e Astronomia "G. Galilei", Università di Padova, Via Marzolo 8, 35131 Padova, Italy
- ¹⁵ INFN-Padova, Via Marzolo 8, 35131 Padova, Italy
- ¹⁶ INAF-Osservatorio Astronomico di Padova, Via dell'Osservatorio 5, 35122 Padova, Italy
- ¹⁷ Instituto de Astrofísica de Canarias, Vía Láctea, 38205 La Laguna, Tenerife, Spain
- ¹⁸ Universidad de La Laguna, Departamento de Astrofísica, 38206 La Laguna, Tenerife, Spain
- ¹⁹ Departamento de Física, FCFM, Universidad de Chile, Blanco Encalada 2008, Santiago, Chile
- ²⁰ Institute Lorentz, Leiden University, Niels Bohrweg 2, 2333 CA Leiden, The Netherlands
- ²¹ Departamento de Física, Universidad del País Vasco UPV-EHU, 48940 Leioa, Spain
- ²² European Space Agency/ESTEC, Keplerlaan 1, 2201 AZ Noordwijk, The Netherlands

- 58 UCB Lyon 1, CNRS/IN2P3, IUF, IP2I Lyon, 4 rue Enrico Fermi, 69622 Villeurbanne, France
- 59 Mullard Space Science Laboratory, University College London, Holmbury St Mary, Dorking, Surrey RH5 6NT, UK
- 60 Departamento de Física, Faculdade de Ciências, Universidade de Lisboa, Edifício C8, Campo Grande, PT1749-016 Lisboa, Portugal
- 61 Instituto de Astrofísica e Ciências do Espaço, Faculdade de Ciências, Universidade de Lisboa, Campo Grande, 1749-016 Lisboa, Portugal
- 62 Department of Astronomy, University of Geneva, ch. d'Ecogia 16, 1290 Versoix, Switzerland
- 63 Aix-Marseille Université, CNRS, CNES, LAM, Marseille, France
- 64 INAF-Istituto di Astrofisica e Planetologia Spaziali, via del Fosso del Cavaliere, 100, 00100 Roma, Italy
- 65 Aix-Marseille Université, CNRS/IN2P3, CPPM, Marseille, France
- 66 Space Science Data Center, Italian Space Agency, via del Politecnico snc, 00133 Roma, Italy
- 67 Institut d'Estudis Espacials de Catalunya (IEEC), Edifici RDIT, Campus UPC, 08860 Castelldefels, Barcelona, Spain
- 68 Institute of Space Sciences (ICE, CSIC), Campus UAB, Carrer de Can Magrans, s/n, 08193 Barcelona, Spain
- 69 Universitäts-Sternwarte München, Fakultät für Physik, Ludwig-Maximilians-Universität München, Scheinerstrasse 1, 81679 München, Germany
- 70 Max Planck Institute for Extraterrestrial Physics, Giessenbachstr. 1, 85748 Garching, Germany
- 71 Institute of Theoretical Astrophysics, University of Oslo, P.O. Box 1029 Blindern, 0315 Oslo, Norway
- 72 Jet Propulsion Laboratory, California Institute of Technology, 4800 Oak Grove Drive, Pasadena, CA, 91109, USA
- 73 Department of Physics, Lancaster University, Lancaster, LA1 4YB, UK
- 74 Felix Hormuth Engineering, Goethestr. 17, 69181 Leimen, Germany
- 75 Technical University of Denmark, Elektrovej 327, 2800 Kgs. Lyngby, Denmark
- 76 Cosmic Dawn Center (DAWN), Denmark
- 77 Max-Planck-Institut für Astronomie, Königstuhl 17, 69117 Heidelberg, Germany
- 78 NASA Goddard Space Flight Center, Greenbelt, MD 20771, USA
- 79 Department of Physics and Astronomy, University College London, Gower Street, London WC1E 6BT, UK
- 80 Department of Physics and Helsinki Institute of Physics, Gustaf Hällströmin katu 2, 00014 University of Helsinki, Finland
- 81 Université de Genève, Département de Physique Théorique and Centre for Astroparticle Physics, 24 quai Ernest-Ansermet, CH-1211 Genève 4, Switzerland
- 82 Laboratoire d'étude de l'Univers et des phénomènes eXtremes, Observatoire de Paris, Université PSL, Sorbonne Université, CNRS, 92190 Meudon, France
- 83 SKA Observatory, Jodrell Bank, Lower Withington, Macclesfield, Cheshire SK11 9FT, UK
- 84 Centre de Calcul de l'IN2P3/CNRS, 21 avenue Pierre de Coubertin 69627 Villeurbanne Cedex, France
- 85 Dipartimento di Fisica "Aldo Pontremoli", Università degli Studi di Milano, Via Celoria 16, 20133 Milano, Italy
- 86 INFN-Sezione di Milano, Via Celoria 16, 20133 Milano, Italy
- 87 University of Applied Sciences and Arts of Northwestern Switzerland, School of Computer Science, 5210 Windisch, Switzerland
- 88 Universität Bonn, Argelander-Institut für Astronomie, Auf dem Hügel 71, 53121 Bonn, Germany
- 89 INFN-Sezione di Roma, Piazzale Aldo Moro, 2 - c/o Dipartimento di Fisica, Edificio G. Marconi, 00185 Roma, Italy
- 90 Dipartimento di Fisica e Astronomia "Augusto Righi" - Alma Mater Studiorum Università di Bologna, via Piero Gobetti 93/2, 40129 Bologna, Italy
- 91 Department of Physics, Institute for Computational Cosmology, Durham University, South Road, Durham, DH1 3LE, UK
- 92 Université Paris Cité, CNRS, Astroparticule et Cosmologie, 75013 Paris, France
- 93 CNRS-UCB International Research Laboratory, Centre Pierre Binétruy, IRL2007, CPB-IN2P3, Berkeley, USA
- 94 Institute of Physics, Laboratory of Astrophysics, Ecole Polytechnique Fédérale de Lausanne (EPFL), Observatoire de Sauverny, 1290 Versoix, Switzerland
- 95 Telespazio UK S.L. for European Space Agency (ESA), Camino bajo del Castillo, s/n, Urbanización Villafranca del Castillo, Villanueva de la Cañada, 28692 Madrid, Spain
- 96 Institut de Física d'Altes Energies (IFAE), The Barcelona Institute of Science and Technology, Campus UAB, 08193 Bellaterra (Barcelona), Spain
- 97 DARK, Niels Bohr Institute, University of Copenhagen, Jagtvej 155, 2200 Copenhagen, Denmark
- 98 Waterloo Centre for Astrophysics, University of Waterloo, Waterloo, Ontario N2L 3G1, Canada
- 99 Department of Physics and Astronomy, University of Waterloo, Waterloo, Ontario N2L 3G1, Canada
- 100 Perimeter Institute for Theoretical Physics, Waterloo, Ontario N2L 2Y5, Canada
- 101 Université Paris-Saclay, Université Paris Cité, CEA, CNRS, AIM, 91191, Gif-sur-Yvette, France
- 102 Institute of Space Science, Str. Atomistilor, nr. 409 Măgurele, Ilfov, 077125, Romania
- 103 Consejo Superior de Investigaciones Científicas, Calle Serrano 117, 28006 Madrid, Spain
- 104 Universität Innsbruck, Institut für Astro- und Teilchenphysik, Technikerstr. 25/8, 6020 Innsbruck, Austria
- 105 Satlantis, University Science Park, Sede Bld 48940, Leioa-Bilbao, Spain
- 106 Department of Physics, Royal Holloway, University of London, TW20 0EX, UK
- 107 Instituto de Astrofísica e Ciências do Espaço, Faculdade de Ciências, Universidade de Lisboa, Tapada da Ajuda, 1349-018 Lisboa, Portugal
- 108 Cosmic Dawn Center (DAWN)
- 109 Niels Bohr Institute, University of Copenhagen, Jagtvej 128, 2200 Copenhagen, Denmark
- 110 Universidad Politécnica de Cartagena, Departamento de Electrónica y Tecnología de Computadoras, Plaza del Hospital 1, 30202 Cartagena, Spain
- 111 Kapteyn Astronomical Institute, University of Groningen, PO Box 800, 9700 AV Groningen, The Netherlands
- 112 Infrared Processing and Analysis Center, California Institute of Technology, Pasadena, CA 91125, USA
- 113 INAF, Istituto di Radioastronomia, Via Piero Gobetti 101, 40129 Bologna, Italy
- 114 Astronomical Observatory of the Autonomous Region of the Aosta Valley (OAVdA), Loc. Lignan 39, I-11020, Nus (Aosta Valley), Italy
- 115 Université Côte d'Azur, Observatoire de la Côte d'Azur, CNRS, Laboratoire Lagrange, Bd de l'Observatoire, CS 34229, 06304 Nice cedex 4, France
- 116 Department of Physics, Oxford University, Keble Road, Oxford OX1 3RH, UK
- 117 Aurora Technology for European Space Agency (ESA), Camino bajo del Castillo, s/n, Urbanización Villafranca del Castillo, Villanueva de la Cañada, 28692 Madrid, Spain
- 118 Department of Mathematics and Physics E. De Giorgi, University of Salento, Via per Arnesano, CP-I93, 73100, Lecce, Italy
- 119 INFN, Sezione di Lecce, Via per Arnesano, CP-I93, 73100, Lecce, Italy
- 120 INAF-Sezione di Lecce, c/o Dipartimento Matematica e Fisica, Via per Arnesano, 73100, Lecce, Italy
- 121 INAF - Osservatorio Astronomico di Brera, via Emilio Bianchi 46, 23807 Merate, Italy
- 122 INAF-Osservatorio Astronomico di Brera, Via Brera 28, 20122 Milano, Italy, and INFN-Sezione di Genova, Via Dodecaneso 33, 16146, Genova, Italy
- 123 ICL, Junia, Université Catholique de Lille, LITL, 59000 Lille, France

- ¹²⁴ ICSC - Centro Nazionale di Ricerca in High Performance Computing, Big Data e Quantum Computing, Via Magnanelli 2, Bologna, Italy
- ¹²⁵ Technical University of Munich, TUM School of Natural Sciences, Physics Department, James-Franck-Str. 1, 85748 Garching, Germany
- ¹²⁶ Max-Planck-Institut für Astrophysik, Karl-Schwarzschild-Str. 1, 85748 Garching, Germany
- ¹²⁷ Departamento de Física Fundamental. Universidad de Salamanca. Plaza de la Merced s/n. 37008 Salamanca, Spain
- ¹²⁸ Instituto de Astrofísica de Canarias (IAC); Departamento de Astrofísica, Universidad de La Laguna (ULL), 38200, La Laguna, Tenerife, Spain
- ¹²⁹ Université de Strasbourg, CNRS, Observatoire astronomique de Strasbourg, UMR 7550, 67000 Strasbourg, France
- ¹³⁰ Center for Data-Driven Discovery, Kavli IPMU (WPI), UTIAS, The University of Tokyo, Kashiwa, Chiba 277-8583, Japan
- ¹³¹ Ludwig-Maximilians-University, Schellingstrasse 4, 80799 Munich, Germany
- ¹³² Max-Planck-Institut für Physik, Boltzmannstr. 8, 85748 Garching, Germany
- ¹³³ Dipartimento di Fisica - Sezione di Astronomia, Università di Trieste, Via Tiepolo 11, 34131 Trieste, Italy
- ¹³⁴ California Institute of Technology, 1200 E California Blvd, Pasadena, CA 91125, USA
- ¹³⁵ Department of Physics & Astronomy, University of California Irvine, Irvine CA 92697, USA
- ¹³⁶ Departamento Física Aplicada, Universidad Politécnica de Cartagena, Campus Muralla del Mar, 30202 Cartagena, Murcia, Spain
- ¹³⁷ Instituto de Física de Cantabria, Edificio Juan Jordá, Avenida de los Castros, 39005 Santander, Spain
- ¹³⁸ Observatorio Nacional, Rua General Jose Cristino, 77-Bairro Imperial de Sao Cristovao, Rio de Janeiro, 20921-400, Brazil
- ¹³⁹ CEA Saclay, DFR/IRFU, Service d'Astrophysique, Bat. 709, 91191 Gif-sur-Yvette, France
- ¹⁴⁰ Institute of Cosmology and Gravitation, University of Portsmouth, Portsmouth PO1 3FX, UK
- ¹⁴¹ Department of Computer Science, Aalto University, PO Box 15400, Espoo, FI-00 076, Finland
- ¹⁴² Instituto de Astrofísica de Canarias, c/ Via Lactea s/n, La Laguna 38200, Spain. Departamento de Astrofísica de la Universidad de La Laguna, Avda. Francisco Sanchez, La Laguna, 38200, Spain
- ¹⁴³ Caltech/IPAC, 1200 E. California Blvd., Pasadena, CA 91125, USA
- ¹⁴⁴ Ruhr University Bochum, Faculty of Physics and Astronomy, Astronomical Institute (AIRUB), German Centre for Cosmological Lensing (GCCL), 44780 Bochum, Germany
- ¹⁴⁵ Department of Physics and Astronomy, Vesilinnantie 5, 20014 University of Turku, Finland
- ¹⁴⁶ Serco for European Space Agency (ESA), Camino bajo del Castillo, s/n, Urbanizacion Villafranca del Castillo, Villanueva de la Cañada, 28692 Madrid, Spain
- ¹⁴⁷ ARC Centre of Excellence for Dark Matter Particle Physics, Melbourne, Australia
- ¹⁴⁸ Centre for Astrophysics & Supercomputing, Swinburne University of Technology, Hawthorn, Victoria 3122, Australia
- ¹⁴⁹ DAMTP, Centre for Mathematical Sciences, Wilberforce Road, Cambridge CB3 0WA, UK
- ¹⁵⁰ Kavli Institute for Cosmology Cambridge, Madingley Road, Cambridge, CB3 0HA, UK
- ¹⁵¹ Department of Astrophysics, University of Zurich, Winterthurerstrasse 190, 8057 Zurich, Switzerland
- ¹⁵² Department of Physics, Centre for Extragalactic Astronomy, Durham University, South Road, Durham, DH1 3LE, UK
- ¹⁵³ IRFU, CEA, Université Paris-Saclay 91191 Gif-sur-Yvette Cedex, France
- ¹⁵⁴ Univ. Grenoble Alpes, CNRS, Grenoble INP, LPSC-IN2P3, 53, Avenue des Martyrs, 38000, Grenoble, France
- ¹⁵⁵ INAF-Osservatorio Astrofisico di Arcetri, Largo E. Fermi 5, 50125, Firenze, Italy
- ¹⁵⁶ Dipartimento di Fisica, Sapienza Università di Roma, Piazzale Aldo Moro 2, 00185 Roma, Italy
- ¹⁵⁷ Centro de Astrofísica da Universidade do Porto, Rua das Estrelas, 4150-762 Porto, Portugal
- ¹⁵⁸ Instituto de Astrofísica e Ciências do Espaço, Universidade do Porto, CAUP, Rua das Estrelas, PT4150-762 Porto, Portugal
- ¹⁵⁹ Dipartimento di Fisica, Università di Roma Tor Vergata, Via della Ricerca Scientifica 1, Roma, Italy
- ¹⁶⁰ INFN, Sezione di Roma 2, Via della Ricerca Scientifica 1, Roma, Italy
- ¹⁶¹ HE Space for European Space Agency (ESA), Camino bajo del Castillo, s/n, Urbanizacion Villafranca del Castillo, Villanueva de la Cañada, 28692 Madrid, Spain
- ¹⁶² Theoretical astrophysics, Department of Physics and Astronomy, Uppsala University, Box 516, 751 37 Uppsala, Sweden
- ¹⁶³ Mathematical Institute, University of Leiden, Einsteinweg 55, 2333 CA Leiden, The Netherlands
- ¹⁶⁴ Institute of Astronomy, University of Cambridge, Madingley Road, Cambridge CB3 0HA, UK
- ¹⁶⁵ Department of Astrophysical Sciences, Peyton Hall, Princeton University, Princeton, NJ 08544, USA
- ¹⁶⁶ Space physics and astronomy research unit, University of Oulu, Pentti Kaiteran katu 1, FI-90014 Oulu, Finland
- ¹⁶⁷ Institut de Physique Théorique, CEA, CNRS, Université Paris-Saclay 91191 Gif-sur-Yvette Cedex, France
- ¹⁶⁸ Center for Computational Astrophysics, Flatiron Institute, 162 5th Avenue, 10010, New York, NY, USA

Appendix A: Combination with current and future CMB measurements

In this appendix, we summarise how we compute and add the cosmological information from current and future measurements of CMB temperature, E -mode polarisation, and lensing. Comparing and folding in the information contained in CMB anisotropies is important for the forecasts studied here, and more generally, for the physics of the early Universe. The comparison shows how well *Euclid* can probe initial conditions in the low-redshift and non-linear regime compared to the high-redshift and linear regime of the CMB, which is currently the most precise probe of the early Universe. The combination of CMB measurements and *Euclid* will show the complementarity of the two probes and will break many of the degeneracies present in each independent probe, leading to tighter constraints.

We follow the recipes described in more detailed in [Euclid Collaboration: Ilić et al. \(2022\)](#), where the interested reader can find the joint study of *Euclid* and CMB probes. Note, however, that in this paper we do not include the cross-correlation between *Euclid* and CMB measurements as in [Euclid Collaboration: Ilić et al. \(2022\)](#), but we limit ourselves to probe combination, i.e. to the sum of the CMB and *Euclid* Fisher matrices:

$$F_{\alpha\beta}^{\text{tot}} = F_{\alpha\beta}^{\text{spec}} + F_{\alpha\beta}^{\text{ph}} + F_{\alpha\beta}^{\text{CMB}}. \quad (\text{A.1})$$

The Fisher matrix $F_{\alpha\beta}^{\text{CMB}}$ is defined as

$$\begin{aligned} F_{\alpha\beta}^{\text{CMB}} &= \left\langle \frac{\partial^2 \mathcal{L}^{\text{CMB}}}{\partial \theta_\alpha \partial \theta_\beta} \right\rangle = \frac{1}{2} \text{Tr} \left[\frac{\partial \mathcal{C}}{\partial \theta_\alpha} C^{-1} \frac{\partial \mathcal{C}}{\partial \theta_\beta} C^{-1} \right] \\ &= \sum_{\ell_{\min}}^{\ell_{\max}} \sum_{abcd} \frac{2\ell+1}{2} f_{\text{sky}}^{\text{CMB}} \frac{\partial C^{ab}}{\partial \theta_\alpha} (C^{-1})^{bc} \frac{\partial C^{cd}}{\partial \theta_\beta} (C^{-1})^{da}, \end{aligned} \quad (\text{A.2})$$

where $abcd \in \{T, E, \phi\}$, $f_{\text{sky}}^{\text{CMB}}$ is the effective sky fraction, C_ℓ^{cd} is the cd angular power spectrum, and the theoretical covariance matrix C is defined as

$$C = \begin{bmatrix} \bar{C}_\ell^{TT} & C_\ell^{TE} & C_\ell^{T\phi} \\ C_\ell^{TE} & \bar{C}_\ell^{EE} & C_\ell^{E\phi} \\ C_\ell^{T\phi} & C_\ell^{E\phi} & \bar{C}_\ell^{\phi\phi} \end{bmatrix}. \quad (\text{A.3})$$

Here \bar{C}_ℓ^{aa} include the isotropic noise deconvolved with the instrument beam ([Knox 1995](#)),

$$\mathcal{N}_\ell^{aa} = w_{aa}^{-1} b_\ell^{-2}, \quad b_\ell = e^{-\ell(\ell+1)\theta_{\text{FWHM}}^2/16 \ln 2}, \quad (\text{A.4})$$

where $a \in \{T, E\}$, θ_{FWHM} is the full width half maximum (FWHM) of the beam in radians, and w_{TT} and w_{EE} are the inverse square of the detector noise level for temperature and polarisation in $\text{arcmin}^{-1} \mu\text{K}^{-1}$. For CMB lensing, we use the resulting \mathcal{N}_ℓ^{TT} and \mathcal{N}_ℓ^{EE} to reconstruct the minimum variance estimator for the noise $\mathcal{N}_\ell^{\phi\phi}$ ([Okamoto & Hu 2003](#)) and use the publicly available code `quicklens`.¹⁰

We consider three different specifications for the CMB experiments with which *Euclid* could be complemented. We first consider a specification that reproduces the *Planck* 2018 uncertainties for the Λ CDM parameters ([Planck Collaboration: Aghanim et al. 2020b](#)) with a simplified setting as in Eq. (A.4): we use noise specifications corresponding to in-flight performances of the high-frequency instrument (HFI) 143 GHz channel ([Planck Collaboration: Aghanim et al. 2020a](#)) with the sky

fraction $f_{\text{sky}} = 0.7$ and the multipole range $\ell_{\min} = 2$ to $\ell_{\max} = 1500$ for temperature and polarisation. The E -mode polarisation noise is further inflated by a factor of 8 for $2 \leq \ell \leq 30$ to reproduce the uncertainty of the optical depth parameter at reionization τ ; see [Bermejo-Clement et al. \(2021\)](#). Finally, CMB lensing is obtained by combining the 143 GHz and 217 GHz HFI channels assuming a conservative multipole range of 8–400. For the CMB, we also consider the optical depth at reionisation τ and then we marginalise over it before combining the CMB Fisher matrix with the *Euclid* ones.

For the SO-like experiment, we use noise curves provided by the SO collaboration in [Ade et al. \(2019\)](#) taking into account residuals and noise from component separation.¹¹ We use spectra from $\ell_{\min} = 40$ to $\ell_{\max} = 3000$ for the temperature and temperature-polarisation cross-correlation, and $\ell_{\max} = 5000$ for the E -mode polarisation. The CMB lensing and temperature-lensing cross-correlation spectra cover the multipole range of 2–3000. We consider the sky fraction $f_{\text{sky}} = 0.4$. We complement the SO-like information with the *Planck*-like large-scale data in the multipole range of 2–40 in both temperature and polarisation.

For CMB-S4, we use noise sensitivities of $1 \mu\text{K arcmin}$ in temperature and $\sqrt{2} \mu\text{K arcmin}$ in polarisation, with resolution of $\theta_{\text{FWHM}} = 1 \text{ arcmin}$. We assume data over the same multipole ranges of SO and with the same sky coverage. In all these three cases, we do not keep τ fixed for the CMB and then we marginalise over it before combining the CMB Fisher matrix with the *Euclid* ones.

¹¹ We use version 3.1.0 available at

https://github.com/simonsobs/so_noise_models.

¹⁰ <https://github.com/dhanson/quicklens>